ΠΟΛΥΤΕΧΝΕΙΟ ΚΡΗΤΗΣ

ΣΧΟΛΗ ΗΛΕΚΤΡΟΛΟΓΩΝ ΜΗΧΑΝΙΚΩΝ & ΜΗΧΑΝΙΚΩΝ ΥΠΟΛΟΓΙΣΤΩΝ

ΔΙΠΛΩΜΑΤΙΚΗ ΕΡΓΑΣΙΑ

Ηλεκτρομαγνητική Ανάλυση Σύγχρονου Κινητήρα Μονίμων Μαγνητών με Κλωβό σε Συνθήκες Απομαγνήτισης και Σπασμένης Μπάρας

της **Ναταλίας Φατσέα**

–Εξεταστική Επιτροπή–

Αναπληρωτής Καθηγητής **Κωνσταντίνος Γυφτάκης**

Καθηγητής **Ευτύχιος Κουτρούλης**

Αναπληρωτής Καθηγητής **Ντάνιελ Μορινίγκο Σοτέλο**, Πανεπιστήμιο του Βαγιαδολίδ

Χανιά, Οκτώβριος 2025

TECHNICAL UNIVERSITY OF CRETE

SCHOOL OF ELECTRICAL & COMPUTER ENGINEERING

DIPLOMA THESIS

Electromagnetic Analysis of a Line-start Permanent Magnet Synchronous Motor with Demagnetization and Broken Bar Faults

---

of **Natalia Fatsea**

–Committee–

Associate Professor **Konstantinos Gyftakis**

Professor **Eftychios Koutroulis**

Associate Professor **Daniel Moriñigo Sotelo**, University of Valladolid

Chania, October 2025

Περίληψη

Ο Σύγχρονος Κινητήρας Μόνιμου Μαγνήτη με Κλωβό (LSPMSM) υιοθετείται όλο και περισσότερο σε βιομηχανικές εφαρμογές λόγω της υψηλής απόδοσης, της υψηλής πυκνότητας ισχύος, της ανθεκτικότητας και της δυνατότητας άμεσης εκκίνησης από το δίκτυο. Η λειτουργία του μπορεί να επηρεαστεί από βλάβες όπως η απομαγνήτιση των μόνιμων μαγνητών και η θραύση μπαρών του κλωβού του δρομέα. Ωστόσο, η σχετική βιβλιογραφία για τη μελέτη των συγκεκριμένων σφαλμάτων στους LSPMSM κινητήρες παραμένει περιορισμένη. Η παρούσα εργασία παρουσιάζει την ηλεκτρομαγνητική ανάλυση ενός κινητήρα LSPMSM, ονομαστικής ισχύος 750 W, υπό κανονικές και εσφαλμένες συνθήκες απομαγνήτισης και σπασμένης μπάρας.

Για τον σκοπό αυτό αναπτύχθηκε δισδιάστατο μοντέλο με τη Μέθοδο Πεπερασμένων Στοιχείων (FEM) χρησιμοποιώντας το λογισμικό Simcenter MAGNET, με το οποίο προσομοιώθηκε η μόνιμη και μεταβατική συμπεριφορά του κινητήρα υπό ονομαστικό φορτίο. Το μοντέλο επαληθεύτηκε με πειραματικά δεδομένα σε υγιή κατάσταση και στη συνέχεια τροποποιήθηκε ώστε να ενσωματώσει σενάρια ομοιόμορφης απομαγνήτισης και σπασμένων μπαρών. Η ανάλυση της συμπεριφοράς του κινητήρα πραγματοποιήθηκε μέσω των μεθόδων Motor Current Signature Analysis (MCSA), της παρακολούθησης της παρεκκλίνουσας μαγνητικής ροής (stray flux monitoring) και του Short-time Fourier Transform (STFT), όλες οι οποίες είναι βασισμένες στην ανάλυση του φασματικού περιεχομένου των σημάτων με τον Γρήγορο Μετασχηματισμό Fourier (FFT).

Τα αποτελέσματα έδειξαν ότι η παρακολούθηση της παρεκκλίνουσας μαγνητικής ροής αποτελεί αποτελεσματική μεθοδολογία για την ανίχνευση της απομαγνήτισης, προσφέροντας μια αξιόπιστη βάση για έγκαιρη διάγνωση και παρακολούθηση της κατάστασης του κινητήρα. Αντιθέτως, τα σφάλματα σπασμένης μπάρας εμφάνισαν λιγότερο ευδιάκριτα χαρακτηριστικά, γεγονός που αναδεικνύει την ανάγκη για περαιτέρω διερεύνηση.

Abstract

The Line-Start Permanent Magnet Synchronous Motor (LSPMSM) is increasingly adopted in industrial applications because of its high efficiency, high power density, robustness, and ability to start directly from the grid. Its performance can be significantly affected by faults such as demagnetization of the permanent magnets and broken rotor bars of the squirrel cage. However, little research has been made for the LSPMSM bearing those faults. This thesis presents a comprehensive electromagnetic analysis of a $750W$ LSPMSM under healthy and faulty operating conditions, with a focus on quantifying the impact of demagnetization and broken bar defects.

A two-dimensional FEM model was developed to simulate the motor's steady-state and transient performance under nominal load, using the Finite Element Analysis (FEA) software Simcenter MAGNET. The model was then validated against the experimental results for the healthy motor and subsequently modified to introduce uniform demagnetization and broken bar scenarios. The methods used to analyze motor behavior were Motor Current Signature Analysis (MCSA), stray flux monitoring, and Short-time Fourier Transform (STFT), all of which are based on obtaining the frequency content of the signals through the Fast Fourier Transform (FFT).

The findings highlight that stray flux monitoring is successful for demagnetization detection, providing a basis for early detection and condition monitoring. In contrast, broken bar faults exhibit less distinctive signatures, indicating the need for further study.

Acknowledgments

This thesis was made possible by the very pleasant cooperation with Pr. Daniel Moríñigo Sotelo and Dr. Tomas Garcia-Calva, from the University of Valladolid. They shared with us the model's design sheets and data, and operated the model to acquire the experimental signals used for the validation of the simulation model.

I want to thank Pr. Konstantinos Gyftakis for his guidance, his support, excellent communication, for the plentiful opportunities he has given me and for all the knowledge that I have earned from watching and listening to him.

I want to thank my parents and family for their love, support and their unwavering belief in me during all the years of my studying.

I want to thank Pr. Moríñigo Sotelo, from University of Valladolid, along with his partner Dr. Garcia Calva, for the knowledge they gave me, their help, kindness and support.

I want to thank my very loved and great friend Nikos Gkiolekas for his unconditional support, help and being there in many of my predicaments.

Finally, I want to thank all my very loved and precious friends for encouraging me all this time in this difficult journey and for being the greatest teachers about how to deal with life: Georgia Lamprinaki, Flora Loukai, Enri Ajazi, George Samonas, Georginos, Konstantinos Lazaridis, Stavros Dapontis, George Dimakis, Chrysa Kostarelou, Pinelopi Kontova, and so many others.

Contents

List of Abbreviations

A | B | D | E | F | I | L | M | P | Q | R | S

A

AC Alternating Current. 4, 14, 19, 20

B

BB broken bar. 40

D

d-axis Direct axis. 28, 30

DC Direct Current. 19, 20, 25

DOLPMSM Direct-On-Line Permanent Magnet Synchronous Motor. 27

E

EMF Electromotive Force. 28

F

FEA Finite Element Analysis. 2, 5, 10, 16, 42–45, 60, 66, 80

FEM Finite Element Method. 2, 42, 43

FFT Fast Fourier Transform. 2, 5, 6, 11, 12, 16, 39, 40, 77–79, 81, 87, 89, 91

I

IE International Efficiency. 14, 15

IEC International Electrotechnical Commitee. 14

IM Induction Motor. 10, 14, 19, 21–23, 44

IMs Induction Motors. 14, 15, 40

IPMSM Interior Permanent Magnet Synchronous Motor. 25–28

L

LSPMSM Line-Start Permanent Magnet Synchronous Motor. 2, 4, 5, 9, 10, 14, 17, 27–32, 40, 41, 45, 69, 81

LSPMSMs Line-Start Permanent Magnet Synchronous Motors. 15, 16

M

MCSA Motor Current Signature Analysis. 1, 2, 5, 16, 39, 77, 81

MMF Magnetomotive Force. 10, 31, 32, 38

P

PF Power Factor. 71

PM Permanent Magnet. 14, 15, 25, 28, 31, 40

PMs Permanent Magnets. 14, 20, 40, 41, 91

PMSM Permanent Magnet Synchronous Motor. 20, 25, 40

PMSMs Permanent Magnet Synchronous Motors. 14, 15

Q

q-axis Quadrature axis. 28, 30

R

RMF Rotating Magnetic Field. 20, 22, 26

S

SM Synchronous Motor. 4, 25–28

SMs Synchronous Motors. 14

SPMSM Surface-mounted Permanent Magnet Synchronous Motor. 25

STFT Short-time Fourier Transform. 1, 2, 5, 6, 12, 16, 39, 41, 91–93

SynRM Synchronous Reluctance Motor. 25, 26

List of Figures

Chapter 1

Introduction

According to the World Energy Outlook 2024 (WEO), total global energy demand increased by approximately 2% in 2023, reaching 640 exajoules (EJ), equivalent to 15,286 million tonnes of oil equivalent (Mtoe) [1]. The majority of this demand continues to be met by fossil fuels, with oil, natural gas, and coal accounting for around 80% [1]. Although a record level of clean energy was introduced globally two-thirds of the overall increase in energy demand in 2023 was still met by fossil fuels, driving energy-related carbon dioxide (CO_2) emissions to a record high [1]. A significant share of these primary energy resources is converted into electricity, of which more than 50% is consumed by electric motor-driven systems [2], [3], making them one of the largest contributors to global energy use and emissions. Consequently, optimizing electric motor efficiency has become a regulatory necessity.

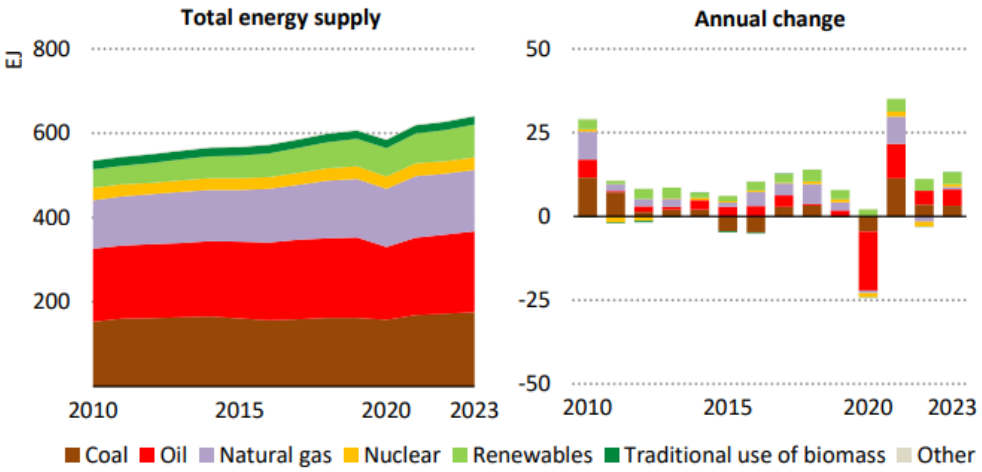

Figure 1.1: Global energy demand up to 2023[1].

1.1 Why the Line-Start Permanent Magnet Synchronous Motor

Organizations like the International Electrotechnical Commitee (IEC) have developed new standards for electric motors that require higher efficiencies. The energy efficiency of electric motors is defined in the international standard on efficiency classes for motors IEC 60034-30-1:2014. This standard establishes a set of limit efficiency values based on frequency, number of poles, and motor power. It defines the four International Efficiency (IE) classes for line-operated AC motors that Table 1.1 shows.

The efficiency improvement of Induction Motors (IMs), among all types of electric motors, is the most effective practice since they are used in the vast majority of industrial applications, due to their low cost, up to IE3 efficiency level, and high reliability [3]–[5]. This is usually achieved through design optimization of parts of the Induction Motor that contribute to overall losses, as seen in Figure 1.2. Nonetheless, it is quite challenging for IMs to reach IE4 levels, while respecting the IEC 60072 standard frame dimensions and maintaining cost effectiveness [5].

An alternative approach to improving efficiency is the replacement of induction motors with Permanent Magnet Synchronous Motors (PMSMs), which have become increasingly attractive in recent years due to the significant reduction in Permanent Magnet (PM) costs. Generally, Synchronous Motors have negligible rotor copper losses compared to Induction Motors, due to their different operating principle, and adding Permanent Magnets further increases the efficiency and power factor of these motors [6]. However, they do not have direct-on-line starting capability as Induction Motors have, meaning that they cannot start right after connecting them to the power supply. They require inverters or other motors for starting. This fact makes them uneconomical for many single-speed applications such as fans, pumps, and compressors, which account for more than 70% of the usage of electric motors [1], [5], [7].

Code IEC 60034-30-1	**Efficiency class**
IE1	Standard Efficiency
IE2	High Efficiency
IE3	Premium Efficiency
IE4	Super Premium Efficiency

Table 1.1: IEC 60034-30-1:2014 efficiency classes.

To address this limitation, Line-Start Permanent Magnet Synchronous Motors (LSPMSMs) were first introduced in the 1950s [7]. This motor combines the high efficiency and high power density of PMSMs together with the direct-on-line starting capability of IMs. Their widespread adoption was initially hindered by the limited availability and high cost of high-energy permanent magnets. But, with the recent development of advanced PM materials at more affordable prices, LSPMSMs have reemerged as a promising solution for high-efficiency industrial applications [9]–[12]. Aníbal T. de Almeida [5] discusses the motor technologies available in the 2014 market , noting that IE4 LSPMSMs were offered in the 0.55–7.5 kW range. Arash H. Isfahani [7] compares four IMs with LSPMSMs of same power, showing that the latter exceeded the IE4 super premium efficiency class in two low power ratings and noting their potential for higher power motors in the future. Many other researchers have compared them to induction motors showcasing their superiority in efficiency, power factor and cost savings [8], [12]–[14]. Figure 1.2 (b) shows the comparison of the efficiency and power factor (PF) between the LSPMSM and IM.

1.2 Research Gap and Objectives

Although LSPMSMs have been shown to outperform Induction Motors the majority of existing research has focused primarily on their performance under healthy operating conditions. Limited attention has been given to their behavior under fault scenarios, such as permanent magnet demagnetization and broken rotor bars in the squirrel cage. These faults

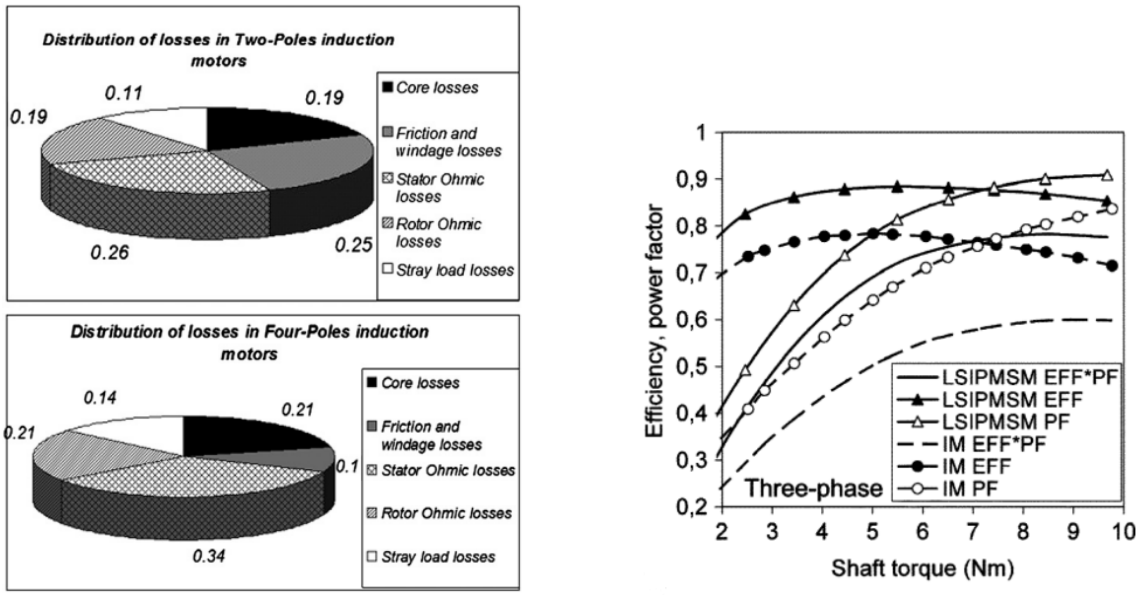

(a) (b)

Figure 1.2: (a)Distribution of losses in 2-pole and 4-pole IMs [7], and (b) efficiency (EFF) and power (PF) of LSPMSM and IM as a function of shaft torque [8].

can significantly affect machine performance, reliability, and diagnostic accuracy, and therefore deserve detailed investigation.

The main objectives of this thesis are as follows:

- **To develop and validate** an accurate electromagnetic model of a 750W LSPMSM using Finite Element Analysis (FEA).
- **To build a healthy motor behavior profile** in the frequency domain.
- **To simulate and evaluate** the impact of demagnetization and broken rotor bar faults on motor performance.
- **To compare and discuss** the results of the Motor Current Signature Analysis (MCSA) and Stray Flux Monitoring diagnostic methods applied to the faulty conditions using the Fast Fourier Transform (FFT) and Short-time Fourier Transform (STFT).

By addressing these objectives, this work aims to fill the existing research gap and provide a comprehensive electromagnetic analysis of LSPMSMs under both healthy and faulty conditions. The results contribute to a better understanding of the machine's fault behavior and can support the development of improved diagnostic techniques and fault-tolerant designs.

1.3 Thesis Structure

Below, the content of each chapter is briefly discussed to outline the structure of this thesis.

Chapter 2: Theoretical Background - This chapter introduces the fundamental theory and concepts of electrical machines. The operation principles, equations, and characteristics of induction motors, permanent magnet synchronous motors, and line-start permanent magnet synchronous motors are presented. Subsequently, different types of faults in electrical machines and diagnostic methods are discussed. The chapter concludes with a brief explanation of the finite element analysis (FEA) method used in this work.

Chapter 3: Model Development & Validation - The first part of this chapter describes the development process of the electromagnetic model, with the use of the Simcenter MAGNET software. The second part focuses on the validation of the model by comparing the healthy machine simulations with the experimental results obtained from a real 750W LSPMSM.

Chapter 4: Simulation Results & Discussion - This chapter presents the simulation of fault scenarios and discusses the results. The implementation of different diagnostic methods is described, with demagnetization faults analyzed first, followed by broken rotor bar faults.

Chapter 5: Conclusion - The final chapter summarizes the main findings of the thesis, highlights their significance for the analysis and reliability of LSPMSMs, and outlines possible directions for future research.

Chapter 2

Theoretical Background

To meet their needs, humanity utilizes various forms of energy, with electricity being one of the most widely used. Electrical energy powers essential aspects of daily life, from lighting and heating to mechanical movement, making it indispensable in residential and industrial settings. It plays a crucial role in everything from small households to large-scale factories and construction sites, enabling modern infrastructure, automation, and efficiency. With its versatility and ability to be easily transmitted and converted into other forms of energy, electricity remains a fundamental resource for technological advancement and industrial development.

2.1 Electromechanical Energy Conversion

Most industrial, commercial, and domestic functions, as well as the electrical power they consume, are the result of electromechanical energy conversion: the process of converting electrical energy into mechanical energy and vice versa. This is achieved through devices called *electrical machines*, in which electromechanical conversion takes place through the medium of a magnetic field. The flow of the conversion determines whether the machine is called an *electric motor*, which generates motion and mechanical power, or an *electric generator*, which is responsible for producing electrical energy.

Figure 2.1: Electromechanical energy conversion diagram.

2.2 Electrical Machines [15], [16]

Electrical machines consist of a stationary hollow part, the stator, and a moving part, the rotor. The rotor is placed inside the stator without touching, and the space between them is called the air gap of the machine. The stator consists of a ferromagnetic core and a single-phase or multiphase winding wound throughout its interior, forming electromagnets. The rotor also consists of a ferromagnetic core but it can either have windings or permanent magnets or nothing.

The type of electrical supply the stator receives or generates categorizes electrical machines into Direct Current (DC) and Alternating Current (AC) machines. AC machines are further classified into single-phase and three-phase, depending on the arrangement of the stator windings. Three-phase AC machines are the most widely used electrical machines worldwide, both as motors and as generators.

2.2.1 Three-phase AC Machines

The most common type of three-phase AC motor is the Induction Motor (IM), also known as an asynchronous motor. It is named after the fact that the currents flowing through the rotor are *induced* by the stator's winding currents rather than being directly externally supplied, as in, i.e., DC machines. Additionally, the rotor rotates at a different speed than the speed of the magnetic field produced by the stator current; hence the term "asynchronous".

As a generator, the asynchronous machine is not very common. It is used primarily in wind turbines and in small hydroelectric units [18], [19]. Most often, another major category of AC machines is preferred for electrical power production: the synchronous machine. This machine's rotor locks in (synchronizes) with the stator's magnetic field and retains that speed regardless of load variations. This is one of the reasons for their extensive use as generators;

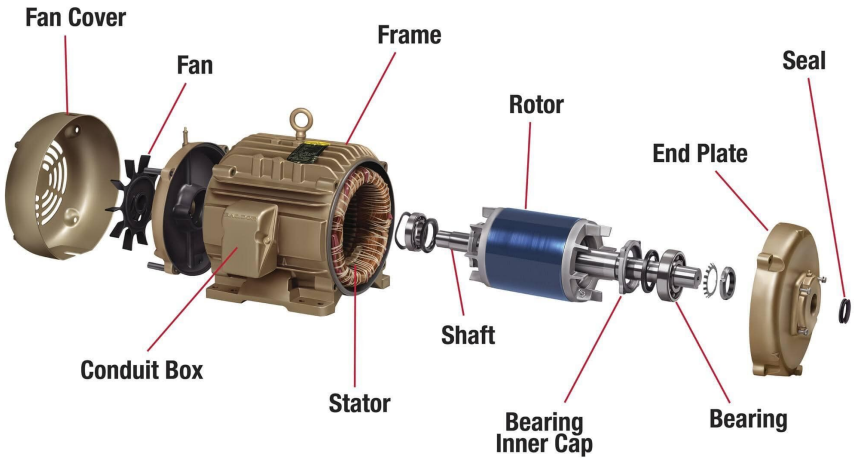

Figure 2.2: Depiction of an electrical machine and its parts. [17]

the output frequency is directly proportional to the rotor's speed. They also differ from induction machines in that the rotor's magnetic field is not induced by the stator but is instead created externally by DC excitation or Permanent Magnets (PMs).

The synchronous machine is used as a motor in applications requiring precise speed control and constant speed operation under varying loads. They are also useful in power systems, as they can help with reactive power compensation and voltage regulation by operating at unity or leading power factor. In contrast with the asynchronous machine, a disadvantage of the synchronous motor is the inability to self-start due to its different operating principle. So, they require auxiliary starting methods, such as variable speed drives, damper windings or external motors.

The primary object of this thesis is a special type of three-phase AC Permanent Magnet Synchronous Motor (PMSM), which uses an asynchronous machine's rotor to act as a damper winding. So, the focus of this chapter will be on the operation and characteristics of both synchronous and asynchronous motor types.

Operating Principle of Three-Phase AC Motors

The working principle of all three-phase AC motors is fundamentally the same and is determined by the structure and supply of the stator and the rotor. The stator contains a balanced three-phase winding, spaced 120 ° apart in space, and supplied by a sinusoidal three-phase voltage system with a 120 ° phase shift between them. The three-phase current flowing in the stator winding creates a Rotating Magnetic Field (RMF) that turns at a speed directly proportional to the current's frequency. The RMF will interact with the rotor's magnetic field to produce electromagnetic torque and cause the rotor to turn. The difference between induction and synchronous motors lies in how each produce the rotor's magnetic field.

The RMF speed is known as *synchronous speed* and is directly proportional to the supply

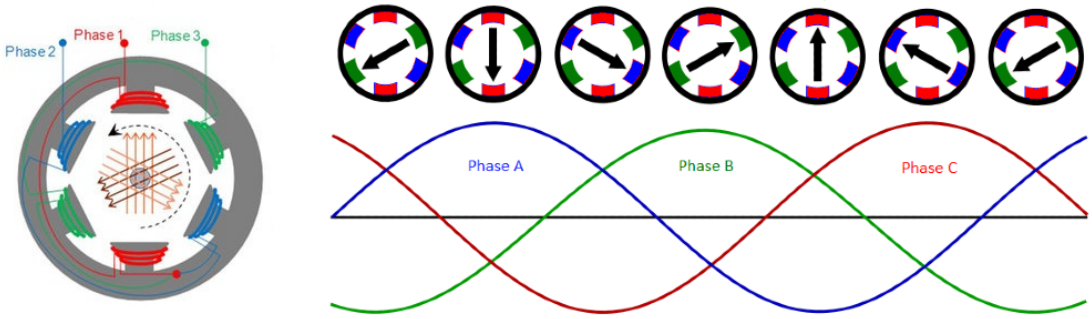

Figure 2.3: Three-phase winding of a two-pole stator supplied with three-phase current and the resulting rotating magnetic field. [20], [21]

frequency:

$$\omega_s = \frac{2\pi f_s}{p}, \quad (rad/s) \tag{2.1}$$

where $\boldsymbol{p}$ is the number of pole pairs of the magnetic field, and $\boldsymbol{f_s}$ is the electrical frequency. A more common way to measure synchronous speed is in Rounds Per Minute (RPM) and is symbolized:

$$n_s = \frac{60 f_s}{p}, \quad (RPM) \tag{2.2}$$

The resulting magnetic field is a function of time and space, and is described by the following equation:

$$B(x,t) = B_{max} \sin\left(\omega t + \pi \frac{x}{\tau_p}\right) \tag{2.3}$$

where $\boldsymbol{\omega = 2\pi f_s}$ the electrical angular frequency, $\boldsymbol{t}$ is the time, $\boldsymbol{x}$ is the distance along the circumference of the inner circle in the cross-section of the stator, measured from a freely chosen reference point, and $\boldsymbol{\tau_p}$ is the pole pitch; the distance between two consecutive poles.

2.3 Induction Motors [15], [16], [22]

The induction motor (IM) can be classified into three main categories depending on the rotor structure: the Squirrel Cage IM, the Wound Rotor IM, and the Solid Rotor IM (see Figure 2.4).

The ***Squirrel Cage Induction Motor*** is the most common type of induction motor. The squirrel cage rotor comprises two end rings that short-circuit a series of slightly skewed conductive bars, embedded on the rotor's ferromagnetic core, and are typically made of aluminum or copper. Each conductive bar constitutes one phase winding. Its wide use is due to its low cost and low maintenance needs.

The ***Wound Rotor Induction Motor*** features a rotor with a three-phase winding similar to the stator, with one side star-connected and the other side linked to a set of slip

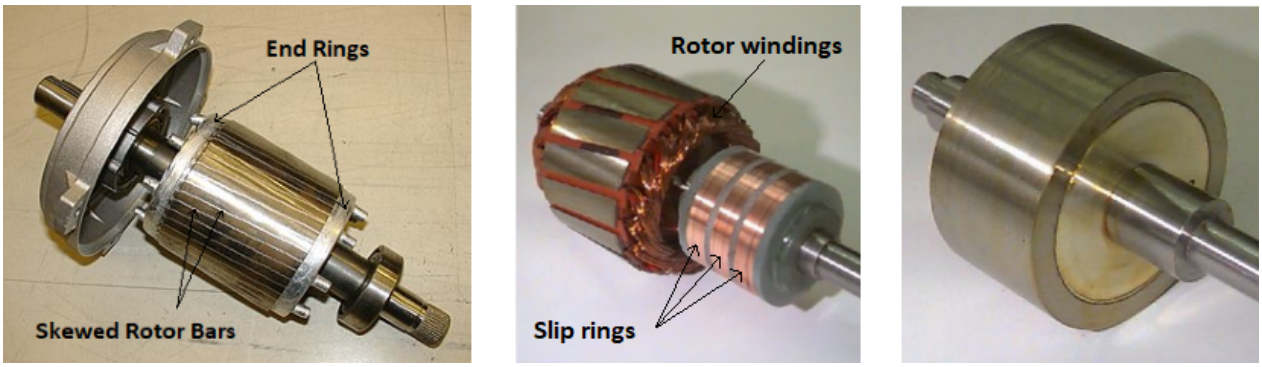

Figure 2.4: From left to right: squirrel cage rotor, wound rotor, and solid ferromagnetic rotor. [23]–[25]

rings and brushes. This configuration makes it possible to measure induced currents in the rotor and connect it to an external circuit when necessary.

The ***Solid Rotor Induction Motor***, features a rotor made of a solid cylindrical ferromagnetic core without embedded conductive bars or windings. The rotor surface is often coated with a conductive material, such as aluminum, creating a continuous short-circuit path for induced currents. This design provides a simple, rugged rotor structure, typically used in high-speed, low-power applications where starting torque requirements are low.

2.3.1 Principal of operation

The stator's Rotating Magnetic Field (RMF), as discussed in Subsection 2.2.1, will induce currents in the rotor's winding, according to the law of electromagnetic induction. Those currents together with the RMF, will develop electromagnetic torque, which will set the rotor in rotary motion in the RMF's direction, in order to resist the cause of its movement. The rotor will try to reach synchronous speed but can never fully do so due to its own inertia and mechanical friction. It will stabilize itself at a slightly lower speed than the synchronous, depending on the load. It is said then that the rotor exhibits some *slip*, which is defined as:

$$s = \frac{n_s - n_r}{n_s} 100\% \tag{2.4}$$

where $\boldsymbol{n_s}$ is the synchronous speed and $\boldsymbol{n_r}$ is the asynchronous rotor speed. Under ideal conditions with no load, the rotor might momentarily achieve synchronous speed. However, in this scenario, the relative speed between the stator's rotating magnetic field and the rotor becomes zero, resulting in no induced voltage and consequently, no torque.

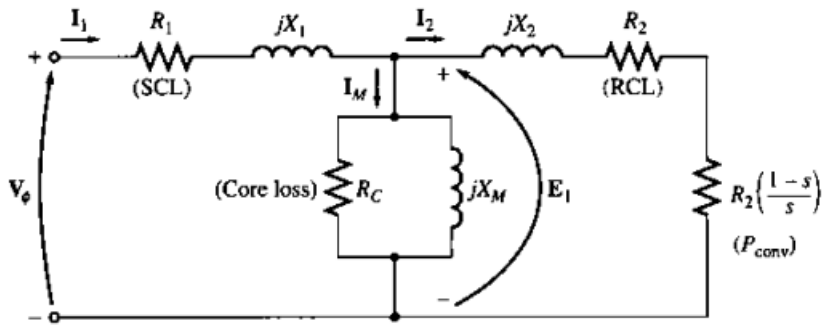

Figure 2.5: The phase equivalent circuit of an induction motor [15].

2.3.2 Equivalent circuit and equations

The phase equivalent circuit of the induction motor is illustrated in Figure 2.5, where V_ϕ, I_1 : stator phase voltage and current, R_1, R_2 : stator and rotor ohmic losses per phase,

X_1, X_2 : stator and rotor leakage reactance per phase, R_c : stator core losses, X_M : stator magnetizing reactance , E_1 : induced rotor phase voltage, I_2 : rotor phase current, and $R_2\left(\frac{1-s}{s}\right)$: useful mechanical power.

The power flow of an IM can be derived by examining the phase equivalent circuit of Figure 2.5, and is shown in Figure 2.6. The input power to an induction motor, P_{in}, is in the form of three-phase electric voltages and currents. The first losses encountered in the machine are I^2R losses in the stator windings, the *stator copper loss* P_{SCL}. Then some amount of power is lost as hysteresis and eddy currents in the stator, P_{core}. The power remaining at this point is transferred to the rotor of the machine across the air gap between the stator and rotor. This power is called the *air-gap power* (P_{AG}) of the machine. After the power is transferred to the rotor, some of it is lost as I^2R losses, the *rotor copper loss* P_{RCL}, and the rest is converted from electrical to mechanical form, P_{conv} or how it broadly known electromagnetic power, P_{em}. Finally, friction and windage losses, $P_{F\&W}$, and stray losses, P_{misc}, are subtracted. The remaining power is the output of the motor P_{out}, which is basically the coupled load.

The electromagnetic torque T_{em} of an induction motor is given by:

$$T_{em} = P_{em}\omega_r = \frac{1}{\omega_s}\frac{V_{th}^2}{(R_{th}+\frac{R_2'}{s})^2+(Xth+X_2')^2}\frac{R_2'}{s} \tag{2.5}$$

where V_th, R_{th}, and X_{th} the Thevenin equivalent input voltage, resistance and reactance on the stator's side.

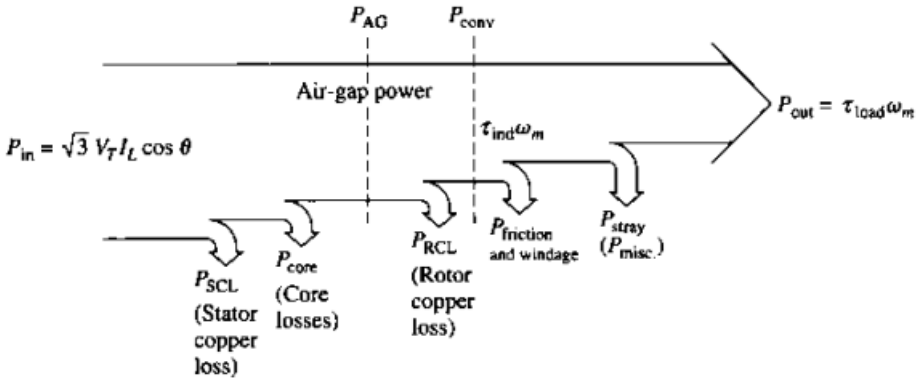

Figure 2.6: The power flow diagram of an induction motor [15]

2.3.3 Speed-Torque characteristic

The torque-speed and current-speed characteristic of the induction motor is shown in Figure 2.7. At startup, the rotor speed is zero, so the slip is maximum, resulting in high rotor currents and thus high starting torque. As the rotor accelerates and approaches synchronous speed, the slip decreases, reducing the rotor current and torque. The torque-speed curve

of the induction motor shows a low starting speed with high starting torque, increasing torque as speed rises, reaching a peak (breakdown torque), then settling at rated torque near synchronous speed. The torque-speed curve depends on the rotor's resistance as per Eq. 2.5 and is shown in Figure 2.8.

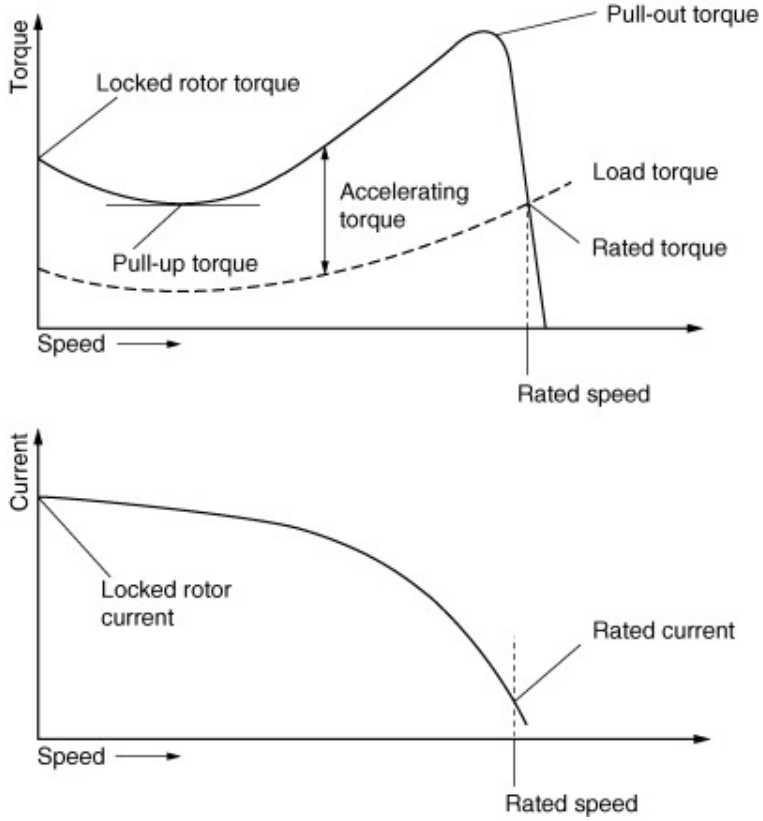

Figure 2.7: Torque-speed and current-speed characteristic of an induction motor [26]

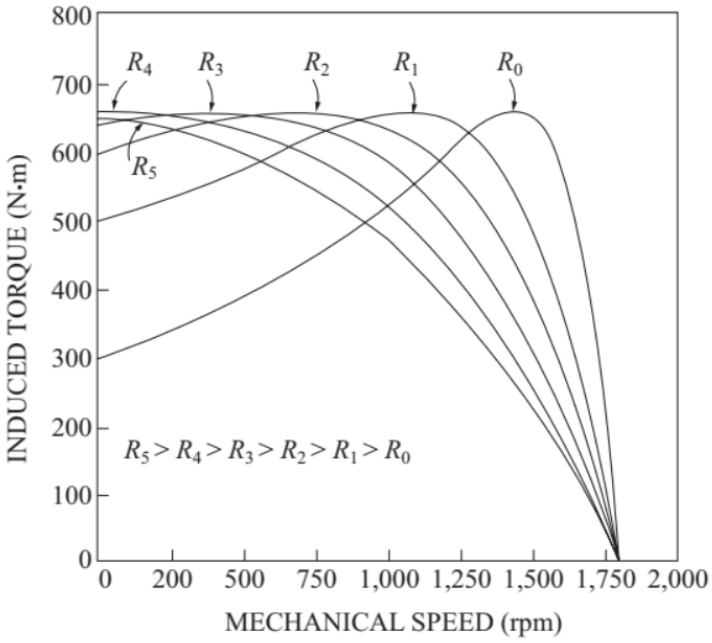

Figure 2.8: Dependence of induction motor's torque on rotor resistance [15].

2.4 Synchronous Motors [15], [16]

The synchronous motor can be classified based on the construction of the rotor into the ***Cylindrical Rotor SM*** and ***Salient Pole SM***.

The ***Cylindrical or Non-Salient Rotor SM*** has a smooth cylindrical rotor with distributed, DC-excited, field windings embedded in slots, creating a uniform air gap between the rotor and stator. A machine of this type usually has only one or two pairs of poles, therefore, it is used for high-speed applications [27]. For this reason, the rotor has a small diameter compared to its length to withstand centrifugal forces at high speed. A synchronous generator with this kind of rotor is typically used as a turbo alternator [28].

The rotor of a ***Salient Pole SM*** on the other hand has poles projecting out from the surface of the rotor core, making them visibly prominent or "salient". These poles are usually large and embedded with DC-excited windings. They have a non-uniform air gap with a larger diameter and shorter axial length. Salient pole rotors are typically used in low- and medium-speed synchronous machines and as generators mainly in hydroelectric plants and industrial generators driven by gas or steam turbines [29].

A special type of synchronous machine is the ***Permanent Magnet Synchronous Motor (PMSM)***. The rotor of a PMSM, instead of field windings, contains embedded or surface-mounted permanent magnets providing a constant magnetic field. It is known for its high efficiency, high power density, no rotor excitation losses, and compact design. It is widely used in electric vehicles, robotics, aerospace, machine tools [30]–[33]. Depending on where the PMs are placed, it is further divided into ***Interior Permanent Magnet Synchronous Motor (IPMSM)*** and ***Surface-mounted Permanent Magnet Synchronous Motor (SPMSM)***. Out of the two, the one relevant to the subject of this thesis, is the IPMSM.

Another special category of SMs is the ***Synchronous Reluctance Motor (SynRM)*** in which electromagnetic torque is generated due to the difference in magnetic reluctance along different axes of the rotor, rather than by rotor windings or PMs. The rotor structure features *flux barriers* to create this anisotropy. Flux barriers are low-permeability gaps inside

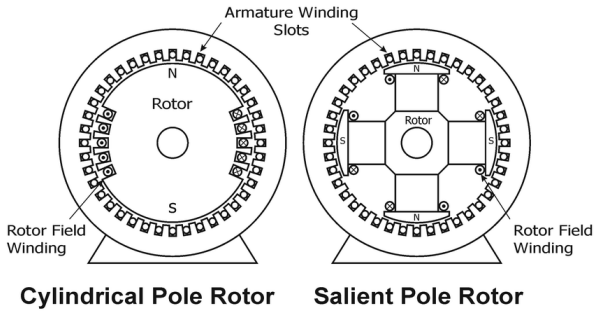

(a) Rotor topology based [34]

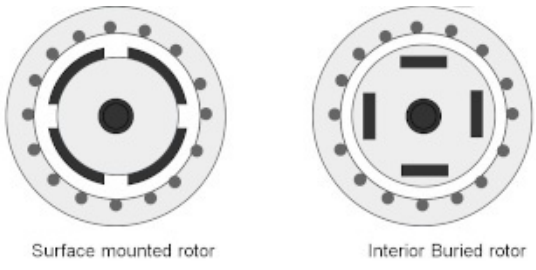

(b) Permanent Magnet SM types [35]

Figure 2.9: Classification of synchronous machines.

the rotor with the purpose of blocking or redirecting the magnetic flux within it, increasing the magnetic reluctance in specific paths. Beside the SynRM, they are also used in IPMSMs.

2.4.1 Principal of operation

The working principal of a synchronous motor is based on the "synchronous operation" principle, where the rotor magnetic field is locked in synchronism with the stator's rotating magnetic field, just as a north magnetic pole locks in with a south magnetic pole. A synchronous motor does not have the ability to start on its own because its rotor needs to be spinning at nearly synchronous speed for its separate magnetic field to lock with the stator's field, a speed it cannot reach from a standstill. However, an induction motor can self-start because its rotor generates torque through induced currents from the rotating magnetic field.

An example is given of a salient two-pole SM in Figure 2.10. The stator produces an RMF spinning clockwise at synchronous speed n_s. The rotor's static magnetic field is created externally with the help of either permanent magnets or DC excitation of the rotor's field windings. From the standstill starting position shown in the figure, during the first half of the electrical cycle, the rotor will create a counterclockwise torque with the aim of N2 and S2 locking with S1 and N1, respectively. However, since the stator's RMF is already spinning fast and since the rotor has a starting inertia, the stator's two poles will rotate another half a period with the rotor being almost in the same position. Now, the torque produced will be clockwise, chasing the two poles of the stator again. So, the rotor is unable to follow the fast rotation of the RMF, resulting in ***zero torque*** over one electrical cycle. What happens to the motor is that it vibrates heavily with each electrical cycle and finally overheats.

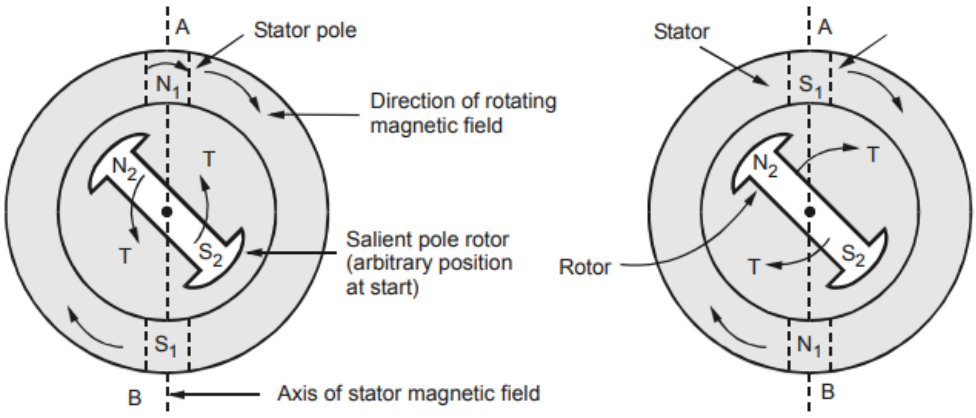

Figure 2.10: Depiction of a synchronous motor's inability to self-start [36]

2.4.2 Starting methods of a SM

With the synchronous motor having no net starting torque there are three main ways to start a synchronous motor safely:

Method 1 With the help of power electronics, reduce the stator frequency low enough for the rotor to be able to catch up during a half electrical cycle with power electronics.

Method 2 Use an external prime mover to rotate the rotor up to synchronous speed, go through the paralleling procedure, and bring the machine on the line as a generator. Then, turning off or disconnecting the prime mover will make the synchronous machine a motor.

Method 3 Put amortisseur or damper windings on the motor to accelerate it to near-synchronous speed before a direct current is applied to the field windings (if such windings exist). It works based on the principle of induction.

The damper winding mentioned in Method 3 above can also be in the form of a squirrel cage. An IPMSM with such a damper winding is the motor studied in this thesis and is generally called ***Line-Start Permanent Magnet Synchronous Motor (LSPMSM)*** or ***Direct-On-Line Permanent Magnet Synchronous Motor (DOLPMSM)***, because of its capability of starting right after connecting it to the power supply line. It will be referred to extensively in the next section.

2.4.3 Equivalent circuit and equations

Because of the non-uniform air gap of a Salient Pole SM, the magnetic reluctance is small along the narrow part of the air gap, and bigger along the wide part. The magnetic flux

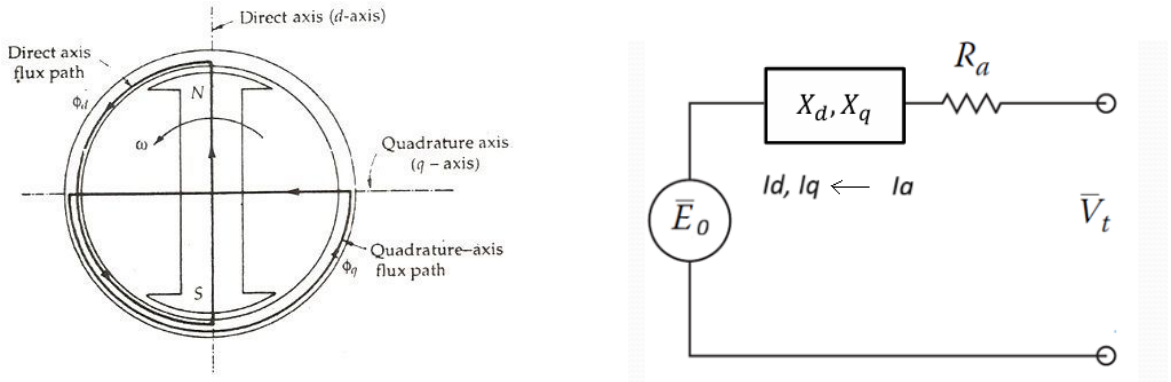

(a) (b)

Figure 2.11: (a) Rotating d-q reference frame [37], and (b) Equivalent circuit of an IPMSM [38].

will go through the path of the least reluctance. The existence of the permanent magnets of an IPMSM will also create an anisotropy in the air gap magnetic reluctance even though it has an even air gap along the rotor perimeter. That is why the analysis of the motor in both cases is based on a synchronously rotating Direct axis (d-axis) and a Quadrature axis (q-axis) reference frame, as Figure 2.11a depicts. Thus, the equivalent circuit of an IPMSM is the same as the equivalent circuit of a Salient Pole SM, and is presented in Figure 2.11b. The equations describing the equivalent circuit are:

$$\begin{bmatrix} E_f \\ 0 \end{bmatrix} = \begin{bmatrix} V_q \\ V_d \end{bmatrix} + (R_a + j \cdot \begin{bmatrix} X_q & 0 \\ 0 & X_d \end{bmatrix}) \cdot \begin{bmatrix} I_q \\ I_d \end{bmatrix} \Rightarrow \begin{bmatrix} E_f \\ 0 \end{bmatrix} = \begin{bmatrix} V_q + R_a I_q + X_d I_d \\ V_d + R_a I_d - X_q I_q \end{bmatrix} \tag{2.6}$$

where E_0: the back electromotive force (back-EMF) produced by the PMs , V_d and V_q: the d-axis and q-axis terminal voltages, R_a: the armature winding resistance, X_d and X_q: the d-axis and q-axis reactances, and I_d and $_q$: the d-axis and q-axis currents.

2.5 The Line-Start Permanent Magnet SM

A Line-Start Permanent Magnet Synchronous Motor consists of a single or polyphase stator as one of the induction motors and a hybrid rotor involving an electricity conducting squirrel cage and pairs of permanent magnet poles. Usually, it also contains flux barriers to determine the magnetic flux path within the rotor. Many different combinations of the cage, pole shapes, pole locations, and magnetic flux barriers have been presented for the rotor so far [39], [40]–[43]. Figure 2.12(a) shows a three-phase 4-pole LSPMSM and its many possible rotor topologies.

2.5.1 Equivalent circuit and equations

The modeling of LSPMSM is based on the stationary d-q reference frame, as described, and is given by the following expressions [7], [46], [47]:

$$V_{sq} = r_s i_{sq} + \omega_r \lambda_{sd} + \frac{d\lambda sq}{dt} \tag{2.7}$$

$$V_{sd} = r_s i_{sd} - \omega_r \lambda_{sq} + \frac{d\lambda sd}{dt} \tag{2.8}$$

$$V'_{rq} = r'_{rq} i'_{rq} + \frac{d\lambda' rq}{dt} = 0 \tag{2.9}$$

$$V'_{rd} = r'_{rd} i'_{rd} + \frac{d\lambda' rd}{dt} = 0 \tag{2.10}$$

where V_{sq}, V_{sd}, V'_{rq}, and V'_{rd} are stator and rotor voltages, λ_{sq}, λ_{sd}, λ'_{rq}, and λ'_{rd} stand for linkage fluxes of stator and rotor and i_{sq}, i_{sd}, i'_{rq}, and i'_{rd} represent stator and rotor currents respectively. ω_r, r_s, r'_{rd}, and r'_{rq} denote rotor speed, stator resistance and rotor resistances referred to stator respectively. Moreover, linkage fluxes of stator and rotor are determined as follows:

$$\lambda_{sq} = L_{sq} i_{sq} + L_{mq} i'_{rq} \tag{2.11}$$

$$\lambda_{sd} = L_{sd} i_{sd} + L_{mq} i'_{rd} + \lambda'_m \tag{2.12}$$

$$\lambda'_{rq} = L'_{rq} i'_{rq} + L_{mq} i_{sq} \tag{2.13}$$

$$\lambda'_{rd} = L'_{rd} i'_{rd} + L_{md} i_{sd} + \lambda'_m \tag{2.14}$$

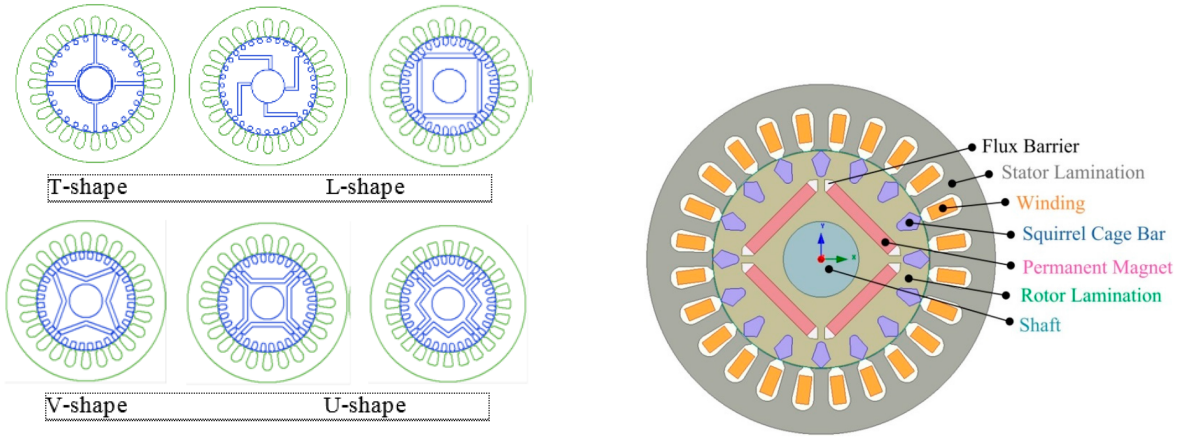

(a) (b)

Figure 2.12: (a) Different rotor topologies of a 4-pole LSPMSM [44], and (b) the LSPMSM relevant for this thesis [45].

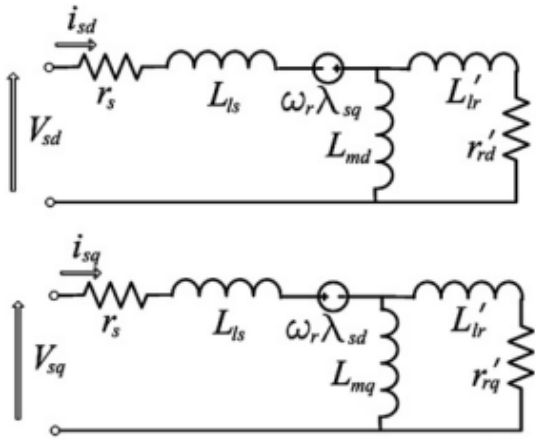

Figure 2.13: A d-q reference frame equivalent circuit of the LSPMSM [7].

where L_{sq}, L_{sd}, L'_{rq}, and L'_{rd} are stator and rotor self-inductances, respectively, and L_{mq} and L_{md} are mutual inductances. The permanent magnet flux is represented by λ'_m. A schematic view of the d-axis and q-axis equivalent circuits is illustrated in Figure 2.13.

2.5.2 Torque expression and Torque-Speed characteristic

The electromagnetic torque during asynchronous and synchronous operation is given by [7]:

$$T_{em} = \underbrace{\frac{3p}{2}(L_{md}i'_{rd}i_{sq} - L_{mq}i'_{rq}i_{sd})}_{T_C} + \underbrace{\frac{3p}{2}\lambda'_m i_{sq}}_{T_{PM}} + \underbrace{\frac{3p}{2}(L_{sd} - L_{sq})i_{sd}i_{sq}}_{T_R} \tag{2.15}$$

in which the first term is the cage torque, T_C, the second term is the permanent magnet torque, T_{PM}, and the third term is the reluctance torque, T_R.

During asynchronous operation, the sum of the permanent magnet torque T_{PM} and the reluctance torque T_R is generally called braking torque $T_{braking}$, because it opposes the average torque produced by the squirrel cage. $T_{PM_{braking}}$ is maximum at high slip and fades to zero as $s \to 0$. It is largely dependent on the saliency ratio (Lsq/Lsd) of the motor and also on the back-emf of the motor, E_0. That is why a high-saliency PM motor with large back-emf results in a greater brake torque during starting [8], [46].

After synchronization, the squirrel cage torque T_C becomes zero, just as in the induction motor, thus leaving only T_{PM} and T_R in expression 2.15, the sum of which is now called synchronous torque, $T_{synchronous}$.

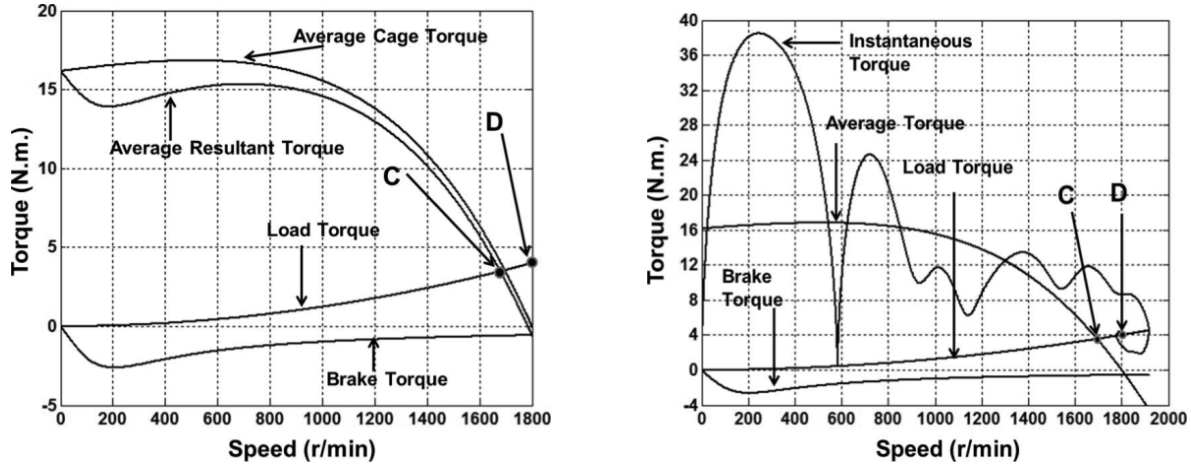

(a) (b)

Figure 2.14: (a) Average asynchronous torque, and (b) Instantaneous torque versus speed of a LSPMSM [46].

The following well-known expression governs The motor dynamic:

$$T_{em} - T_{load} - \underbrace{B_f \omega_r}_{T_{friction}} = \underbrace{J \frac{d\omega_r}{dt}}_{T_{acc}} \tag{2.16}$$

where T_{load}, $T_{friction}$, B_f, T_{acc} and J are the load torque, the friction torque, the viscous friction coefficient, the acceleration torque, and the moment of inertia, respectively. The Torque-Speed characteristic of the LSPMSM is illustrated in Figure 2.14.

Starting and synchronization process [7], [9], [10], [46]–[48]

The motor starts as an induction motor by the combination of two torque components: cage torque, T_C and braking torque, $T_{PM_{braking}}$. The maximum of $T_{PM_{braking}}$ at low speed will create a dip in the average resultant torque curve (T_{em}), as shown in Figure 2.14(a). Then, as the speed increases, T_{em} will reach the maximum point (pullout torque) due to the average cage torque T_C before it starts to decrease. It intersects with the load curve at a speed slightly below the synchronous speed, as indicated by point C. The synchronization point is indicated by point D. The jump from point C to point D is a dynamic process, called pull-in process, and it is better illustrated in the instantaneous torque curve as shown in Figure 2.14(b).

The starting and synchronization of the LSPMSM is influenced by five main factors: the PM braking torque, the cage resistance, the input voltage, the shaft inertia and the occurence of torque dips due to MMF harmonics. If the braking torque is sufficiently high, it causes the average resultant torque to intersect with the load curve at low speeds, leading to failure in starting or synchronization, as shown in Figure. A reduced input voltage slows the motor

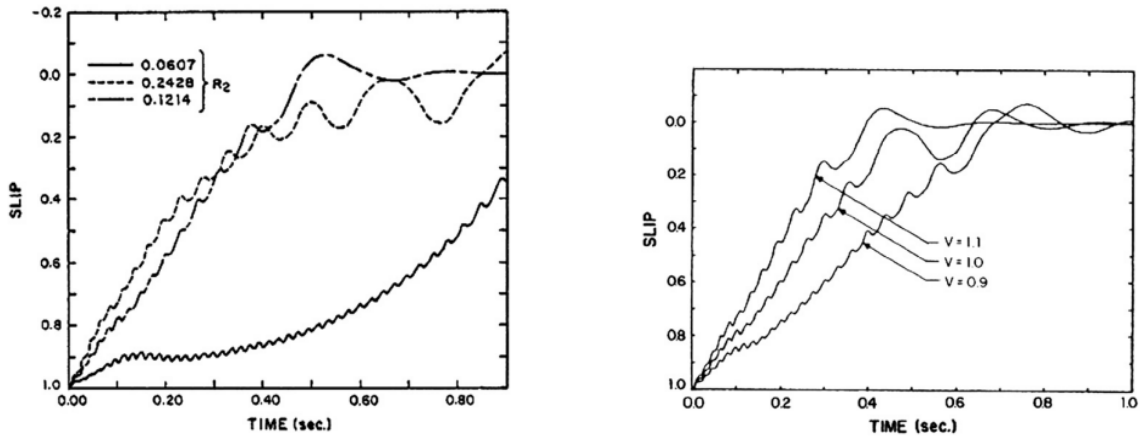

(a) (b)

Figure 2.15: (a) Effect of cage resistance, and (b) Effect of input voltage on starting and synchronization of an LSPMSM [49].

transient and may also lead to synchronization failure, while cage resistance needs to be optimally chosen for proper starting [50]. Increasing load inertia also deteriorates motor starting performance, causing high torque pulsations during start-up, sometimes preventing synchronous operation.

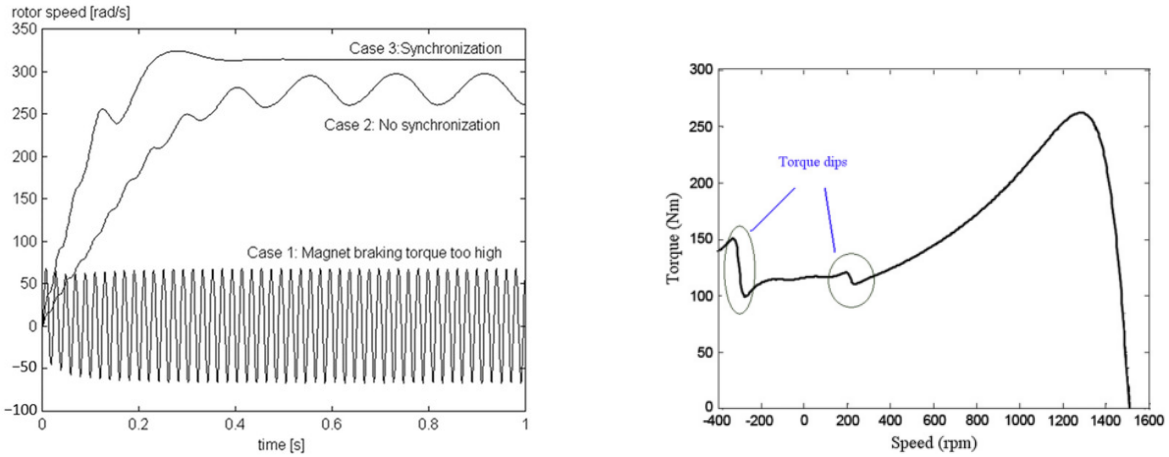

(a) (b)

Figure 2.16: (a) Effect of braking torque on starting and synchronization of an LSPMSM [51], and (b) Effect of MMF harmonics on torque-speed characteristic of induction motors [52].

Due to the existence of the squirrel cage, MMF harmonics create parasitic torques at all speeds, typically causing dips in the torque-speed characteristic [53], [54]. MMF harmonics (also called space harmonics) are the spatial harmonic components of the magnetomotive force distribution in an electrical machine air gap. These arise because the MMF produced by the windings is not a perfect sinusoidal distribution around the air gap but instead contains multiple spatial frequency components due to the discrete slotting and winding layout. Those dips combined with the breaking torque might reduce torque significantly at low speeds, causing starting failures under load.

2.6 Faults in LSPMSMs

Unexpected faults often occur in electric motors due to mechanical, electrical, and thermal stresses. These faults can affect the operation of the machine, reduce its efficiency, and lead to severe damage that may even result in catastrophic failure. Both economic considerations and safety concerns highlight the need for the development and improvement of effective fault detection techniques.

In permanent magnet synchronous motors, faults can generally be classified into three main categories: electrical, mechanical, and magnetic, as eplained in Figure 2.17). Mechanical faults are particularly common in electric machines, accounting for approximately 60% of all

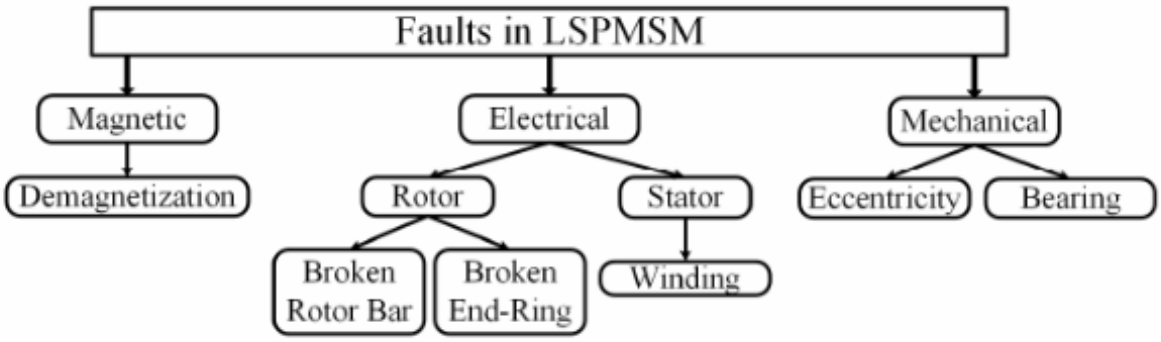

Figure 2.17: Fault classification of LSPMSMs [56].

motor faults, with about 80% of these cases caused by rotor–stator eccentricity. Bearing failures are also significant, contributing between 13% and 41% of failures, depending on the machine type and size. Stator winding faults are another frequent cause of failure in AC motors, representing between 36% and 66% of all faults. Since the conventional PMSM does not have a squirrel cage there is still no known percentage for broken squirrel cage components. Nonetheless, it is known that broken rotor bar and broken end-ring failures account for around 8-9% in induction motor faults [55].

2.6.1 Magnetic Failures

Magnetic faults appear only in permanent magnet machines and consist of irreversible demagnetization faults and mechanical type faults, where the permanent magnets have suffered material damage. The main factors that cause these faults include armature reaction, conflicting magnetic fields, contact of magnets with foreign objects causing damage, corrosion, aging of the permanent magnets, and high temperatures.

The temperature of the permanent magnets rises when the motor operates under high load torque in harsh environmental conditions, as well as when there are internal short-circuit faults in the stator windings, since the short-circuit current there is large and causes a local temperature increase.

Demagnetization can be defined as the loss of the magnetic flux density of the permanent magnets, resulting in the degradation of permanent magnet machine performance. Demagnetization is classified into two types: uniform demagnetization, which happens evenly across the pole, and partial demagnetization, where only specific regions of the material are affected.

In the case of irreversible demagnetization, the strength of the permanent magnets weakens, causing a higher current to be required in the stator to produce a stable output torque. As a result, copper losses and temperature increase, which contribute to further demagnetization, an increase in stator current, and a decrease in motor efficiency.

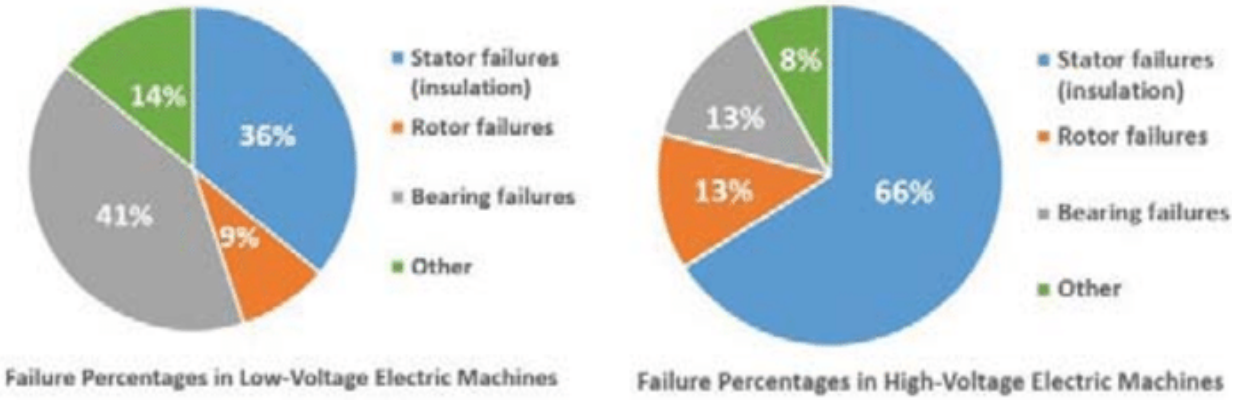

Figure 2.18: Failure percentages by various components in low-voltage electric machines (left) and high-voltage electric machines (right) [57].

In conclusion, demagnetization can lead to unbalanced rotor flux, overload conditions, unwanted noise, and destructive vibrations that may cause bearing wear and rotor damage.

2.6.2 Electrical Failures

Since they have a squirrel cage rotor, a fault that can occur in line start permanent magnet synchronous motors is the broken rotor bar (BB) fault. These faults usually originate from manufacturing defects and, combined with the skin effect—which causes current density in a conductor to be higher on its surface than in its interior—make the bars more vulnerable to cracks and holes.

During motor startup, especially under heavy mechanical load, a high current flows through the rotor bars, significantly increasing their temperature. This temperature rise poses a risk that bars with defects may crack or break. Once a bar breaks, its current is redistributed to neighboring bars, meaning these bars carry more current, which increases the likelihood of failure even if those bars do not have any manufacturing defects. In Figure 2.19 a squirrel cage rotor is shown with 3 broken bars.

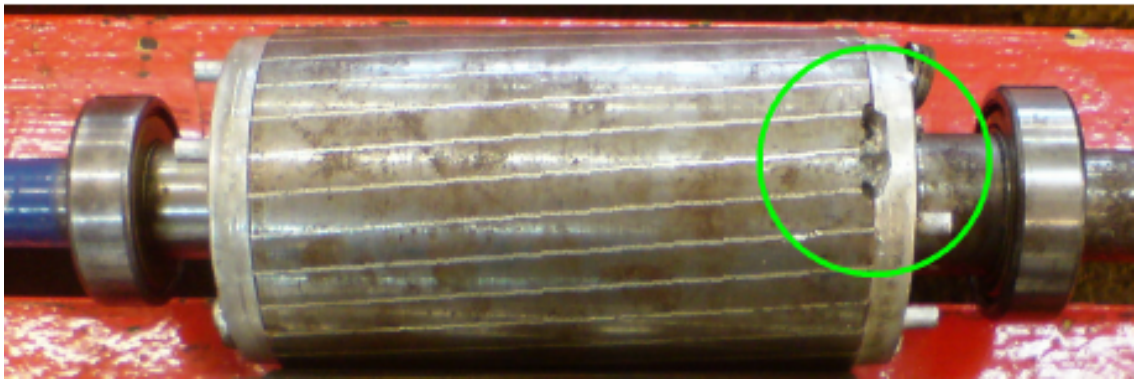

Figure 2.19: Squirrel cage rotor with 3 broken bars [58].

The stator windings, consisting of wire coils wrapped around the poles, are normally insulated to prevent electrical faults. These faults include short circuits between adjacent coils of the same phase, between coils of different phases, between phase and ground, as well as open circuits (see Figure 2.20). Experimental observations show that short circuits between neighboring coils, if left unaddressed, often lead to other types of electrical faults.

Such electrical faults typically arise from insulation degradation caused either by mechanical wear and tear or overheating due to motor overload. Internal short circuits happen when insulation failure between two adjacent coils creates a closed circuit, inducing voltage by Faraday's law and causing current to flow. This current in the shorted path is much higher than the normal phase current, generating intense heat. If not detected and remedied promptly, this heat can damage insulation in neighboring coils, resulting in phase-to-phase or phase-to-ground short circuits, or even open circuit faults.

Furthermore, the high currents in the shorted paths produce strong magnetic fields, which combined with elevated temperatures, increase the risk of irreversible demagnetization of the permanent magnets. Internal short circuits are particularly dangerous as they spread rapidly and are notoriously difficult to diagnose, especially since they do not cause significant changes in phase currents and thus evade many industrial safety detection systems.

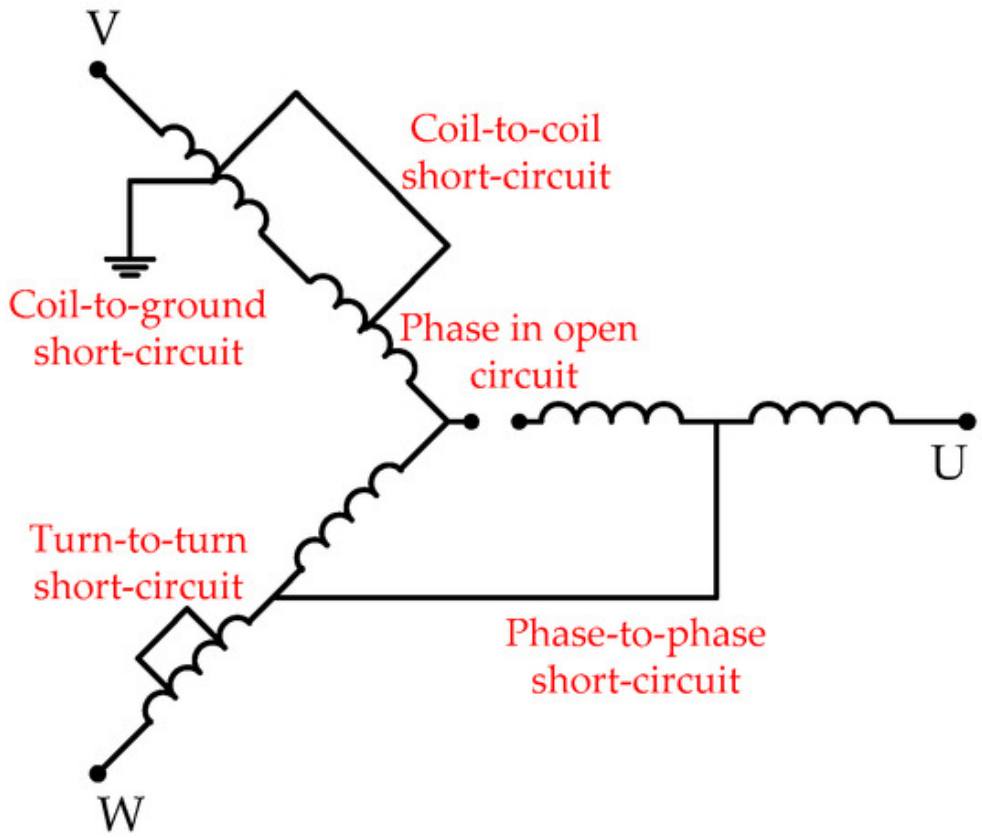

Figure 2.20: Categories of short circuits in the stator winding [59].

2.6.3 Mechanical Failures

Mechanical faults in electric machines mainly arise from issues in the moving parts, primarily involving bearing damage, rotor eccentricity, and shaft bending due to uneven weight distribution of the rotor. Bearings support the rotor, preventing it from dropping due to gravity, while enabling smooth rotation. A typical bearing consists of an outer ring, an inner ring, rolling elements that bear heavy dynamic loads and rotate at high speeds, and optionally a cage around these rolling elements (see Figure 2.21). Most electric machines use bearings with cylindrical rolling elements.

Even under normal operating conditions with balanced loads and proper alignment, bearings can develop faults over time from wear and aging. Lubrication is crucial for bearing performance; inadequate lubrication increases the risk of metal-to-metal contact, while excessive lubrication leads to heat buildup and friction as rolling elements try to push through excess grease. Environmental contaminants such as dust, dirt, moisture, and corrosive chemicals also degrade bearing performance. Misalignment during assembly or shaft bending from overheating or overload causes vibrations that accelerate bearing wear. Overloading may crack or destroy rolling elements, causing high levels of dynamic eccentricity. Sometimes bearing faults manifest as rotor asymmetry faults, often grouped under eccentricity-related faults.

Electric arc erosion is another significant cause of bearing damage. This occurs when current passes through the bearing, stopping at contact points between rings and rolling elements, generating localized heating that may cause dents on rings or rolling elements.

When the machine is healthy, the rotor rotation axis coincides with the geometric center of the stator, resulting in uniform air-gap thickness around the machine. Uneven air-gap distribution, called eccentricity fault, is categorized into static, dynamic, and mixed eccentricity (see Figure 2.22). Static eccentricity occurs when the rotor axis coincides with the rotor geometric center but is displaced relative to the stator center, keeping the minimum air gap stationary during rotation. Dynamic eccentricity happens when the rotor's rotation axis deviates from its geometric center but aligns with the stator center, causing the minimum air gap position to vary during rotation. Often, both types coexist, leading to mixed eccentricity. Such eccentricity faults induce vibrations, noise, and torque ripple, and at severe levels can cause rotor-stator rubbing, resulting in electrical or magnetic motor damage.

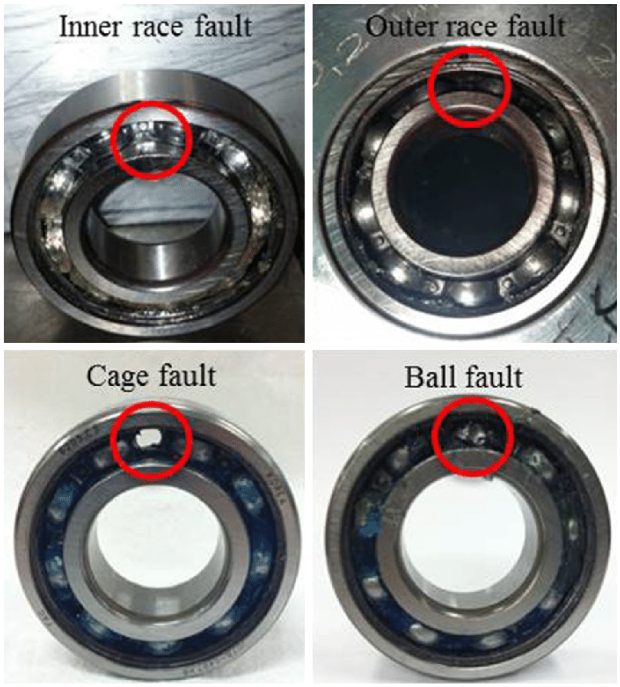

Figure 2.21: Bearing type faults [60].

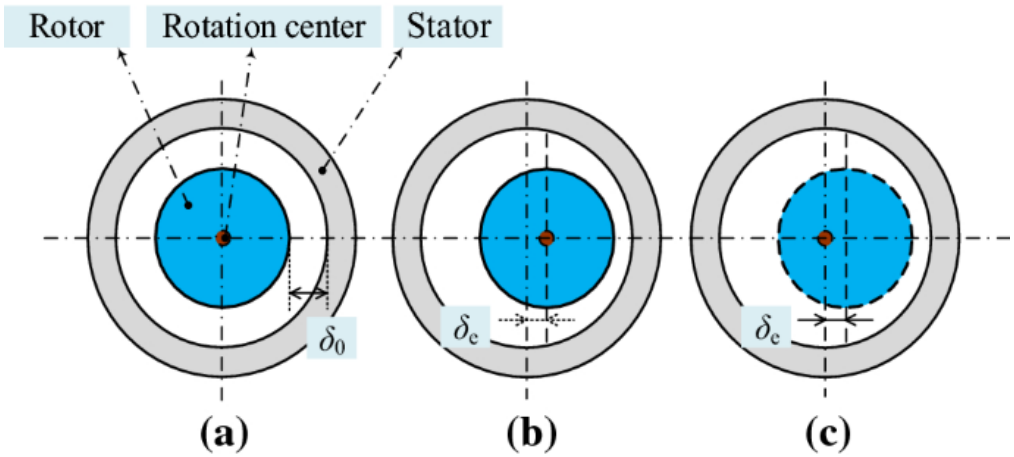

Figure 2.22: Illustration of (a) rotor placement in healthy motor, (b) rotor with static eccentricity, and (c) rotor with dynamic eccentricity [61].

2.7 Fault Diagnosis Methods

Most of the diagnostic methods currently used are based on processed electrical signals and mechanical signals such as vibration velocity and acceleration. Changes caused by electrical damage to the motor are well reflected in the current and voltage signals of the motor, with the stray flux signal being one of the most sensitive to these damages. Mechanical damage is very well revealed in the velocity and acceleration of vibration. Demagnetization causes an asymmetric Magnetomotive Force (MMF) in the air-gap and unbalanced radial forces, resulting in high vibration and noise. In the case of heavy noise caused by motor damage, an acoustic analysis based on noise can be used as an additional approach.

It should be noted that, unlike the measurement of currents and voltages, which are non-invasive and easy to implement in any drive, the measurement of leakage fluxes and vibration requires the installation of the appropriate sensors.

Fault diagnosis methods that process digital signals are able to extract characteristic symptoms, a profile, for each specific type of fault. They are categorized into three groups: methods based on the frequency domain, methods based on the time domain, and methods that combine both time and frequency domains (see Figure 2.23).

Time Domain Methods

System monitoring is a continuous and dynamic process; thus, useful features for fault diagnosis naturally appear in the time domain. Time-domain methods primarily rely on statistical analysis and utilize system parameters like maximum values, RMS values, mean

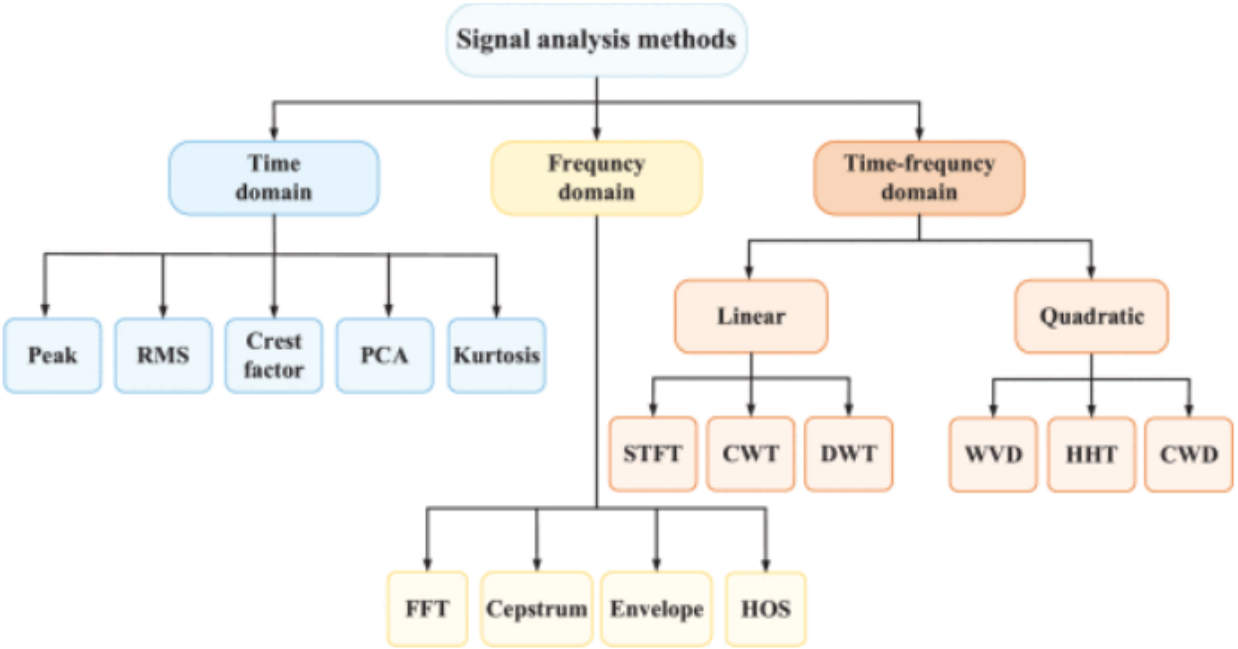

Figure 2.23: Signal analysis methods for AC motors and drives [62].

value, root mean square, kurtosis, and others.

Frequency Domain Methods

The most common signal analysis method in the frequency domain is the Fast Fourier Transform (FFT), which represents a signal as a sum of sinusoidal functions. Its key advantage lies in clearly depicting the signal's frequency distribution, enabling the detection of changes in amplitude and frequency of harmonic components that serve as indicators of various faults.

Time-Frequency Domain Methods

Despite the many advantages of frequency-domain analysis methods, they also have significant drawbacks. The most important is that they require signals to be stationary, which might not always represent the nature of the fault. Time-frequency analysis can identify the signal's frequency components and highlight their time-varying characteristics, making it a valuable tool for monitoring and diagnosing faults in systems with varying operating conditions.

The most popular technique is the Short-time Fourier Transform (STFT), which applies the FFT in short, windowed segments of the signal, using windows such as rectangular, Hamming, Hanning, and others. Another widely used method is the Wavelet Transform (WT), which employs variable-sized windows to decompose continuous-time functions into wavelets, enabling the detection of local features in signals that other analysis techniques might miss. Some other include, Bilinear Transforms (BTs), Hilbert Huang Transform (HHT), and Multiple Signal Classification (MUSIC).

In the following, the demagnetization and rotor-broken bar fault diagnosis techniques will be discussed. The methods employed are the Motor Current Signature Analysis (MCSA) and stray flux monitoring.

2.7.1 Motor Current Signature Analysis

The stator phase current is one of the most frequently used signals for fault diagnosis because analyzing its frequency signatures offers a low-cost, highly reliable, and minimally invasive method that can be applied without disconnecting the motor. Specifically, this method involves recording the current signals of each phase and analyzing them in the steady-state using the Fast Fourier Transform.

Demagnetization of Permanent Magnets [62]–[64]

In the case of uniform or partial PM demagnetization fault, the appearance of disturbances in the PMSM magnetic field causes a distortion of the sinusoidal magnetomotive force. As a result, additional harmonics appear in the stator current spectrum around the fundamental supply frequency:

$$f_{dmg} = (1 \pm k\frac{1}{p})f_s \qquad , k = 1, 2, 3... \tag{2.17}$$

where f_{dmg} the demagnetization fault harmonic index, and p the number of motor poles. An increase in the degree of demagnetization of the rotor causes an increase in the amplitude of the stator current harmonics defined by Eq. 2.17.

Broken rotor bars [65]–[67]

In induction motors, electromagnetic analysis gives the following expression for the frequency of the fault:

$$f_{bb} = (1 \pm 2ks)f_s = f_s \pm 2ksf_s \qquad , k = 1, 2, 3... \tag{2.18}$$

where f_{bb} the broken bar (BB) faulty harmonic frequency. The lower sideband is specifically due to a broken bar, the upper sideband is due to consequent speed oscillation. Experience shows that when the amplitude of the $(1 - 2s)f_s$ harmonic is greater than $-42dB$ it is accurately indicative of a broken rotor bar in the motor. A broader and more general expression for broken bar harmonics is given by:

$$f_{bb} = [\frac{k}{p}(1 - s) \pm s]f_s = sf_s \pm kf_r \qquad , k = 1, 2, 3... \tag{2.19}$$

For the line-start PMSM however, the above BB signatures are not very indicative since the synchronous operation of the motor means that no current flows through the cage rotor when in steady state operation. Thus, nothing significant is expected from analysing the stator current spectrum of the LSPMSM, derived from the FFT.

2.7.2 Stray Flux Monitoring

Stray flux monitoring offers several advantages, being both inexpensive and noninvasive. It uses sensors such as coils with many turns or Hall effect sensors, which are placed on the motor in positions calculated to measure either the radial flux, the axial flux, or a combination of both directions. This enables early fault detection without the need to disconnect the motor or open it up. Moreover, when the motor performance is affected by faults, the asymmetry affected variables in IMs are first the main air-gap flux, then stator back-emfs and finally the

stator current. Besides, the stator current frequency spectrum can be different depending on winding configuration, winding connection type, and motor topology. Thus, the stray flux signal contains more information about the frequency state of the motor compared to the current signal.

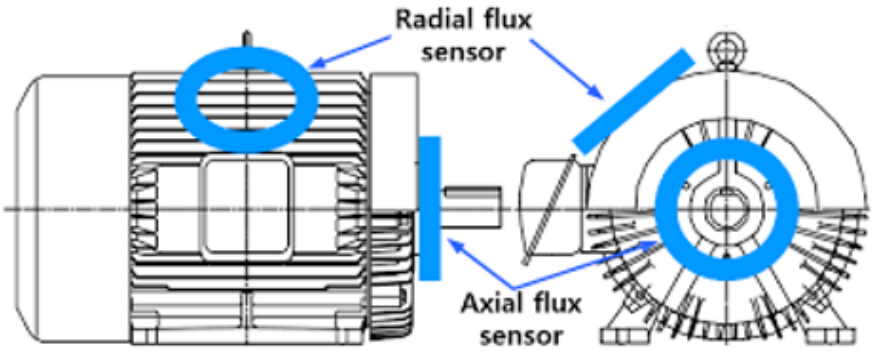

Figure 2.24: Sensor position for stray flux measurements [68].

Demagnetization of PMs [62], [69]

The same expression, Eq. 2.17 applies for monitoring the leakage flux. Because PMs directly affect the overall magnetic field of the motor, this type of fault is more obvious by observing the stray flux rather than the stator current.

Broken rotor bars [70]–[72]

The stray flux spectrum has been determined to contain the following frequency signatures indicating the existence of broken bar faults: the mechanical frequency related harmonics $f_s \pm f_r$, their sidebands $f_s \pm f_r \pm 2sf_s$, and the rotor current frequencies sf_s and $3sf_s$.

2.7.3 STFT for Broken Bar Faults [69], [70]

During the start-up of the LSPMSM motor, the squirrel cage will have current induced in it. The STFT can be applied for the transient part of the stator current and leakage flux signals to determine whether diagnosis of broken bar faults is possible for this kind of machine. This is done by analysing their frequency variations that are expressed as distinct trajectories.

Applying the STFT on the stray flux has been used as a reliable diagnostic method during the start-up of the induction motor. Figure **??** shows the time-frequency evolution of all frequency components related to broken bar faults. The V-pattern of the $(1-2s)f_s$ is the most characteristic and distinct trajectory proving the existence of a broken bar fault.

2.8 Finite Element Analysis

Finite Element Analysis (FEA) is the computer-based application of the ***Finite Element Method (FEM)*** used to simulate and analyze the behavior of structures, systems, or components under various physical conditions. FEM is a numerical technique that divides a complex object into many smaller, simpler parts called finite elements. These elements are connected at points called nodes, forming a mesh that approximates the original geometry (see Figure 2.25. Partial differential equations are then applied to each element to model physical phenomena such as structural stress, thermal heat distribution, fluid flow, or electromagnetic fields. By solving these equations collectively, FEA predicts how the whole object behaves under load, heat, vibration, or other conditions.

2.8.1 Formulation of FEA problem

Electromagnetic equations

For any FE problem, the foremost step is to formulate the equations that describe the overall physics of the system under study. In electrical machines, the main interest is in the electromagnetic fields that govern their operation. Therefore, the starting point are Maxwell's equations (2.20) - (2.23), representing the four coupled partial differential equations combining the laws of electricity and magnetism. In the equations (2.20) - (2.23), $\mathbf{D}$ is displacement electric field, $\mathbf{B}$ is magnetic flux density vector field, $\mathbf{E}$ is electric field intensity vector field, $\mathbf{H}$ is magnetic field intensity vector field and $\mathbf{J}$ is current density vector field.

$$\nabla \cdot \mathbf{D} = \rho \tag{2.20}$$

$$\nabla \cdot \mathbf{B} = 0 \tag{2.21}$$

$$\nabla \times \mathbf{E} = -\frac{\partial \mathbf{B}}{\partial t} \tag{2.22}$$

$$\nabla \times \mathbf{H} = \mathbf{J} + \frac{\partial \mathbf{D}}{\partial t} \approx \mathbf{J} \tag{2.23}$$

The magnetic vector potential $\mathbf{A}$ is defined as

$$\mathbf{B} = \nabla \times \mathbf{A} \tag{2.24}$$

Using $\mathbf{B} = \mu\mathbf{H}$, where μ is the magnetic permeability of the material, substituting (2.24) into (2.23) one gets

$$\nabla^2 \mathbf{A} = -\mu\mathbf{J} \tag{2.25}$$

Using (2.25), the behavior of the electromagnetic field can be studied for regions where the current density is defined. Substituting (2.24) in (2.22) and further simplifying one gets

$$\mathbf{E} = -\frac{\partial \mathbf{A}}{\partial t} - \nabla V_{pot} \tag{2.26}$$

where V_{pot} is the electric scalar potential. Using the relationship $\mathbf{J} = \sigma \mathbf{E}$, where σ is the electrical conductivity, on (2.26) and adding it to (2.25), one ends up with the final formulation, which will be used in the numerical analysis of electric machinery. In the expression (2.27), ∇V_{pot} represents the voltage applied to the system.

$$\frac{\nabla^2 \mathbf{A}}{\mu} - \sigma \frac{\partial \mathbf{A}}{\partial t} = -\mathbf{J} + \sigma \nabla V_{pot} \tag{2.27}$$

FEA setup procedure

Having obtained the expression (2.27) that describes the physics of the system, the FEM method is used as a mathematical tool to solve them for each finite element (see Figure 2.26. The entire FEA procedure is described in a concise manner below.

Step 1 Generation of machine geometry, typically a sketch of its cross section. A more precise geometry will yield more accurate results.

Step 2 Definition of the different parts of the machine that are made with different kinds of materials and are called components. This step also includes defining the required material properties, if need be.

Step 3 Establishing the circuit configuration of the motor's parts.

Step 4 Determination of the model's mesh size. Choosing the mesh size is a trade-off between solution accuracy and computation time and must be taken into consideration.

Step 5 Choosing the simulation settings, running the simulation, and in the end obtaining the results and studying them.

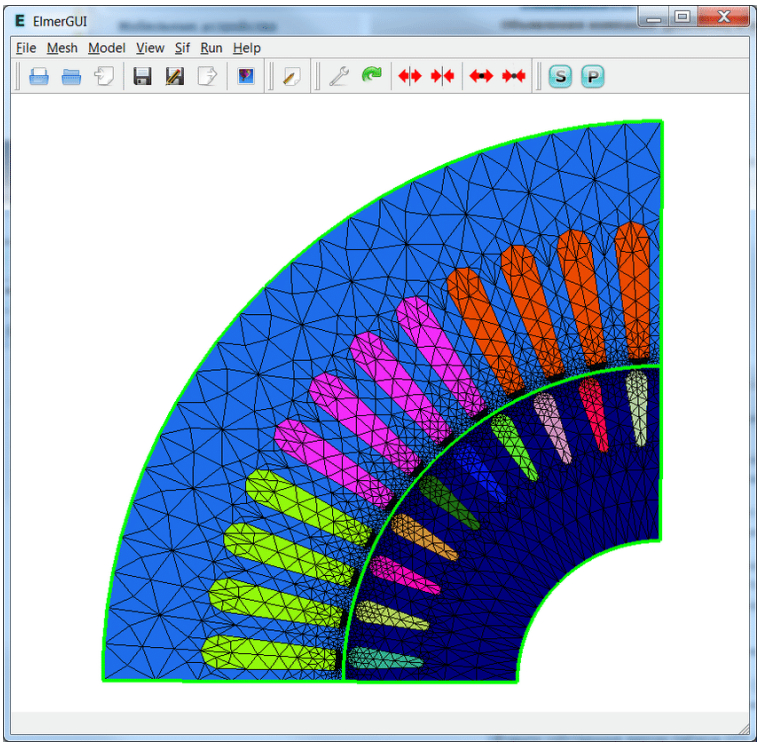

Figure 2.25: Triangular finite element mesh of an IM's cross section [73].

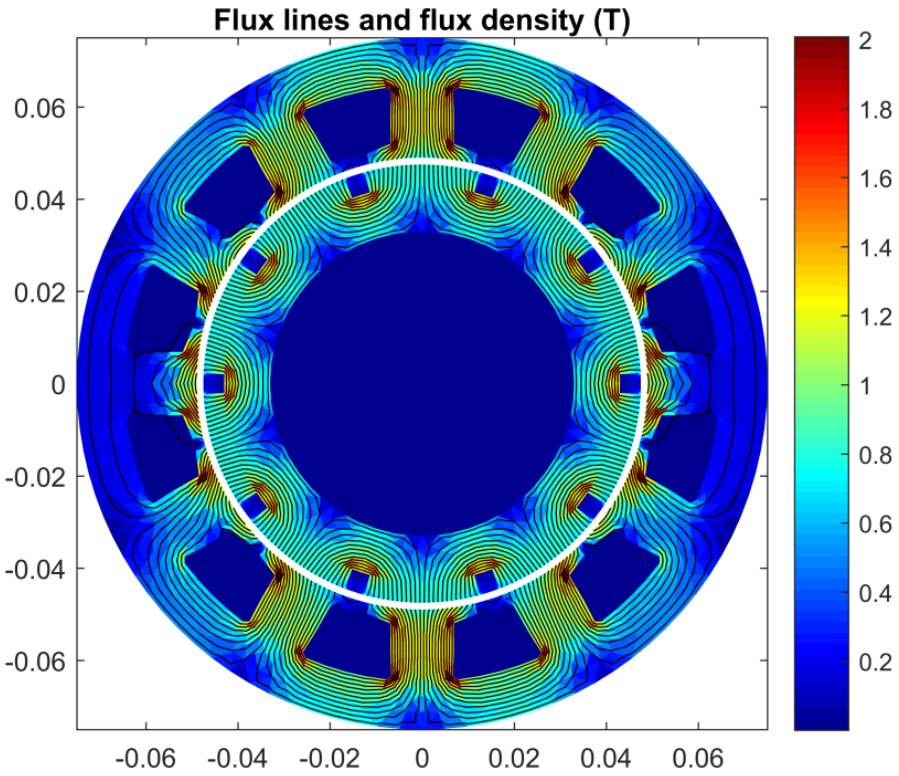

Figure 2.26: magnetic flux density, B, and flux lines, Φ, of an IM as computed by FEA software [74].

Chapter 3

Model Construction & Validation

3.1 FEA Model

The LSPMSM model was developed using four detailed design sheets provided by the manufacturer. These documents include geometric specifications for the stator, rotor, magnet, and winding sequence. Due to confidentiality agreements, the specific details of these sheets will not be disclosed in this thesis.

The software used is Simcenter MAGNET from Siemens AG. It is a low-frequency electromagnetic field simulation solution, using FEA, that is used to predict the performance of motors, generators, transformers, or any component with permanent magnets or coils [75]. The fundamentals of FEA are discussed in Section 2.8.

This section explains how this software was utilized to build an accurate model of the motor. The process is organized into three levels. First, the outline of the motor is drawn using lines, circles, and arcs. The second level then uses the surfaces defined by the above lines to create components of a specific material, i.e. core, air gaps, coils, cage bars, etc. Finally, level three sets the motion component and the simulation parameters necessary for the simulation to begin solving.

To start, a quick explanation of the workspace is given to make the above steps clearer.

3.1.1 Simcenter MAGNET Workspace

In Figure 3.1 the main window is presented, which contains the Simcenter MAGNET working environment. At the top of the window, there is a **Menu bar**, and just below it there is a **Toolbar**. On the center-right, the **View window** is located, where the model is drawn. On the center-left, information about the model is displayed and edited in the pages of the **Project bar**. Between the View window and Project bar another Toolbar is present. All the tools in the toolbars can also be accessed in the Menu bar. Lastly, a **Status bar** is

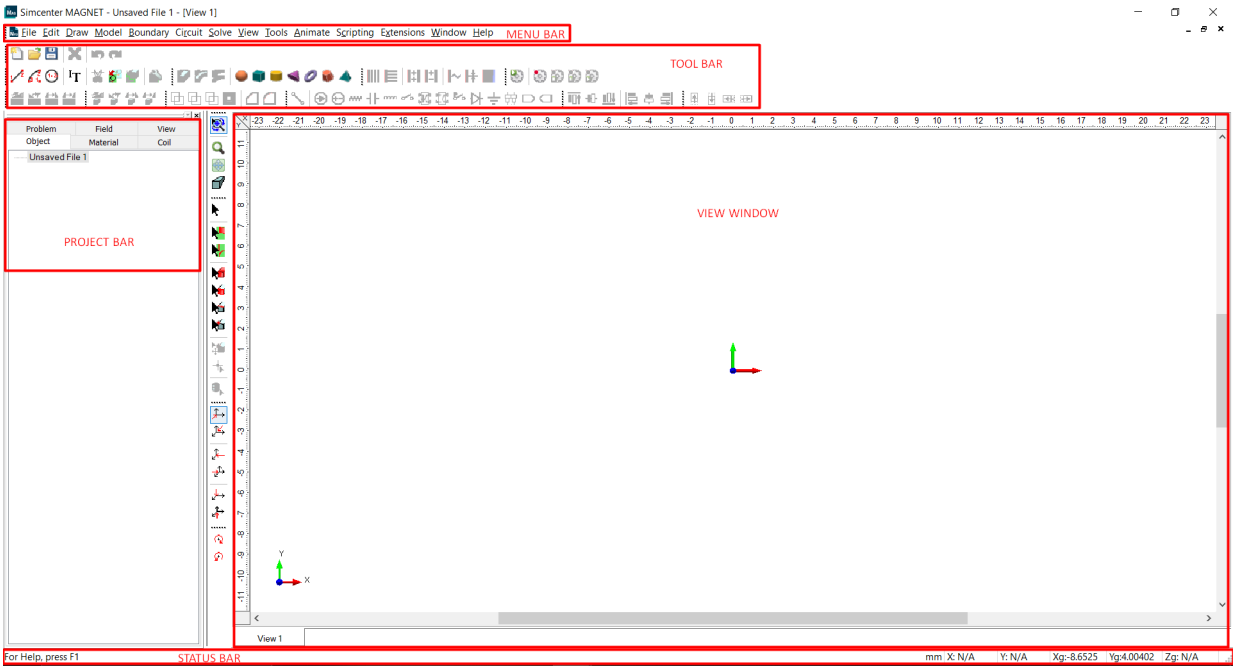

Figure 3.1: Simcenter MAGNET workspace.

displayed at the bottom of the Main window.

The construction of the model started by creating a new file and saving it as LSIPMSM. Then, the Length unit of the model was set from meters (default) to millimeters (**Object -> right click on LSIPMSM -> Properties -> Units -> Length -> millimeters**). This was done for convenience, since the dimensions of the motor are given in mm.

3.1.2 Drawing the Outline of the Motor

Outer and Inner Diameters of the Stator and Rotor.

To start, four circles were drawn (**Draw-> Add Circle**), as depicted in Figure 3.2. The two outer circles define the entire core of the stator. The third circle roughly establishes the core of the rotor. The fourth circle is added as a guide to design later the squirrel cage rotor bars, but in this case, it can be omitted. The center point and radius of these circles were specified using the Keyboard Input Bar, a tool necessary for high precision coordinates (**Tools -> Keyboard Input Bar**).

Stator and Simple Rotor Bar Slots

The design of the stator slot was made simple by the point, line, and angle analysis given in Figure 3.3, for which all coordinates for all points were calculated using the datasheet. It is also noted that Simcenter MAGNET has a tool that can mirror and rotate edges, so only half of the slot was analyzed and drawn.

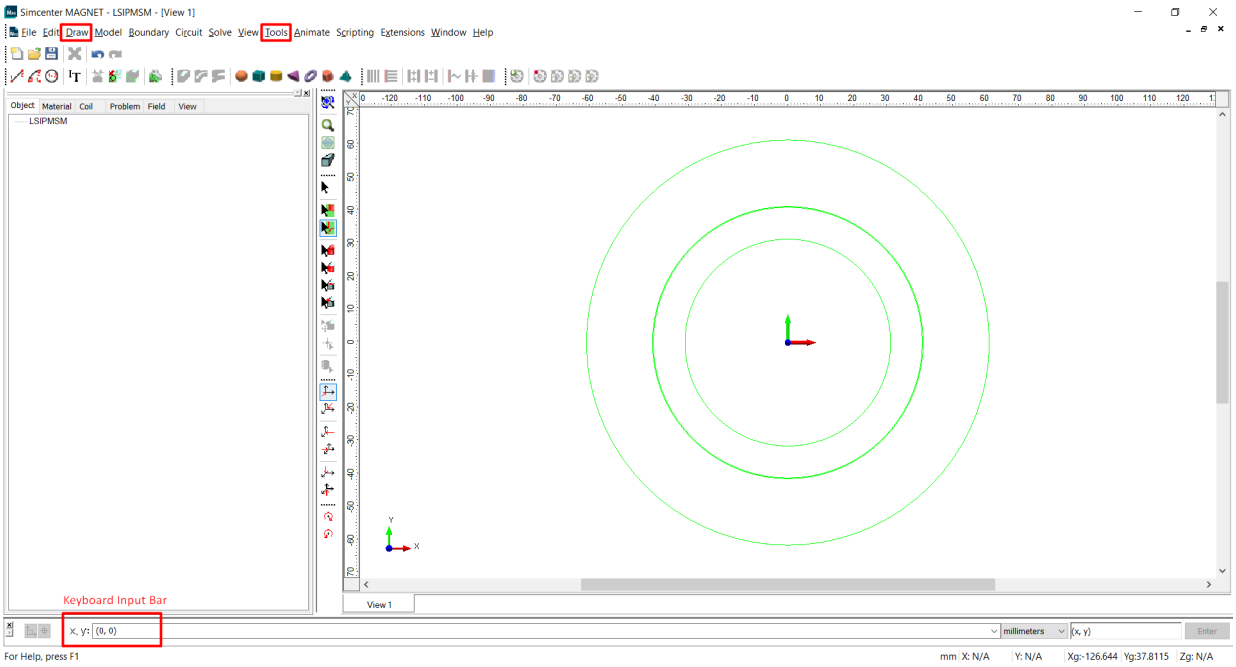

Figure 3.2: Stator's and Rotor's rough definitions.

*Line*12 is a quarter of a circle starting from point $p1$, ending in point $p2$, with the center located at the orthogonal junction of those points, so it was drawn using an arc (**Draw->Add Arc**). The start, end, and center points of the arc were specified using the Keyboard Input Bar. Then *Line*23 and *Line*34 were drawn using a simple line (**Draw->Add Line**). The start and end points of the lines were entered in the Keyboard Input Bar. The result can be seen in Figure 3.4.

For *Line*45 a simple line was also used, but since the point $p5$ cannot be easily computed due to the curvature of the inner stator circle, the endpoint was placed just below the inner stator circle, using the mouse. Then, after using the tool *Segment Edges* on *Line*45 and deleting the protruding line at the end (see Figure 3.5), the half stator slot was successfully connected to the inner stator circle.

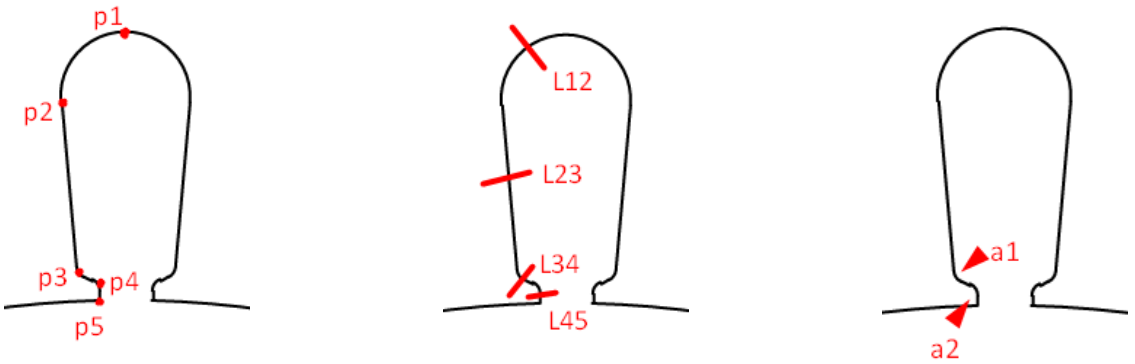

(a) Half stator slot points (b) Half stator slot lines (c) Half stator slot angles

Figure 3.3: Point, line, and angle analysis of a half stator slot.

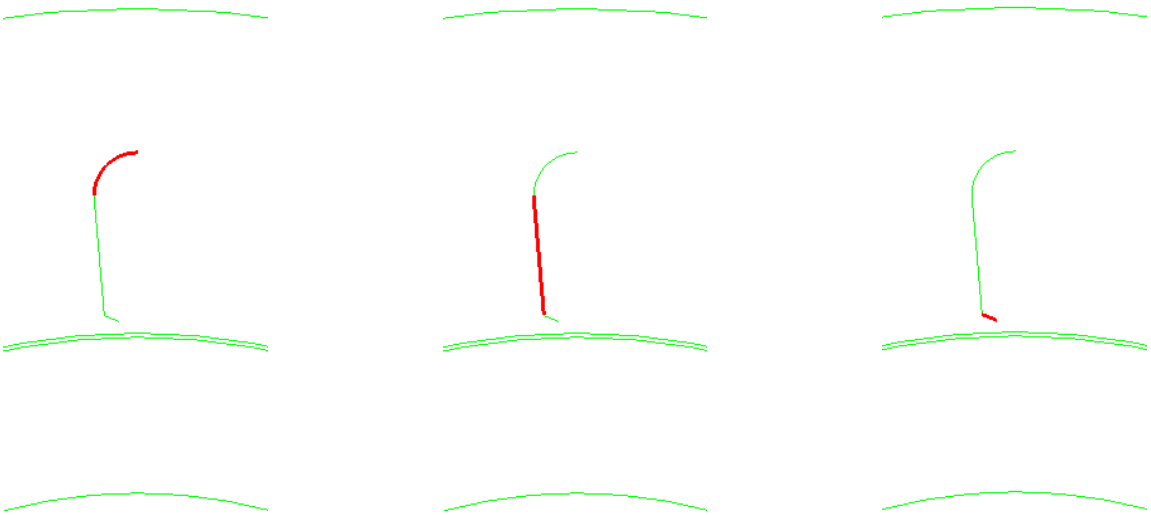

(a) Draw Line 12 (b) Draw Line 23 (c) Draw Line 34

Figure 3.4: First three lines of stator slot drawn in MAGNET.

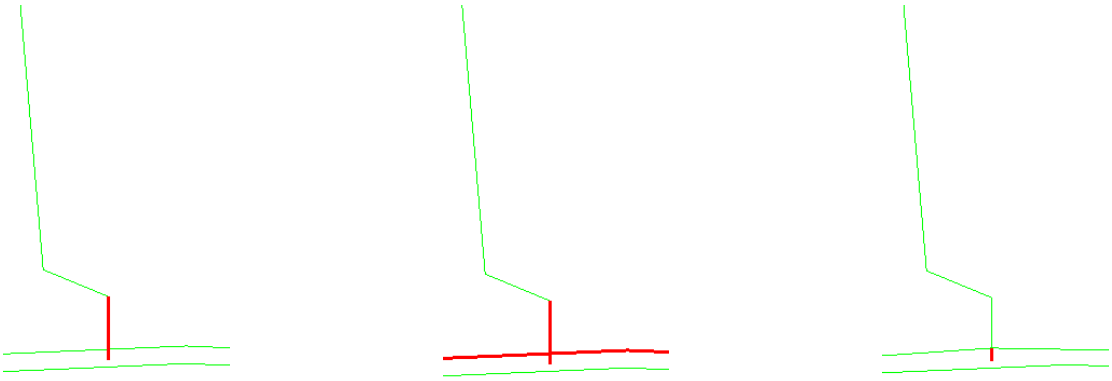

(a) Draw Line 45 (b) Segment selected edges (c) Delete protruding line

Figure 3.5: Fourth line of stator slot drawn in MAGNET.

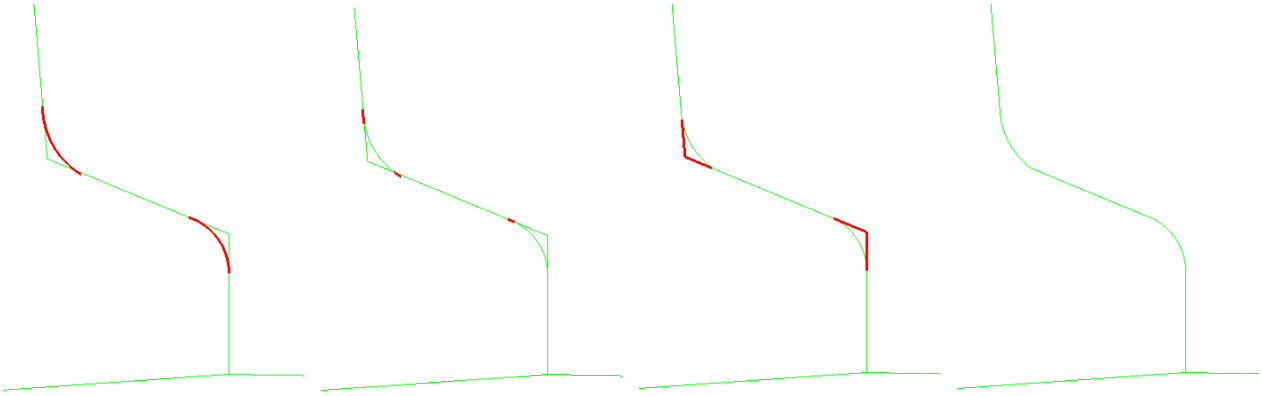

(a) Draw Arcs (b) Delete arc edges (c) Delete line edges (d) Rounded angles

Figure 3.6: Smoothing process of stator slot's angles.

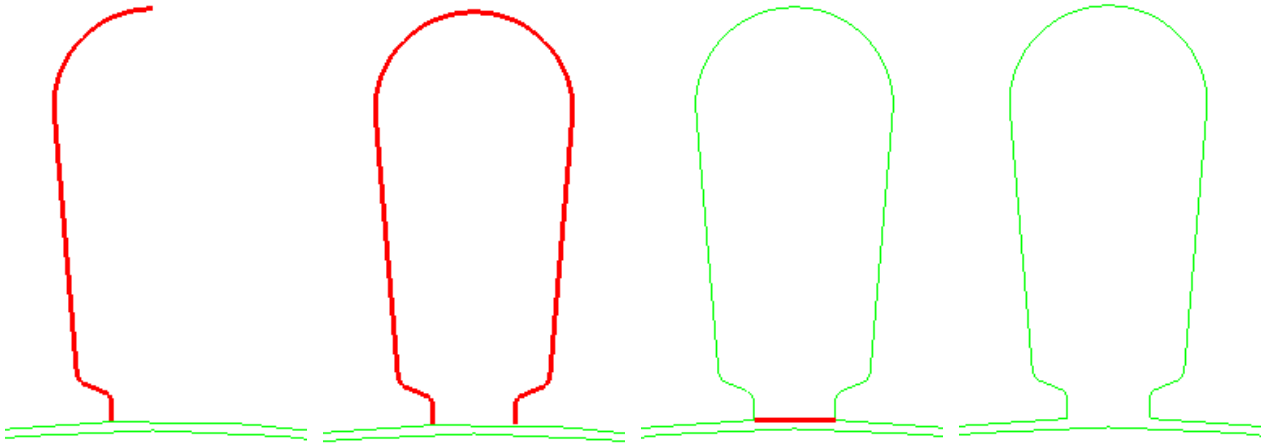

(a) Complete half slot (b) Mirrored half slot (c) Slot base (d) Complete stator slot

Figure 3.7: Completion of one stator slot design.

The two angles seen in Figure 3.5c are sharp compared to the rounded angles of Figure 3.3c. The error of that difference is very small and would not significantly affect the results of the simulation. However, to make the model as true to the original design as possible, arcs were used to round them as shown in Figure 3.6a. Then *Segment Edges* was used to sever the lines at the points of crossing each other, and the unwanted lines (see Figure 3.6b,3.6c) were selected and deleted.

The complete half-slot is shown in Figure 3.7a. To obtain the entire stator slot, the half slot was mirrored to the y-axis, with the tool *Mirror Edges*. The base of the slot was deleted using *Segment Edges* again. The result of a single slot of the stator is presented in Figure 3.7d.

The software also has the tool *Rotate Edges* to rotate or/and copy a selected edge. This tool was used to draw all remaining slots in the stator, rotating the slot of Figure 3.7 at an angle of $360^o/\#statorslots$ each time.

The rotor bar slots were drawn following the same process as above. The stator and rotor with all their winding slots are shown in Figure 3.8.

Eccentric Rotor Bar Slots, Permanent Magnet Slots and Shaft

The rotor has more slots in addition to its cage bar slots. The machine is a 4-pole permanent magnet synchronous motor, so it will also have slots for the magnets. There is also a void for the shaft that will support the entire rotor. Lastly, eight of the 44 rotor bars, two per pole, have an eccentric design compared to the simple rotor bar, acting as flux barriers (see Section 2.4 on flux barriers).

All the gaps mentioned above were drawn using the same techniques as the stator slot

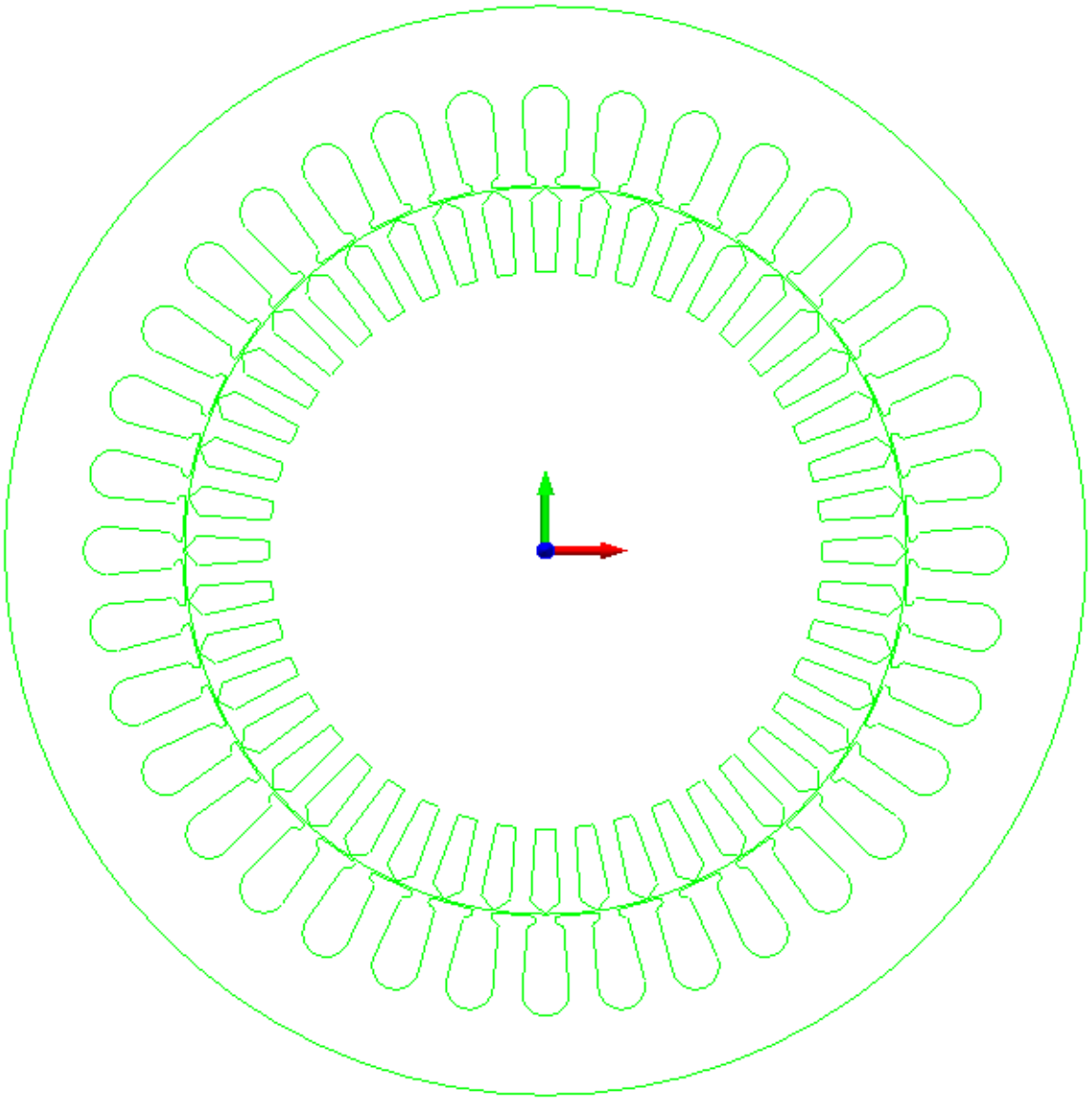

Figure 3.8: The complete stator and rotor winding slot design.

method. First, rough edge slots were created using already calculated points, pivot lines, and the tool *Segment Edges*. Then arcs were used to curve the angles. Where possible, only half of the drawing is made to simplify the calculations and the number of design steps by using *Mirror Edges* and *Rotate Edges*. The final result can be seen in Figures 3.9, 3.10, 3.11.

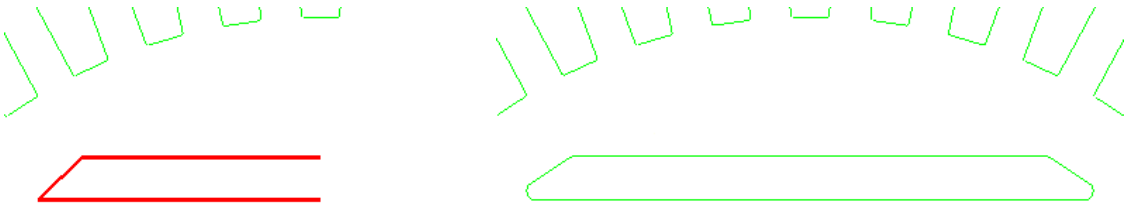

(a) Half magnet slot (b) Complete magnet slot

Figure 3.9: Drawing of one permanent magnet slot.

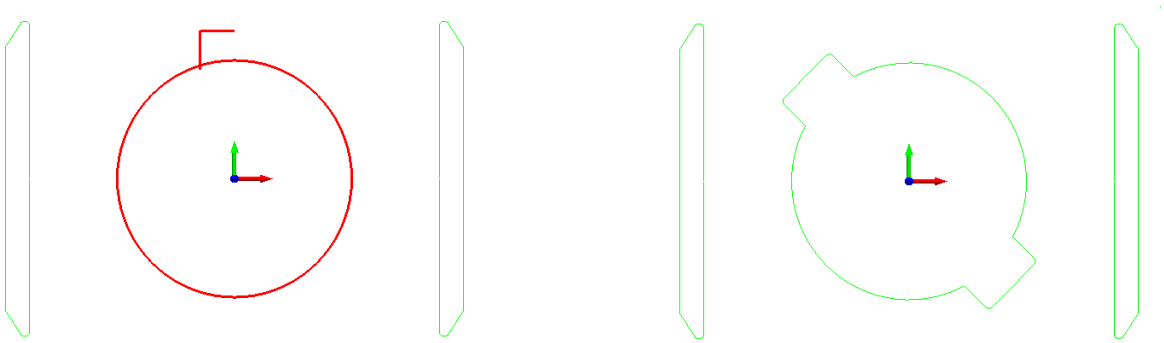

(a) Shaft pivot lines (b) Complete shaft

Figure 3.10: Drawing of the motor's shaft.

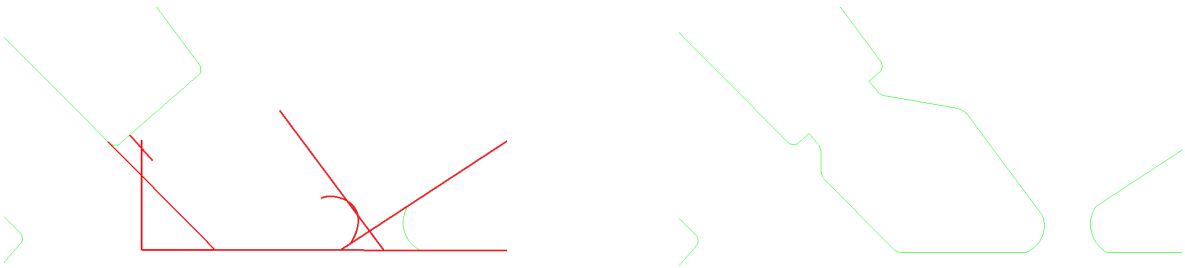

(a) Eccentric rotor bar pivot lines (b) Complete eccentric rotor bar

Figure 3.11: Drawing of one eccentric-shaped rotor bar slot.

Stator Windings, Magnets, and Flux Sensors

Simple parallelograms were drawn to represent the motor coils and magnets, as shown in Figure 3.12a. Place 1 shows two rectangles that act as the two terminals of one sensor. Three identical sensors were also placed at plus 60^o, 120^o, and 240^o degrees clockwise relative to the first. Place 2 shows the windings of the stator, while place 3 shows the permanent magnet.

Air Gap Modeling and Air Box

The air gap between the stator and the rotor must be divided into multiple layers to accurately calculate the air gap parameters, which are important in electrical machine design and condition monitoring. Usually, three layers are used, but in this particular case, four layers were chosen to achieve higher precision in the FEM solution. The layers were created by drawing 3 circles between the inner stator circle and the outer rotor circle, equally dividing the free space. The result is shown in Figure 3.12b.

The last step of the design process was to add a circle surrounding the whole motor, which will serve the purpose of an air box. The whole motor design is shown in Figure 3.13.

3.1.3 Definition of Motor's Materials, Coils, and Components

To complete the model, it is necessary to establish its composition. The edges drawn in Section 3.1.2 create areas that will be defined as the components of the model, and each will be of the respective material. Simcenter MAGNET already has a list of commonly used materials, but there is also the option of creating a new material if necessary.

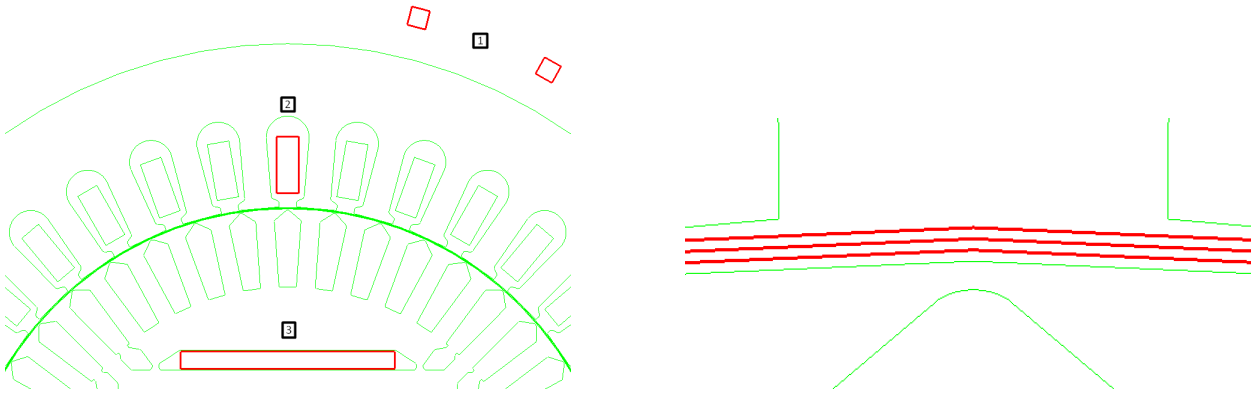

(a) (b)

Figure 3.12: Drawing of (a) stator windings, magnets and flux sensors and (b) air gap modeling.

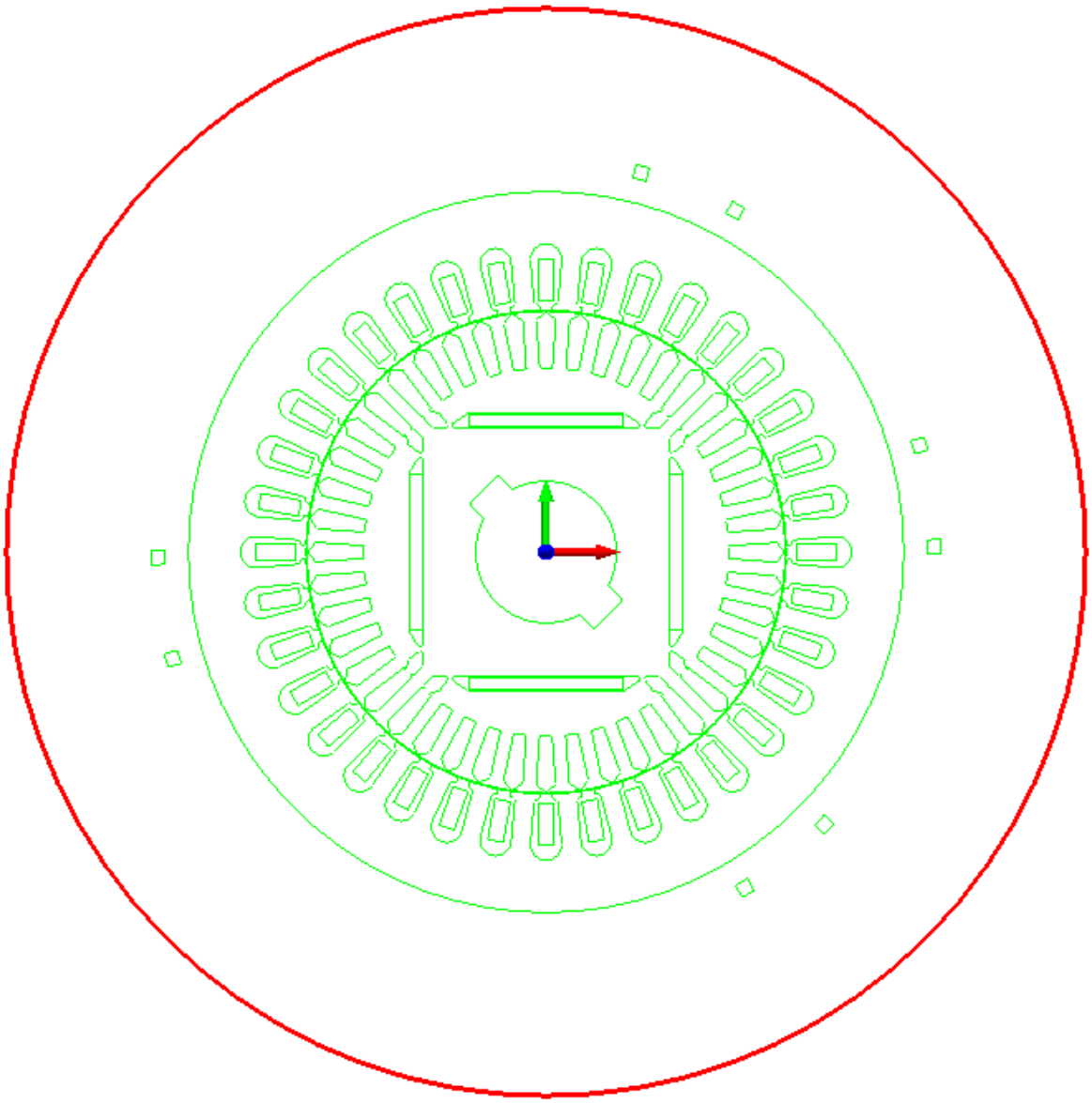

Figure 3.13: Final LSPMSM motor design in SimCenter MAGNET.

Stator and Rotor Components

The stator and rotor are made from the same ferromagnetic material that is not in the materials library of the software. To add it to the already existing list of materials, the tool *New User Material* was selected. In the pop-up window, data about the magnetic permeability (B-H characteristic) and iron loss was requested, which was given by the manufacturer.

The surface that defines the desirable component can be selected by *Select Construction Slice Surfaces*. The stator area was first marked before choosing the *Make Component in a Line*. Then the name, material and the length of the core were chosen as shown in Figure 3.14a. The same was done for the rotor core.

Shaft, Magnet Slot, Air Gap and Surrounding Air Components

The shaft slot, magnet slot, and air box components were created using the AIR material from Simcenter MAGNET's material library.

The air gap consists of four components, one for each layer. For the two inner layers, the AIR material was chosen, while the two outer layers were made with the Virtual Air material. Virtual Air is a material in the Simcenter MAGNET material library that has the same properties as the material AIR. The Virtual Air material can be used, for example, to compute forces on coils or to view shaded or arrow plots on surfaces that would not otherwise be available.

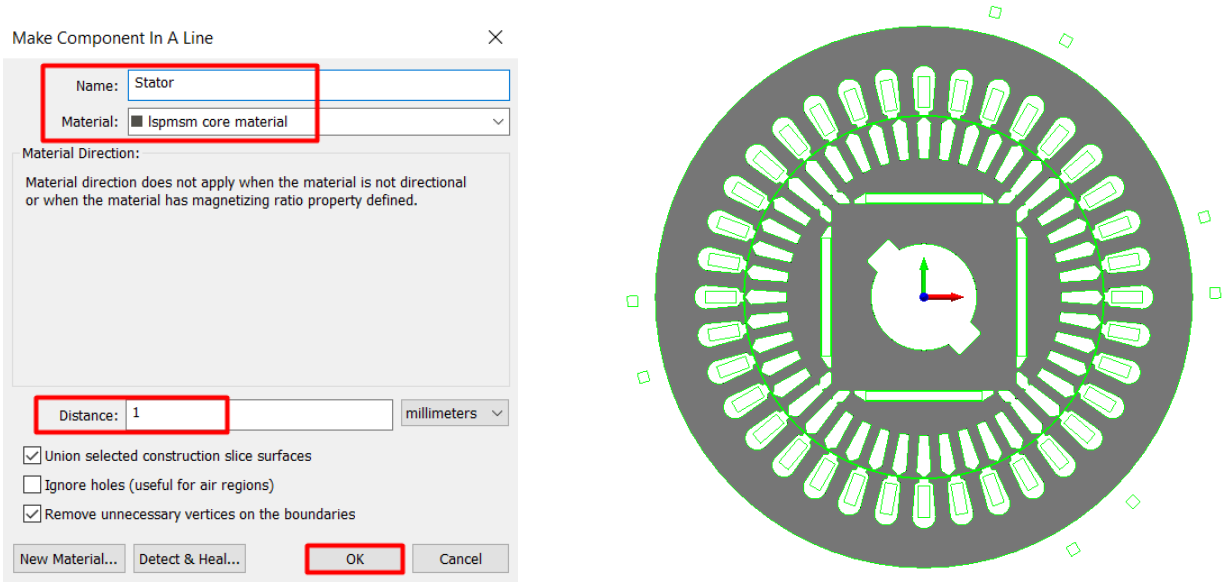

(a) *Make Component In a Line* window (b) Stator and rotor components

Figure 3.14: Process of making a component in Simcenter MAGNET.

Flux Sensor & Stator Winding, Rotor Bar and Magnet Components

The Sensor and Stator Winding Components were made with "Copper: 5.77e7 Siemens/meter" while the Rotor Bar Component was made with "Aluminum: 3.8e7 Siemens/meter". The magnet's neodymium grade was already in MAGNET's list of materials. All of the above components created can be seen in Figure 3.16, where copper is marked in orange, aluminum is light gray, and neodymium is light blue.

After creating the above, the edges (green outline) of the model are no longer needed, so they were all selected and deleted, leaving only the components.

Stator, Rotor and Flux Sensor Coils

The next step was to define the coils of the motor using the *Make Simple Coil* tool. The sequence in which the coil terminals are selected determines the current flow through the terminal. The first to be chosen will have current flow $\odot$, while the other $\otimes$, which is displayed on the terminal components.

The Properties window of the coil of one of the magnetic flux sensors is shown in Figure 3.15. The type of this coil is *Stranded*, and the number of turns was chosen to be 1000. The same properties hold for the other 3 sensors.

Each stator phase winding was also modeled by 6 simple stranded coils connected in series, following the winding connection data sheet given by the manufacturer. Finally, since the rotor has a squirrel cage, it will have as many coils as its bars, so 44 solid-type coils.

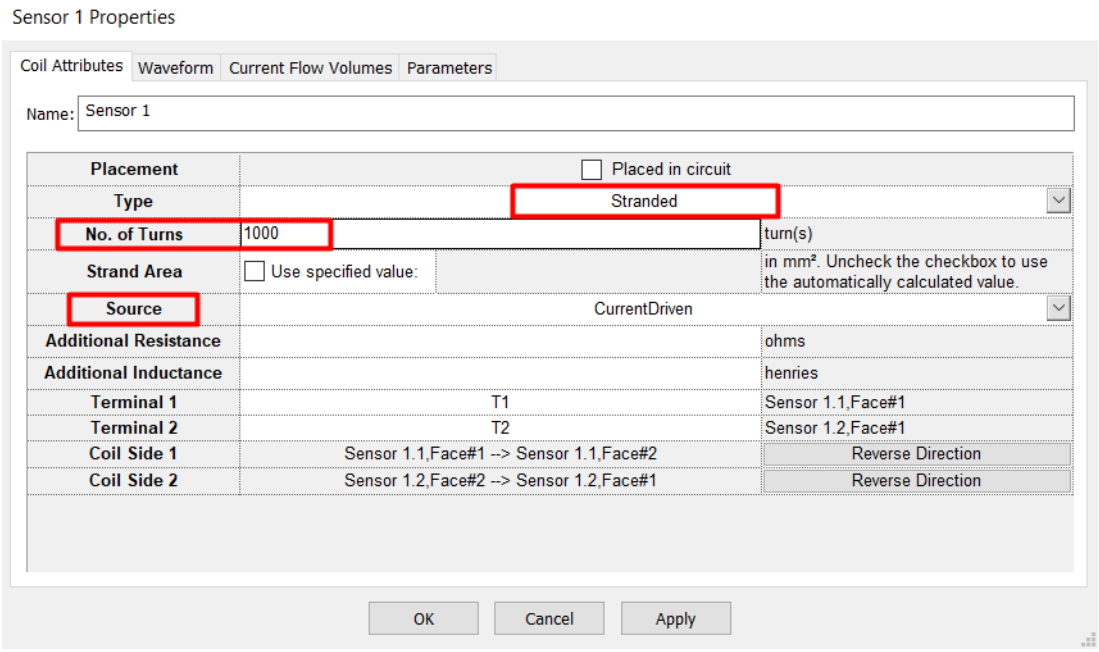

Figure 3.15: Flux sensor's coil properties window.

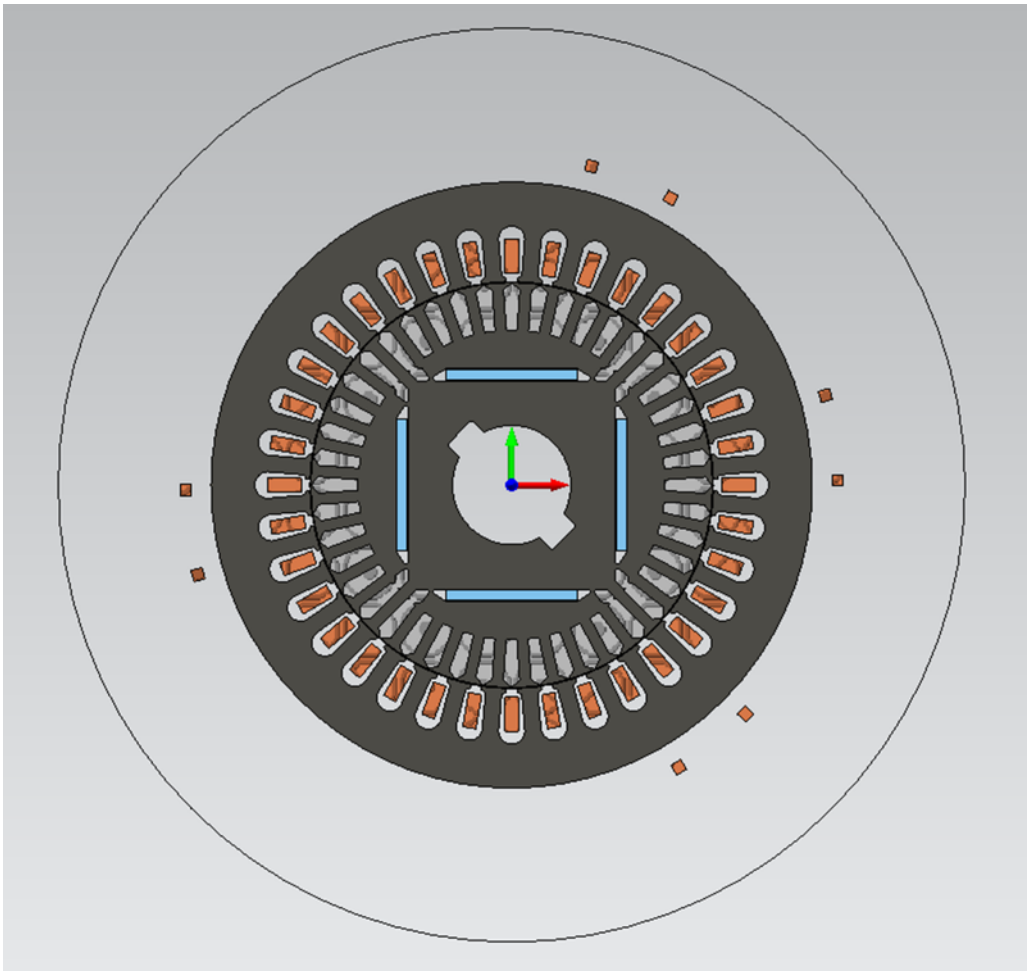

Figure 3.16: Final motor's design with components.

Motion Component

As the name suggests, the motion component consists of all the moving components of this machine: the shaft, the rotor's ferromagnetic core, the PMs & PM slots, the rotor bars, and lastly the two air-gap layers above the rotor. It was made by selecting all the above components and then using the *Make Motion Component* tool. In the General tab of the parameter window, the motion source type was selected to be *Load driven*, and the motion type *Rotary*. Lastly, in the Load tab, the load of the motor was selected to be constant and nominal at $-4.78Nm$ (see Figure 3.17).

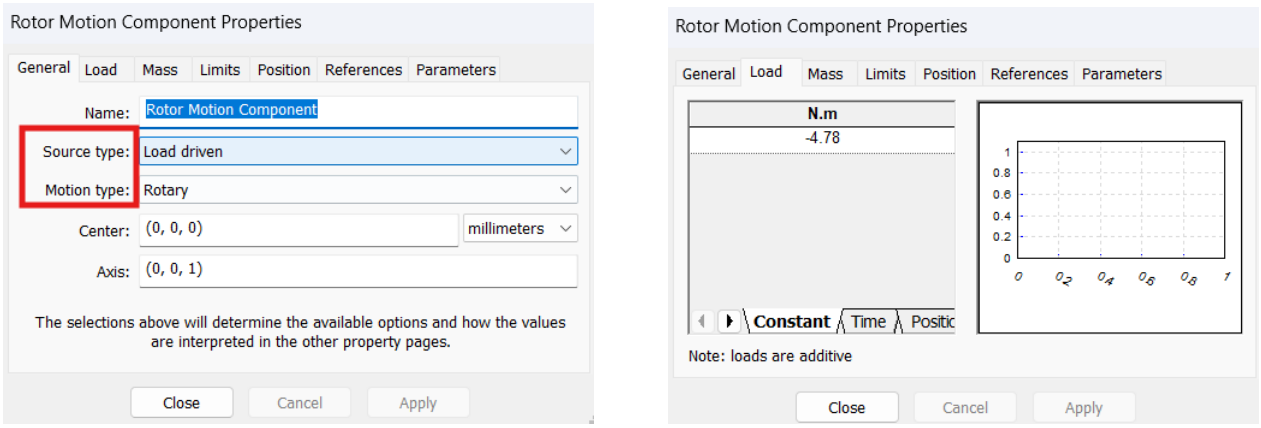

(a) General tab

(b) Load tab

Figure 3.17: Motion Component window.

3.1.4 Circuit Connection and Simulation Settings

The six coils of each phase were first connected in series together with a resistance of 9.9 kOhm. That was the stator's one-phase resistance measured after the motor in the laboratory had been running for several hours. Then all phases were connected in star configuration with a 3-phase voltage source of $400V$, $50Hz$, as illustrated by Figure 3.18. The rotor's 44 coils were all connected in parallel like in Figure 3.19(a). For convinience, only the first set of 4 coils is shown. Lastly, for each sensor coil, a resistance of $1TOhm$ was chosen to model an open circuit (see Figure 3.19(b)).

The number of finite elements for which MAGNET is going to solve the electromagnetic equations 2.8.1 is determined by the mesh of the model, which can be illustrated by right-clicking on any model location and choosing *Initial 2D Mesh*. The default mesh of the model is too coarse (see Figure 3.20(a)), resulting in a less accurate solution, especially regarding the air-gap quantities. So in the Mesh option of the model's properties, the *Maximum element size* was chosen to be 5mm. The improved resolution of the mesh is clearly shown in Figure 3.20(b).

The last step before starting the solving process was to set the parameters of the simulation

through the *Transient Options* window in the *Solve* tab of the menu bar (see Figure 3.21. In the field *Time stem method*, it was defined that the simulation will start from $0ms$ and will virtually run for $7000ms = 7s$ with a time step of $0.1ms$. In the window on the right that is titled *Field solution storage options*, one can choose at what time to store the field solution of the simulation, which is going to be the cross section of the machine with all the relevant quantities illustrated on it, like the magnetic flux lines and magnetic flux density etc. A snapshot at $50ms$ (transient phase), $6900ms$ (steady state-first half cycle) and $6910ms$ (steady state-second half cycle) will be taken for this thesis.

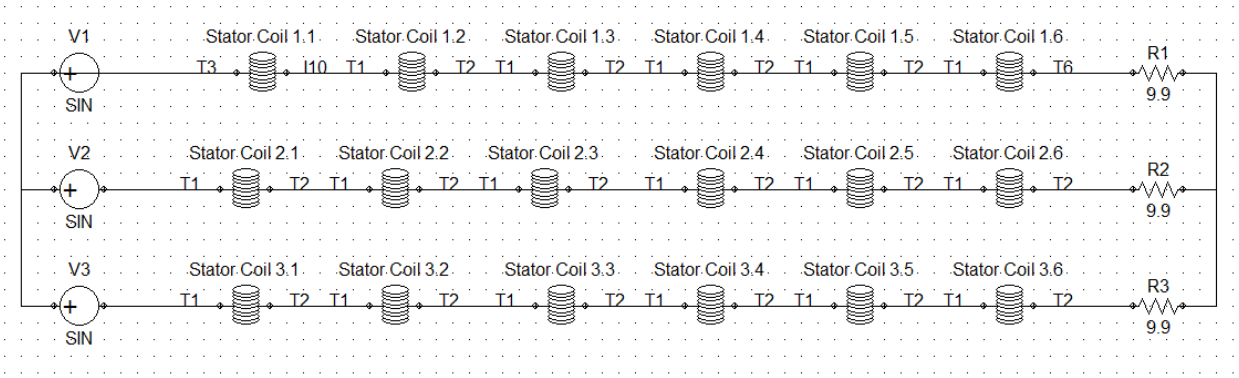

Figure 3.18: The stator's circuit in Simcenter MAGNET.

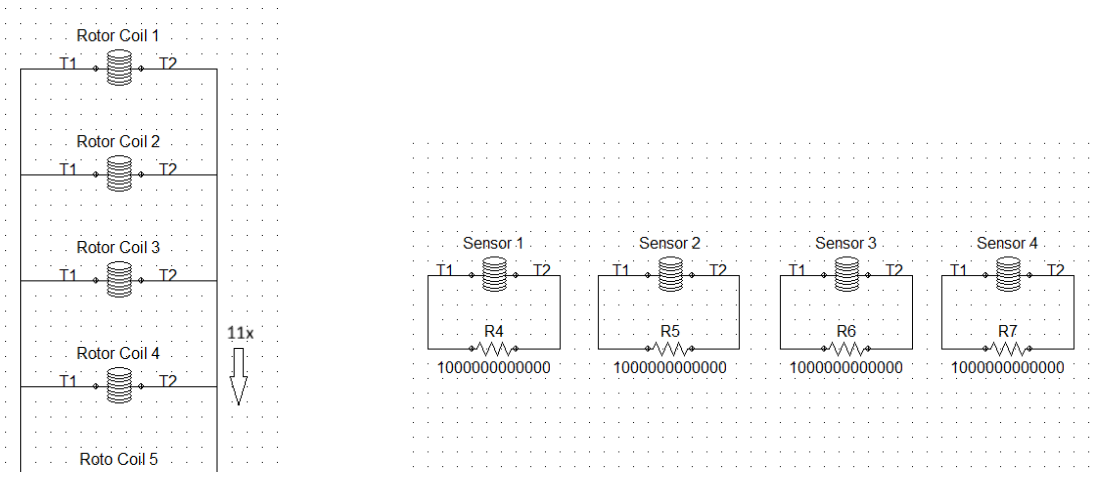

(a) (b)

Figure 3.19: (a) The rotor's squirrel cage circuit, and (b) the stray flux sensor circuits in Simcenter MAGNET.

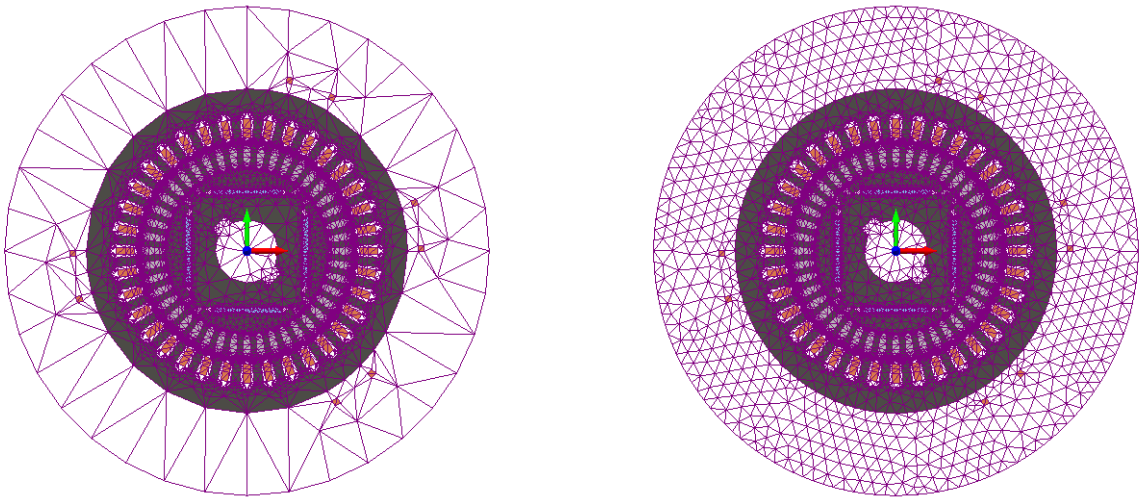

(a) Default mesh. (b) Improved mesh.

Figure 3.20: The 2D Mesh of the model.

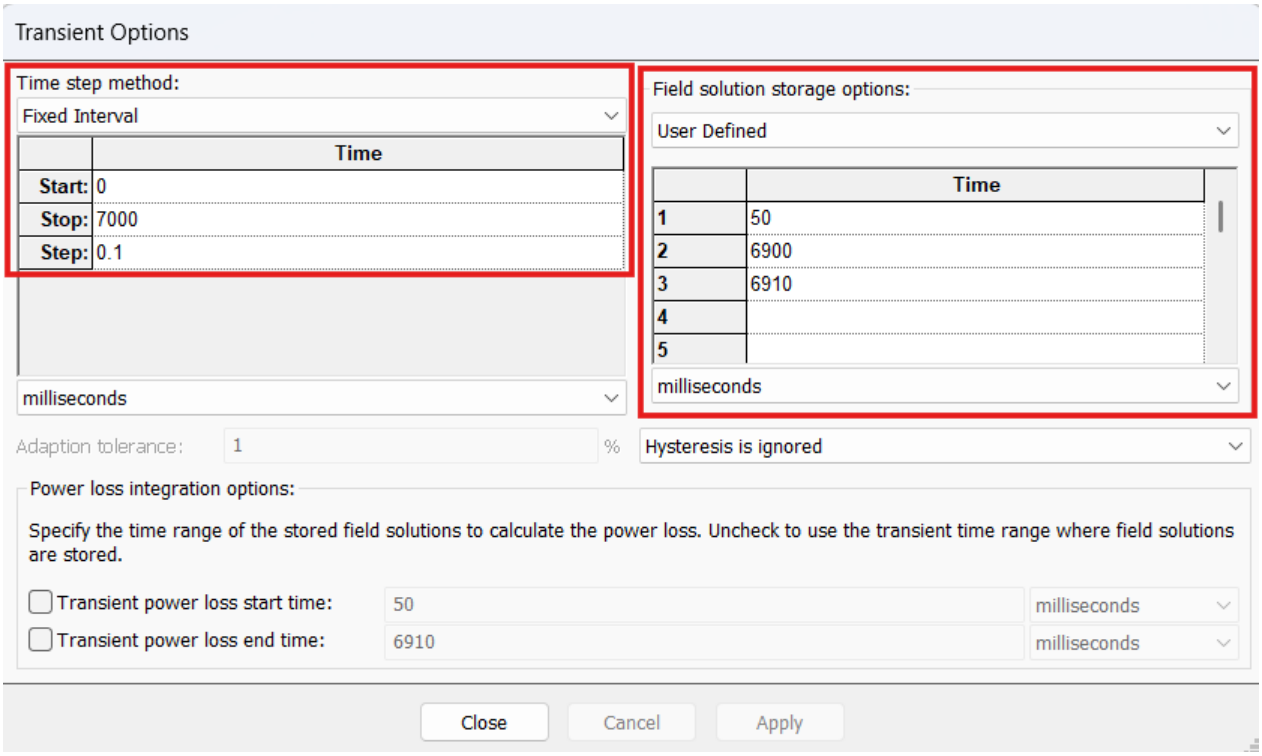

Figure 3.21: Transient Options tab for setting up the simulation time step and duration, and the field solution snapshot.

3.2 Model Verification

3.2.1 Simulation results and experimental validation

Simulation Conditions

The healthy FEA model was simulated with a balanced three-phase 400 V, 50 Hz voltage supply in a star-connected configuration and operated under a rated load of 4.78 Nm. The simulation was carried out for a total duration of seven seconds using Simcenter MAGNET, with a time step of 0.1 seconds to achieve an optimal balance between accuracy and computational efficiency. For reference, the motor nameplate, which contains the operational characteristics, is provided in Figure 3.22.

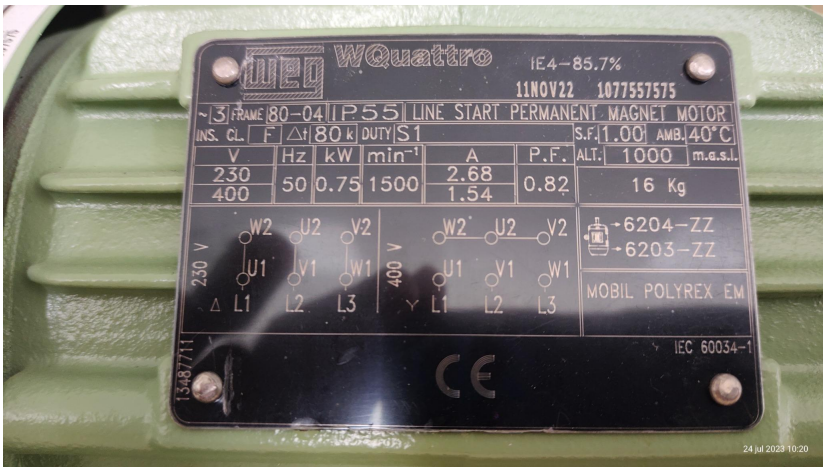

Figure 3.22: Motor nameplate.

FEA Motor Performance Results

The performance of the simulated hybrid motor is presented in Figure 3.23. Then Table 3.1 compares the rated load characteristics provided by the manufacturer with those obtained by simulation. Specifically, from left to right are the stator RMS phase current ($\mathbf{I_{a,rms}}$), mechanical output power ($\mathbf{P_m}$), electrical input power ($\mathbf{P_e l}$), rated load ($\mathbf{T_m}$), synchronous speed ($\mathbf{n_s}$), PF ($\mathbf{\cos \phi}$) and efficiency ($\boldsymbol{\eta}$).Overall, the results are satisfactory, with deviations observed in the stator current, PF, and efficiency. Despite these discrepancies, the rotor reached synchronous speed while delivering the nominal torque at the nominal load.

A large part of the difference observed in motor quantities in Table 3.1 can be attributed to the 2D nature of the simulation. As shown in Section 3.1, the 2D approach completely disregards the influence of the end rings, which would have been considered in a 3D simulation. Therefore, a 3D analysis would have yielded results much closer to the rated data, with minor discrepancies, primarily due to manufacturing asymmetries [76]. These include:

- static and dynamic eccentricity faults,
- iron core porosity,
- stator windings imbalances,
- magnetic anisotropy,
- lamination faults,
- insulation coating faults,
- machining faults,
- power supply imbalances,
- and others.

To add to the above, the influence of temperature was not included in the simulation. The model assumes operation at a constant temperature of 20°C throughout, which may not accurately reflect real-world conditions. Additionally, the dynamic behavior of the stator resistance, particularly during transitions from startup to steady state, was not accounted for. The stator phase resistance used in the circuit FEA modeling of the motor was measured in the lab after operating the motor for several hours.

	$\mathbf{I_{a,rms}(A)}$	$\mathbf{P_m(W)}$	$\mathbf{P_{el}(W)}$	$\mathbf{T_m(Nm)}$	$\mathbf{n_S(rpm)}$	$\cos\phi$	η
Rated	1.54	750 W	874.89 W	4.78	1500	0.82	85.7 %
FEA	1.30	750.84 W	832.29 W	4.78	1500	0.93	90.21 %

Table 3.1: Rated performance comparison between real motor and FEA model.

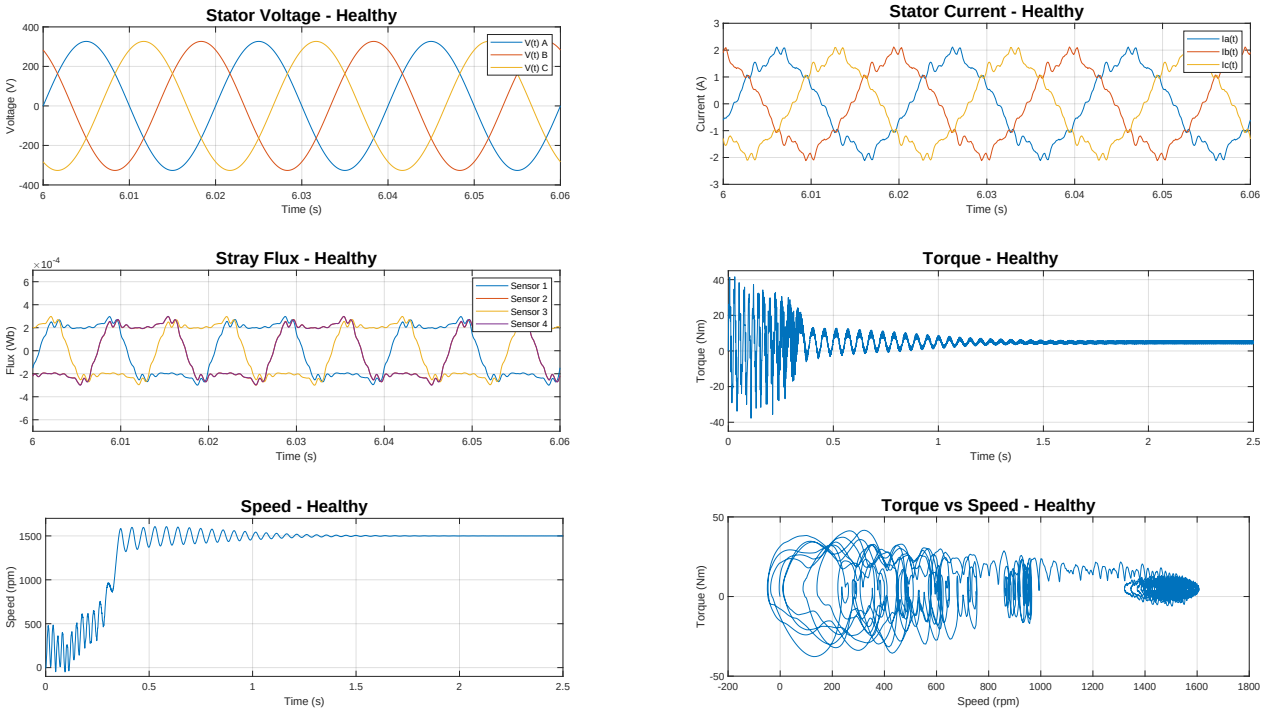

Figure 3.23: Healthy FEA model signals.

FFT Steady-State Analysis

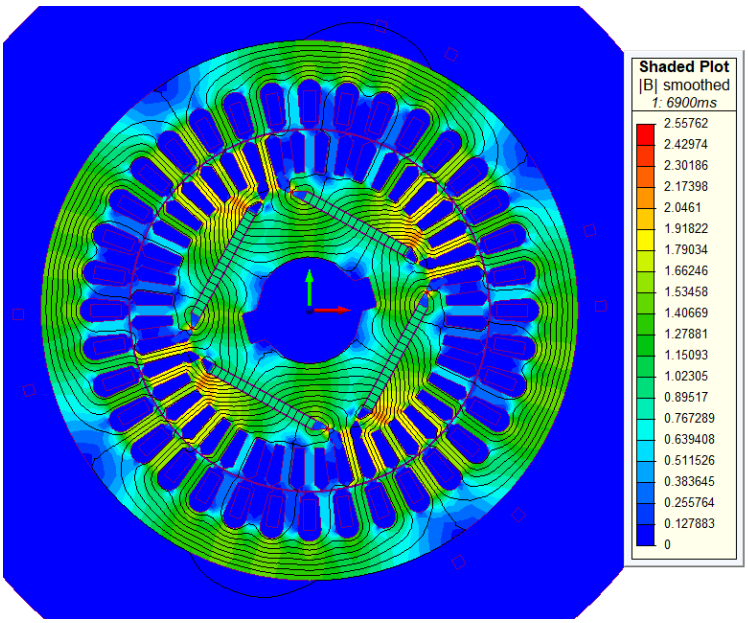

Figure 3.24: Magnetic Flux density of healthy FEA motor.

The single-sided spectra of the steady-state stator current, stray flux, torque, and speed of the healthy FEA model are presented in Figure 3.25.

The first harmonics to be observed in the current spectrum are space harmonics. These harmonics are produced due to the stator MMF and the non-linearity of the iron core. Their

rank is given by $6k \pm 1$ and they are also present in the flux spectrum. Typically, their amplitude decreases as their order increases [77].

However, that is not exactly the case here; topically, some space harmonics are stronger than expected across the spectrum. This phenomenon occurs due to their coincidence with the *Rotor Slot Harmonics (RSH)*, slip-dependent frequency components commonly observed in induction motors. These harmonics result from spatial asymmetry caused by the presence of rotor slots and their interaction with the stator magnetic field [77]. The RSH are given by:

$$f_{RSH} = \left[k\frac{N_R}{p}(1-s) \pm n \right] f_s \tag{3.1}$$

where $\mathbf{k} \in \mathcal{N}$, $\mathbf{N_R}$: rotor slot number, $\mathbf{p}$: pole pairs, $\mathbf{s}$: slip, $\mathbf{n}$: stator MMF rank and $\mathbf{f_s}$: supply frequency. For $k = 1$, the above equation also gives the *Prinsipal Slot Harmonics (PSH)* of the motor. Those occur naturally if the rotor slot number is an even multiple of the number of poles [78]:

$$N_R = 2p\left[3(m \pm q) \pm r\right], \qquad m \pm q = 0, 1, 2, 3..., r = 0, 1 \tag{3.2}$$

which is the case in this motor since $N_R = 11 \cdot p = 44$.

The special rotor geometry must be considered to continue the analysis. It consists of 44 slots - 36 similar short slots and 8 deeper unique slots - enhancing the saliency of the rotor. For each of those numbers, Equation 3.1 yields a pair of RSH.

For $k = 1$, $s = 0$, $n = 1$ and $N_R = 44$ Equation 3.1 yields **1050 Hz** and **1150 Hz**, with respective amplitudes -71.35 dB, -28.99 dB in the current spectrum and -26.88 dB, -34.86 dB in the flux spectrum. The 1050 Hz harmonic is homopolar, and since the stator winding is star-connected, it is weaker in the current spectrum.

For $N_R = 36$ slots, the formula gives **850 Hz** and **950 Hz**. Their amplitudes are -26.99 dB and -36.37 dB in the current spectrum, -31.30 dB and -28.57 dB in the flux spectrum.

Similarly, the 8 rotor slots give harmonic frequencies **150 Hz** and **250 Hz**, with amplitudes of -80.02 dB and -22.39 dB in the current spectrum, which explains the weak presence of 3k harmonics in the current.

Finally, the stator harmonics at **850 Hz** and **1150 Hz** react with the fundamental rotor harmonic, producing torque pulsations at **900 Hz (-32.70 dB)** and **1200 Hz (-30.56 dB)**.

Harmonic (Hz)	Stator Current Spectrum	Stray Flux Spectrum
150	-80.02 dB	-8.29 dB
250	-22.39 dB	-18.60 dB
350	-25.71 dB	-33.75 dB
550	-37.46 dB	-52.30 dB
650	-33.31 dB	-41.90 dB
850	-26.99 dB	-31.30 dB
950	-36.37 dB	-28.57 dB
1050	-71.35 dB	-26.88 dB
1150	-28.99 dB	-34.86 dB

Table 3.2: Harmonics' amplitude in the stator current and flux spectrum.

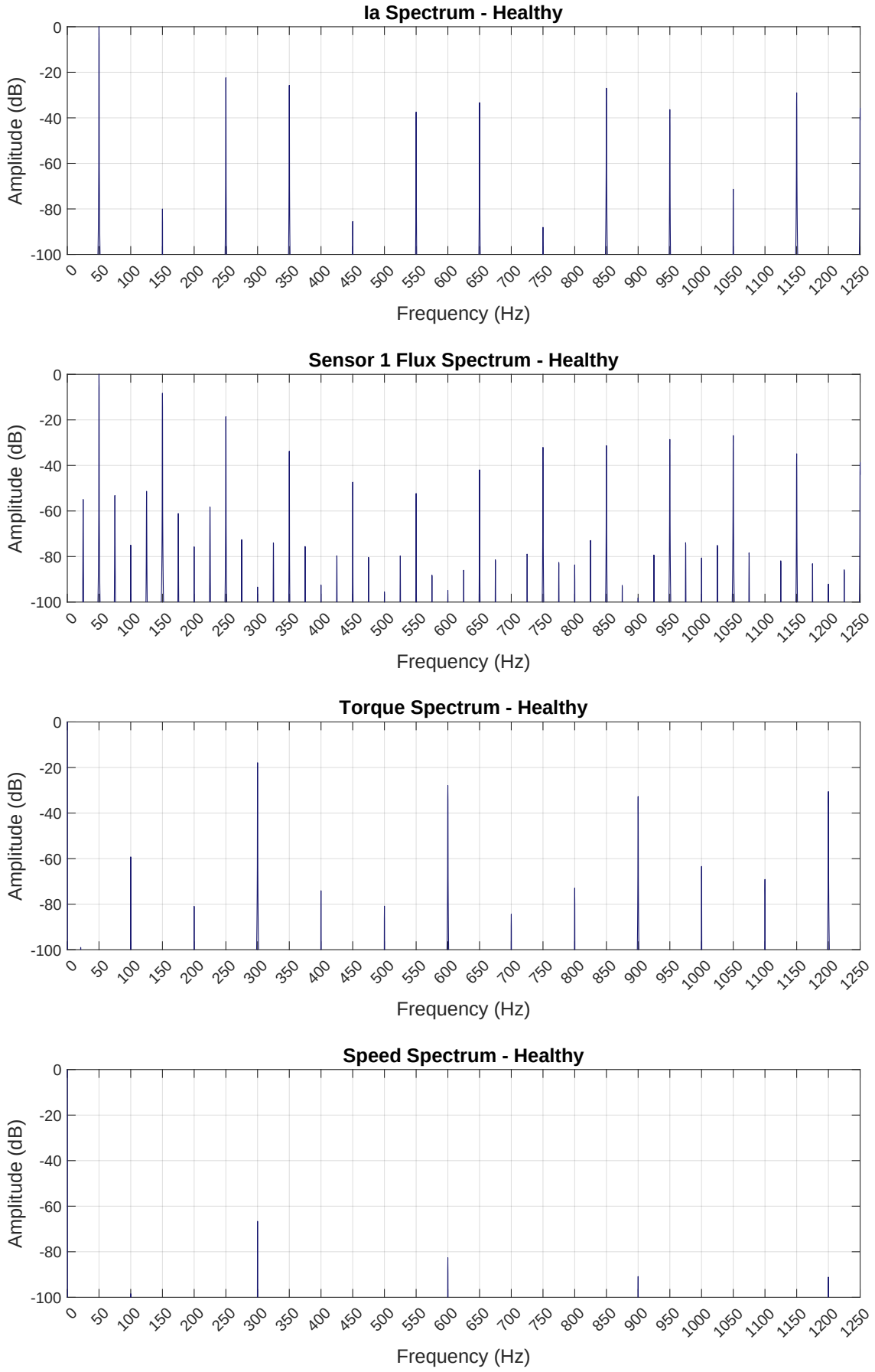

Figure 3.25: FFT of stator current, stray flux, torque, and speed of healthy FEA model.

Comparison with experiment data

Our associates at the University of Valladolid conducted an experiment with a real hybrid motor to validate the FEA model. The acquired stator current, stray flux, torque and speed spectra are shown in Figure 3.26, also containing the simulation results for reference.

Generally, the harmonic content predicted by the simulation agrees with the experimental results. Most of the $6k \pm 1$ space harmonics' amplitude is very satisfying, with an exception for **1050 Hz**, which has reached a high amplitude of **-20.11 dB** in the current spectrum and **-17.05 dB** in the flux spectrum. There is a **54 dB and 10 dB difference**, respectively, from those in the simulation. That dramatic change in the current spectrum is also observed for **150 Hz, 450 Hz, and 750 Hz**, frequencies that are an odd multiple of 3. When a *balanced three-phase system* is star connected, the $3k$ harmonic currents do not flow in the line currents because their line currents are in phase and cancel out. However, these harmonics can still exist in the phase currents and the magnetic field. Real healthy motors will always have low-level inherent asymmetries, such as stator windings, magnetic anisotropy, supply imbalances, etc., which produce a slightly imbalanced system. Hence, $3k$ harmonics are notably present in the experimental current spectrum but do not differ much in the flux spectrum. This lack of symmetry also increases the amplitude of some low-order $2n$ harmonics, especially in the flux spectrum.

In addition to the differences in harmonic amplitudes, another notable observation is the presence of sidebands around the fundamental frequency, at 25 Hz and 75 Hz, with significant amplitudes. These sidebands are attributed to eccentricity in the motor (see 2.6.3 Mechanical Failures for more information) and follow the formula below for permanent magnet machines [79]:

$$f_{ecc} = f_S \pm \frac{f_S}{p} \tag{3.3}$$

Lastly, it is worth noting that minor discrepancies in the stray flux harmonic amplitudes are observed. These discrepancies are primarily attributed to differences in the geometry of the flux sensors between the simulation and the experiment, as well as the aforementioned motor's inherent asymmetries.

The comparative amplitudes of the most significant harmonics in the stator current and stray flux spectra are presented in Table 3.3.

	Stator Current		Stray Flux	
Harmonic (Hz)	**FEA Model**	**Experiment**	**FEA Model**	**Experiment**
25	-111.27 dB	-39.27 dB	-53.50 dB	-29.57 dB
75	-108.11 dB	-41.12 dB	-51.80 dB	-41.99 dB
150	-80.02 dB	-40.46	-49.97 dB	-10.60 dB
850	-27.00 dB	-32.01 dB	-31.30 dB	-24.67 dB
950	-36.37 dB	-40.52 dB	-28.57 dB	-29.43 dB
1050	-71.35 dB	-20.11 dB	-26.88 dB	-17.05 dB
1150	-28.99 dB	-32.11 dB	-34.86 dB	-28.65 dB

Table 3.3: Comparison between simulated and experimental harmonic amplitudes in stator current and stray flux.

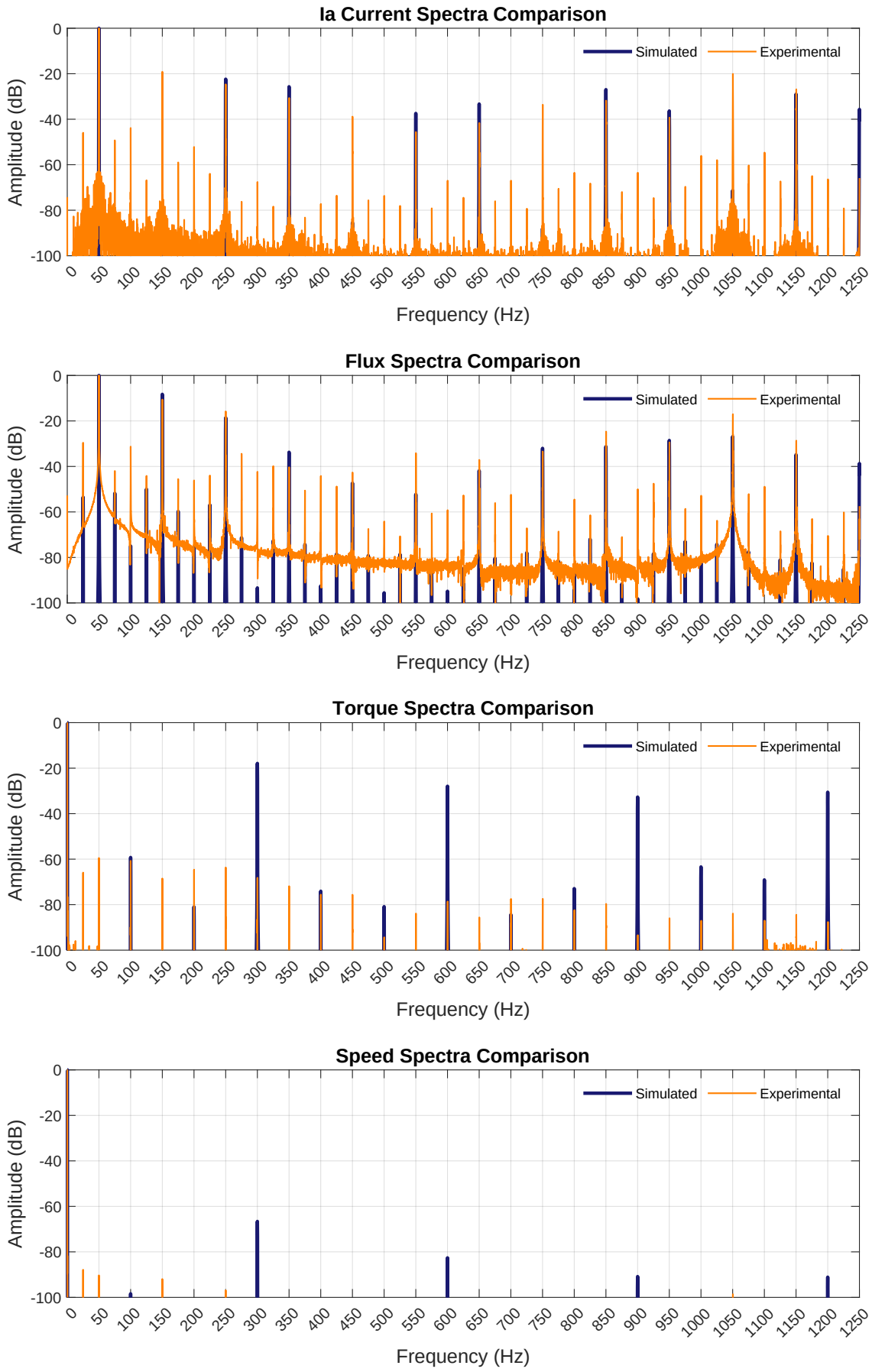

Figure 3.26: FFT of experimental stator current and stray flux.

Experimental Setup

The experiment for the data aquision of the real-life LSPMSM was done by Pr. Moríñigo Sotelo and Dr. Garcia-Calva at the University of Valldolid, in Spain.

The experimental setup comprises a Hybrid PMSM 750 W by WEG connected in a star configuration and powered by the grid. A magnetic-powder brake from Lucas-Nülle (SE 2662-5R), with its associated control unit (SO3213-7S), is used as the motor load and provides for measuring the torque and speed signals. The collection system involves a homemade board with voltage Hall effect transducers by LEM (LV25-P) and current clamps by YHDC (SCT013-005). The data acquisition (DAQ) board is from National Instruments (NI USB-6210).

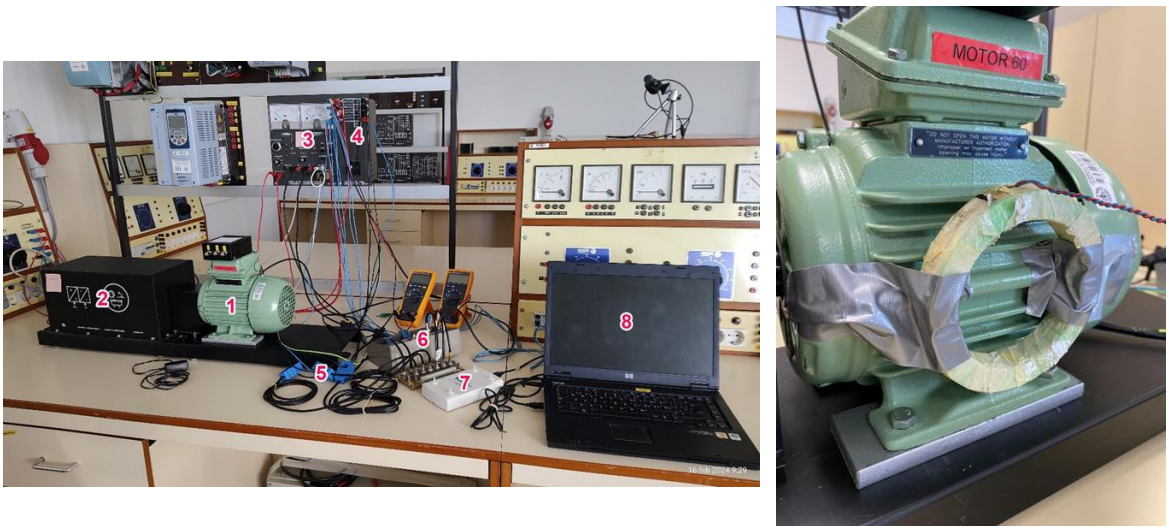

Figure 3.27: Experimental setup for LSPMSM measurements.

Chapter 4

Simulation Results Discussion

4.1 Demagnetization

This thesis examines the behavior of this motor under non-uniform demagnetization of a single permanent magnet. In Fig. 4.1 (a) is shown the magnet that was selected to be demagnetized. The choice of the magnet is irrelevant due to symmetry. In particular, five levels of fault severity were simulated: low (5%), moderate (10%, 15%) and high (20%, 30%). The demagnetized magnet was modeled in Simcenter MAGNET by creating a new magnet material for each severity level, and this equation then calculated its magnetic permeability:

$$B_a = (1 - a) \cdot B_0 \tag{4.1}$$

where **a**: % severity level and $\mathbf{B_0}$: the magnetic permeability of the healthy magnet. Fig. 4.1 (a) shows the demagnetization curves of the material for each case.

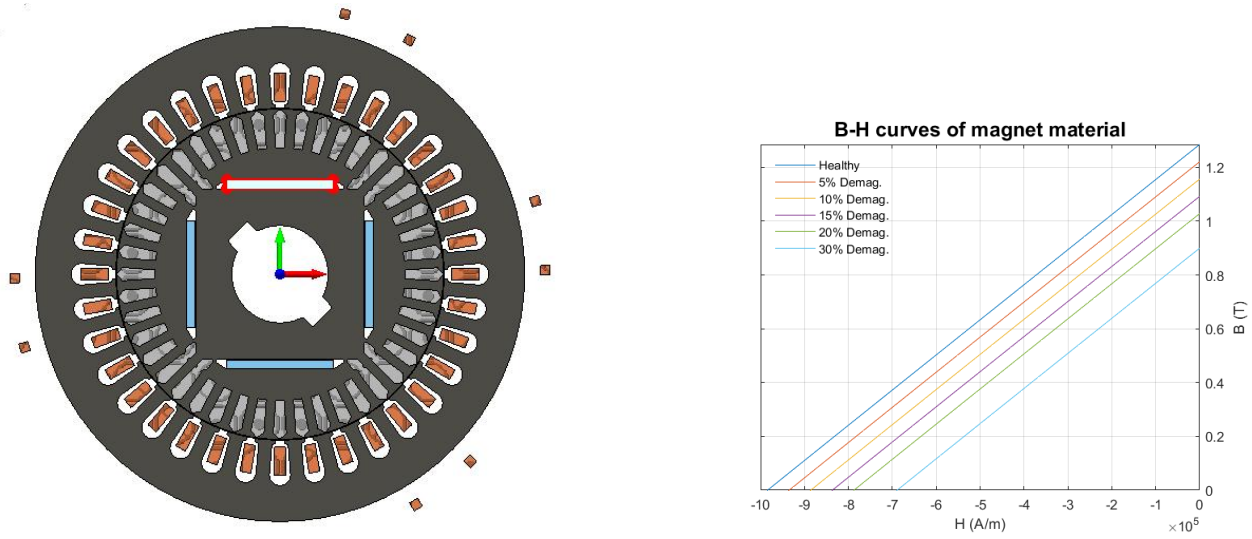

(a) (b)

Figure 4.1: (a) Positon of affected magnet, and (b) Demagnetization curves of magnet.

Steady-state performance data analysis

Performance data for each severity of the fault are compared with those of the healthy motor in Table 4.1. There was no problem with rotor synchronization or torque production in any of the cases.

It is observed that while magnet strength decreases, RMS current gradually increases while Power Factor (PF) and motor efficiency drop slightly and steadily, as demonstrated in Figure 4.2 (a) and (b). Since the weakened magnet reduces the magnetic field strength, the motor compensates by drawing more current to maintain the nominal torque. Higher current leads to higher electrical power, lowering efficiency, and PF. So, the results of Table 4.1 are within expectations.

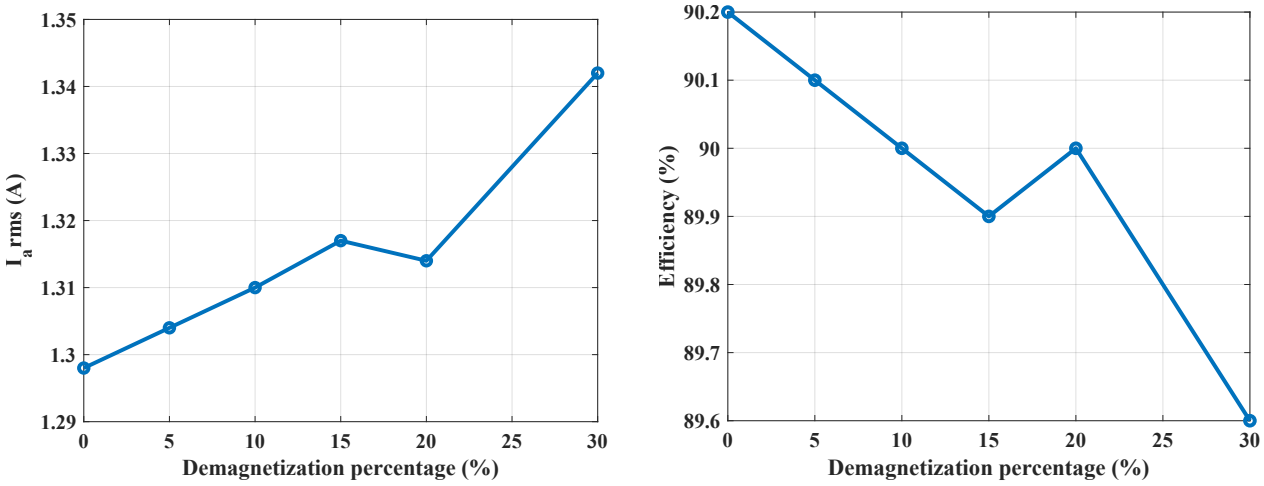

(a) (b)

Figure 4.2: RMS stator current and motor efficiency as a function of demagnetization level.

	Healthy	**5% Dmg**	**10% Dmg**	**15% Dmg**	**20% Dmg**	**30% Dmg**
$\mathbf{I_{a,rms}(A)}$	1.298	1.304	1.310	1.317	1.314	1.342
$\mathbf{P_m(W)}$	750.84	750.84	750.84	750.84	750.84	750.84
$\mathbf{P_{el}(W)}$	832.29	833.07	833.91	834.91	834.44	838.29
$\mathbf{T(Nm)}$	4.78	4.78	4.78	4.78	4.78	4.78
$\mathbf{n_s(rpm)}$	1500	1500	1500	1500	1500	1500
$\boldsymbol{\cos\phi}$	0.925	0.922	0.919	0.915	0.917	0.902
$\boldsymbol{eff}$	0.902	0.901	0.900	0.899	0.900	0.896

Table 4.1: Steady-state motor performance data.

Following, Figure 4.4 shows the time signals of the motor's torque and speed during start-up until synchronization occurs. The first critical observation is that as the demagnetization percentage increases, the time until synchronization generally decreases. This is explained by the fact that the rotor's overall magnetic field produced by the permanent magnets decreases; therefore, the breaking torque decreases accordingly, which eases the synchronization process.

The torque-speed characteristic is shown in Figure 4.3. It differs from the theoretical characteristic due to the presence of oscillations and higher harmonics in the torque and speed.

The stator phase current and the stray flux of the motor for all five severity levels do not have significant changes compared to the respective healthy signals, as shown in Figure 4.5 (a) and (b). The lack of obvious differences is due to the fact that the demagnetization affects only one out of four neodymium PMs. The other three healthy permanent magnets are so strong that they manage to compensate for part of the lost magnetic field density. However, there is still an asymmetry inserted in the magnetic field, which in theory can be more clearly determined after implementing the FFT analysis in the next section.

The above explanation is validated by Figure 4.6, which shows an instance of the motor's air-gap flux density (cross section) at a simulated time of 6.9 s. The demagnetized magnet is colored red to pinpoint its location. Comparing the healthy case with the most severe case of 30% demagnetization, it is evident that the magnetic flux density above the weak magnet in the latter case is less saturated.

Furthermore, it is observed that the weak magnet's position in the cases 5%, 10% is different compared to the cases 15%, 20%, 30%. This is a result of the different times the motor takes to reach steady state. This difference can also be seen in Figure 4.6 (c), which shows the air gap flux density as a function of the rotor angle. There is an exception of behavior in the ranges $140^o - 180^o$ and $320^o - 360^o$, which is totally in agreement with the position of the demagnetized magnet of Figure 4.6. In the former, the magnetic flux density of the 5% and 10% demagnetization cases is above the healthy graph, while the 15%, 20% and 30% demagnetization cases are below it, and in the latter, the opposite is happening, even though they should have been in a consecutive order.

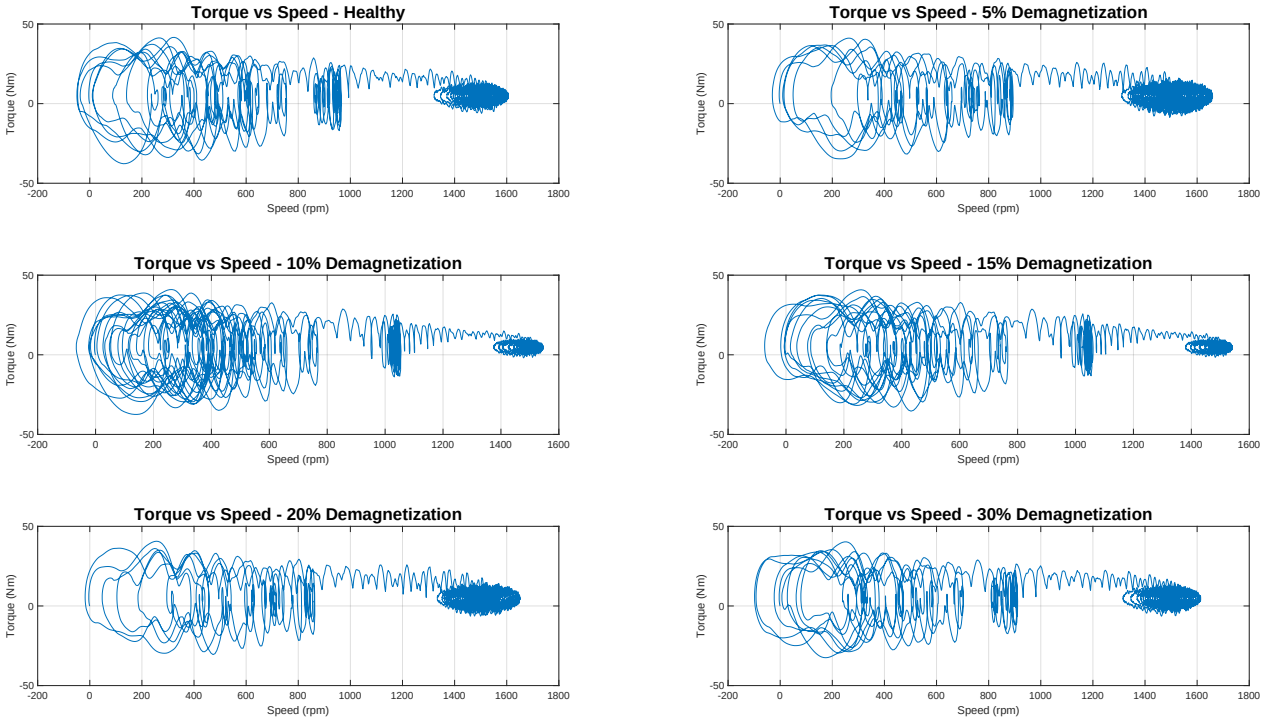

Figure 4.3: Torque-Speed characteristic for all demagnetization cases.

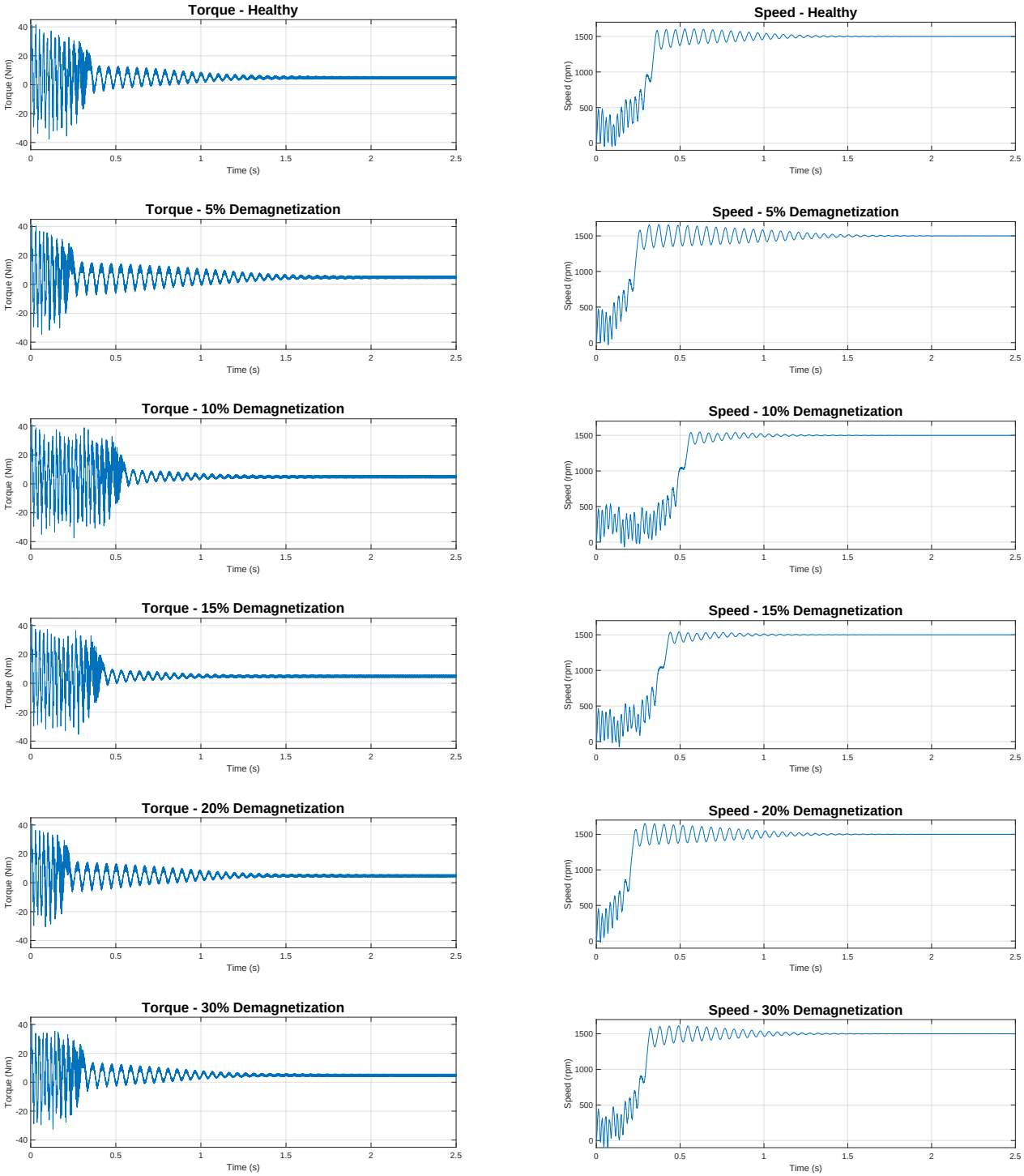

Figure 4.4: Transient torque and speed time signals for all demagnetization cases.

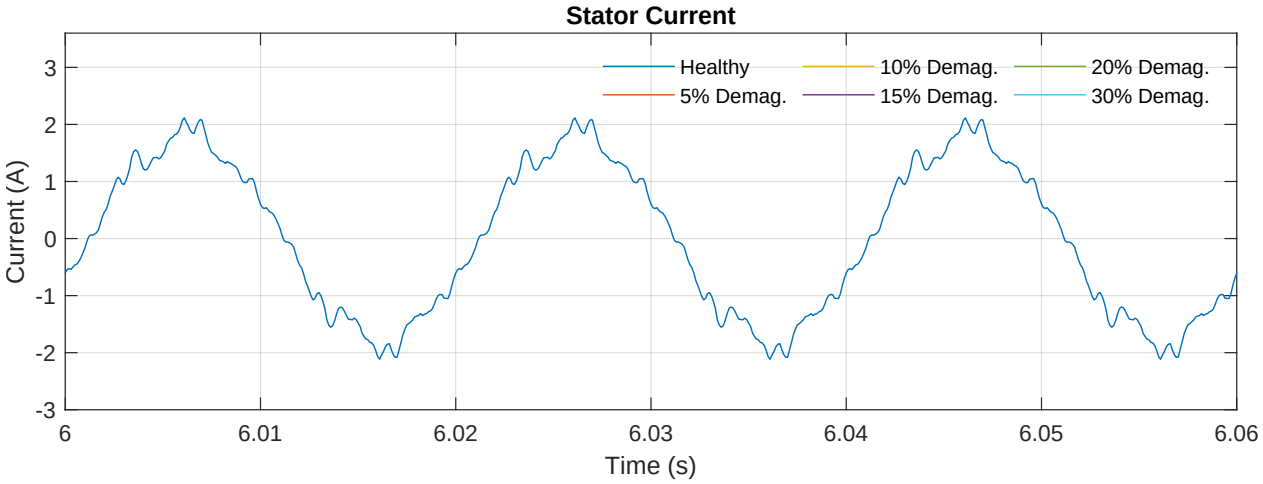

(a) Steady-state stator current.

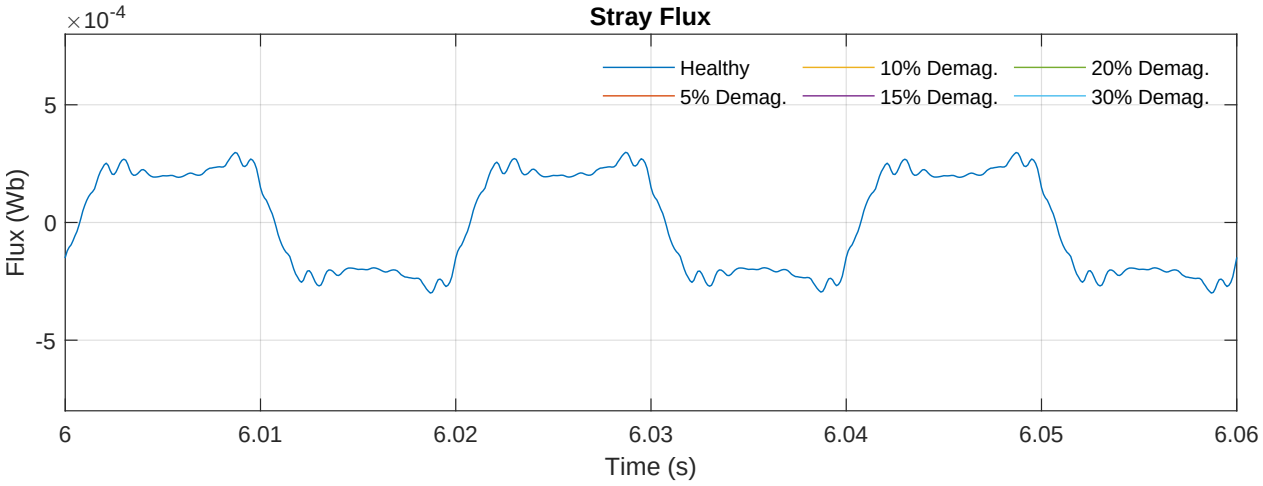

(b) Steady-state stray flux.

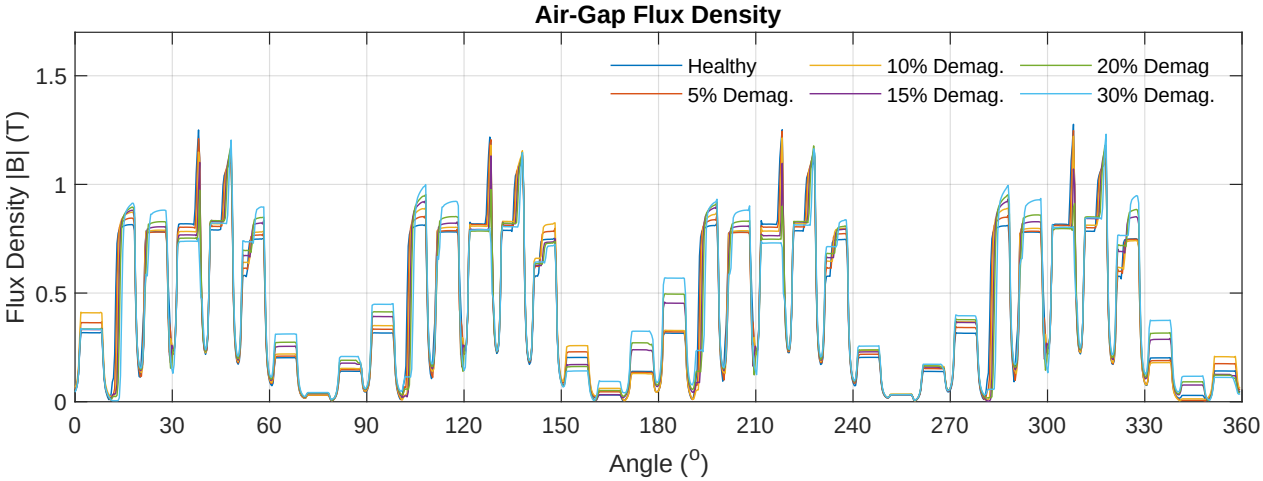

(c) Air gap flux density.

Figure 4.5: Motor's stator current, stray flux and air-gap flux density for each demagnetization level.

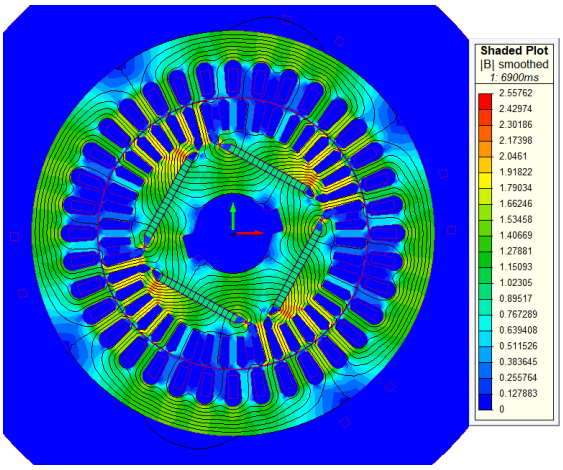

(a) Healthy

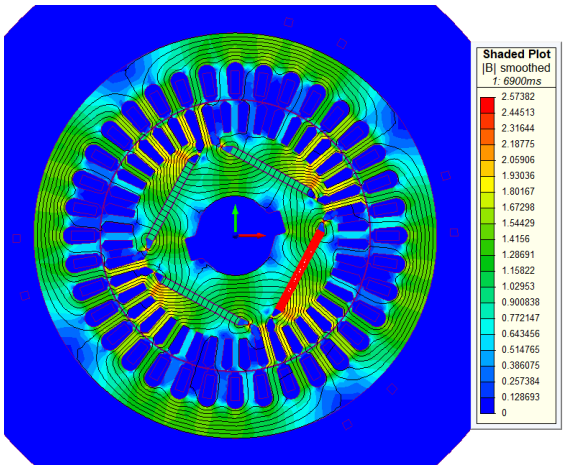

(b) 5% Demagnetization

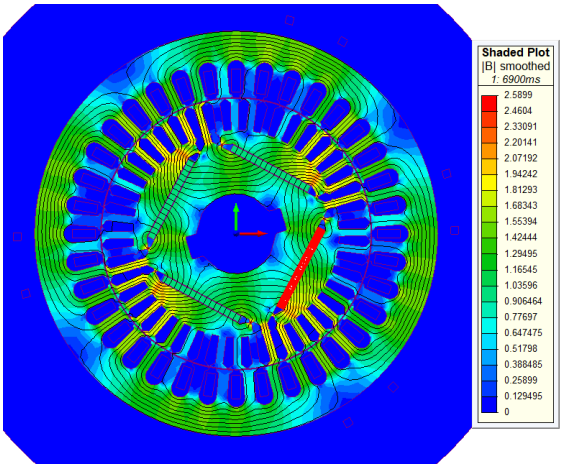

(c) 10% Demagnetization

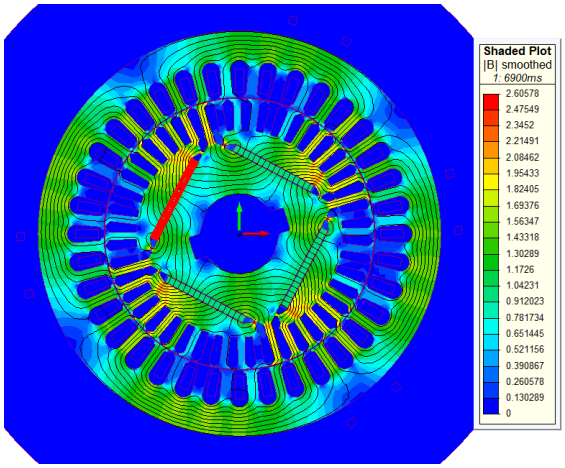

(d) 15% Demagnetization

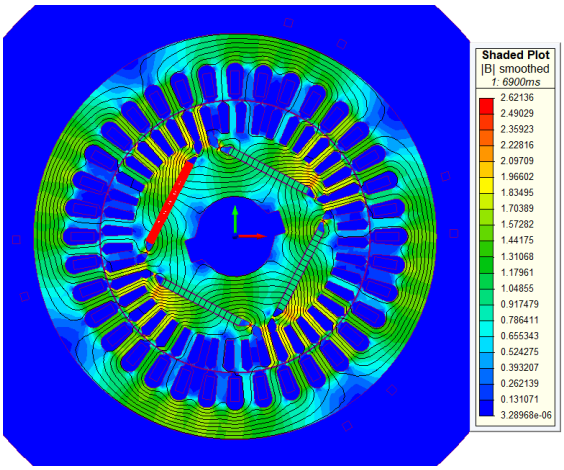

(e) 20% Demagnetization

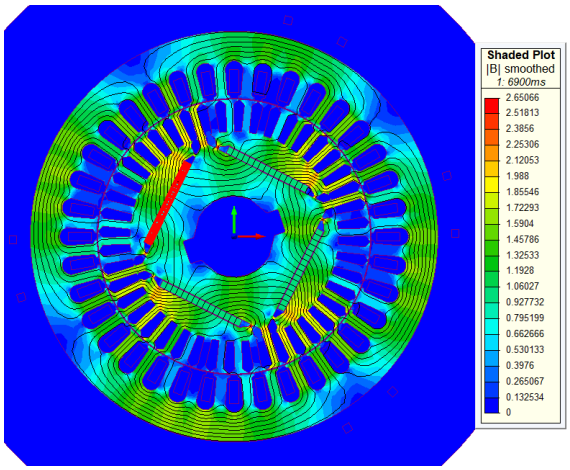

(f) 30% Demagnetization

Figure 4.6: Cross-section magnetic flux density of demagnetization fault cases in steady state (6900ms).

MCSA and Stray Flux Monitoring using FFT

The Fast Fourier Transform analysis was applied for the motor's current and stray flux signals of Figure 4.5. The frequency content of those signals for each faulty case is compared with the healthy content in Figure 4.7 and Figure 4.8 respectively.

Upon analysis of the current spectrum of each case, there are two obvious observations. The first is that there is a very slight drop in the amplitude in the motor's main signatures that is proportional to the severity of the demagnetization. This is ascribed to the fact that those harmonics are a manifestation of the saturation of the stator's and rotor's ferromagnetic core. As mentioned above, demagnetization causes less saturation around the area of the affected magnet. Therefore, as saturation decreases, the amplitude of those harmonics also decreases. Nevertheless, the change in amplitude is so small that it is not enough to derive the motor's health. It is suspected that upon combined and varied demagnetization of all four magnets this decrease in amplitude in the stator current would become more clear.

Secondly, there is an increase in the amplitude of the side harmonics, also proportional to the severity level. This is in accordance with the literature, which suggests monitoring the fault at frequencies $f_s \pm k\frac{f_s}{p}$ in the stator current. However, this increase is insignificantly small because of the inductances present in the motor's circuit, acting like a filter. This filter is more efficient at cutting high rather than low frequencies and that is why the effect can be seen mostly around the fundamental and the third harmonic.

On the other hand, all the expected side harmonics of the stator current are clearly and strongly present in the stray flux at amplitudes approximately 28dB (5% demagnetization) and 40dB (30% demagnetization) higher than those of the healthy condition. This is not unexpected, since the demagnetization of a magnet directly influences the magnetic flux of the motor. So flux monitoring is a valid method for the detection of the demagnetization of one magnet, even at low severity, for this motor but MCSA is not a reliable method.

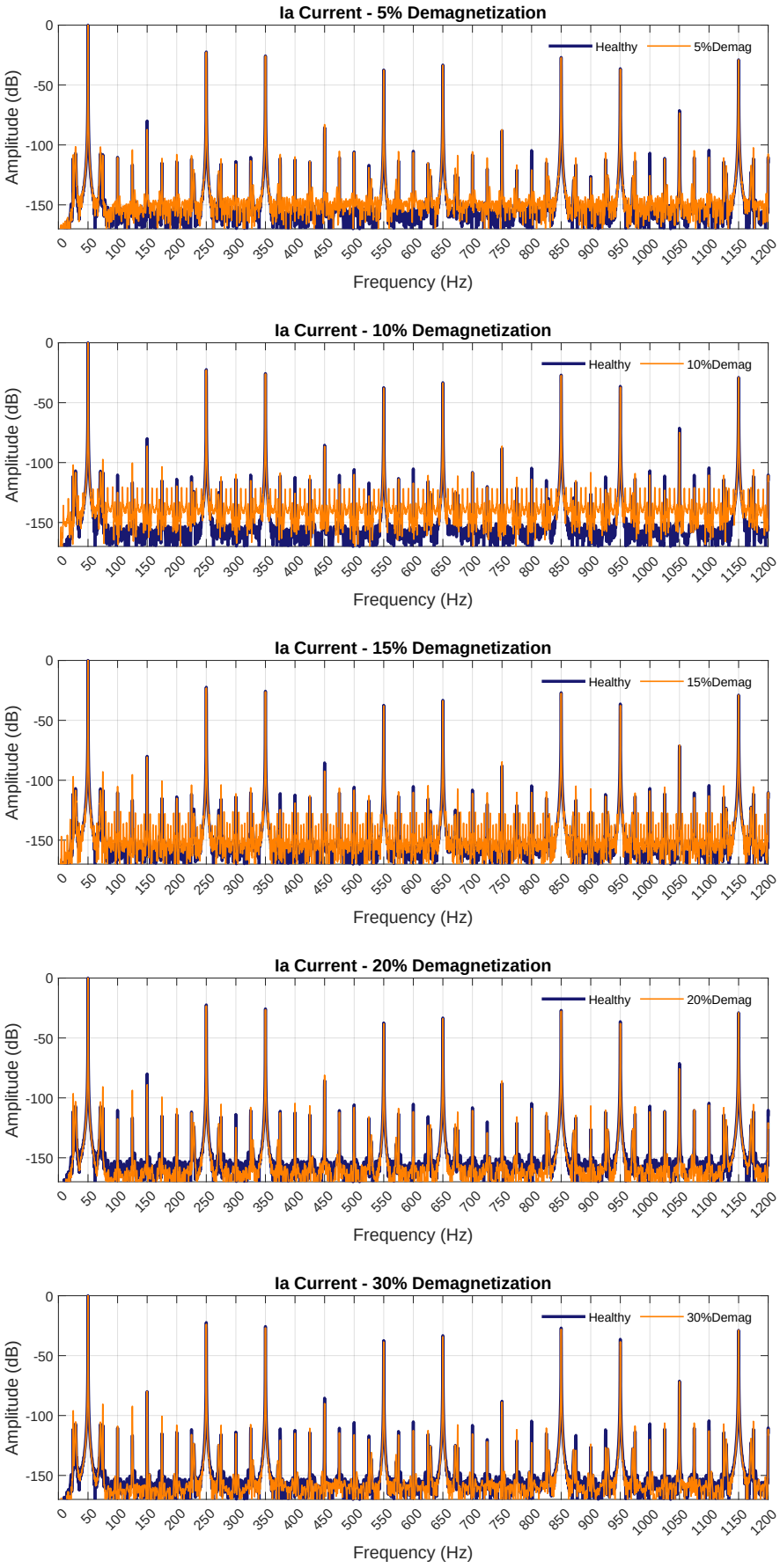

Figure 4.7: Comparative FFT spectra of healthy and faulty stator current signal for all demagnetization cases.

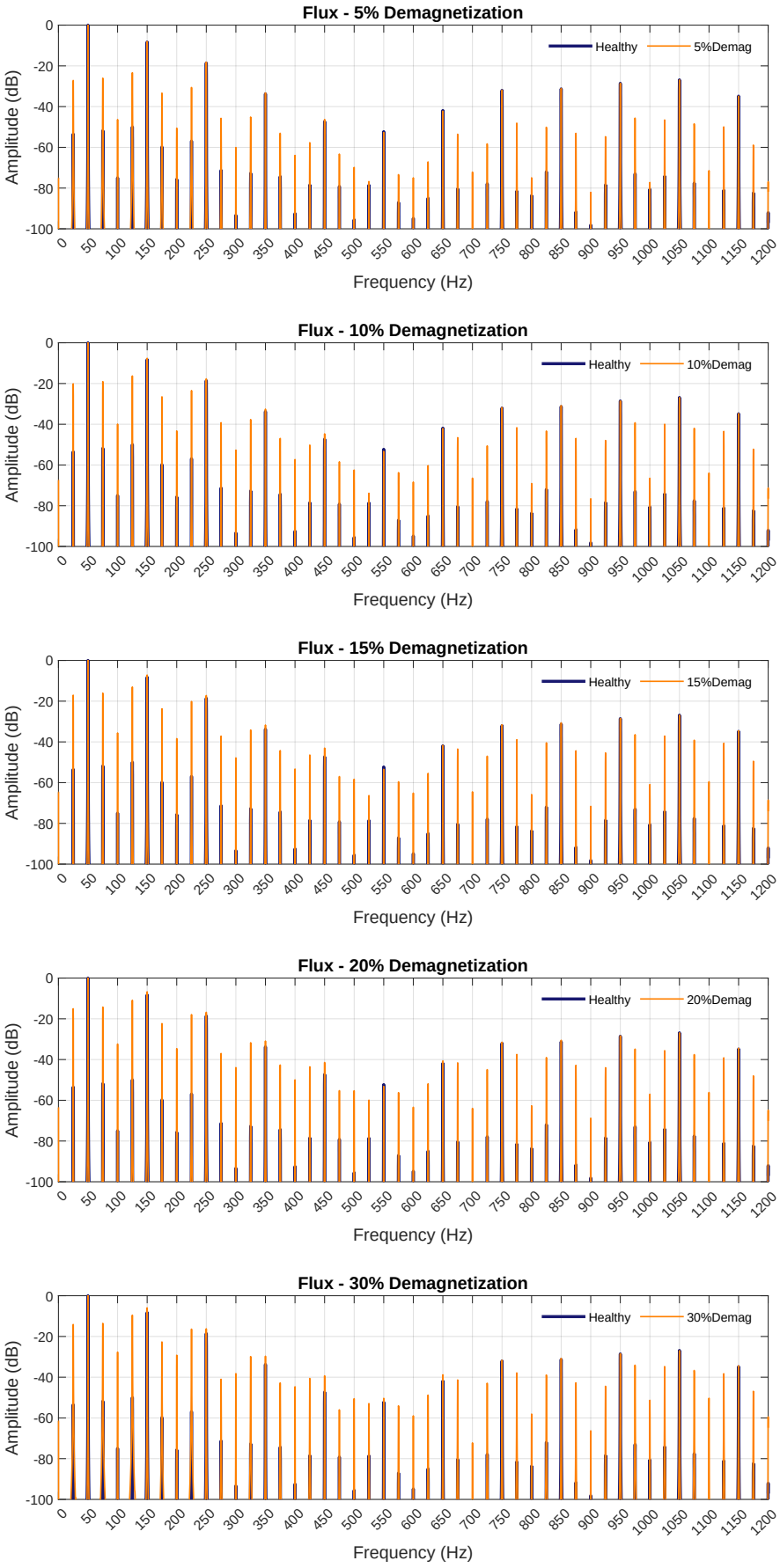

Figure 4.8: Comparative FFT spectra of healthy and faulty stray flux signal for all demagnetization cases.

4.2 Broken Bar

The broken bar fault was modeled in FEA by connecting one $1TOhm$ resistance in series with the chosen rotor bar (see Figure 4.9). That way, an open circuit is modeled. Seven cases of broken bars were studied out of which: two cases have one broken bar (BBS6, BBW10), two cases have two adjacent broken bars (BBS6S7, BBW10W11), two cases have two non-adjacent broken bars (BBS6S1, BBS6W10), and one case has three adjacent broken bars (BBS5S6S7). *BB* stands for broken bar, *S* stands for the simple rotor bar, and *W* stands for the deeper rotor bar, which also acts as a flux barrier. Figure 4.10 shows the position of all those rotor bars relative to one magnet. From right to left are the S1, S5, S6, S7, W10, W11 rotor bars.

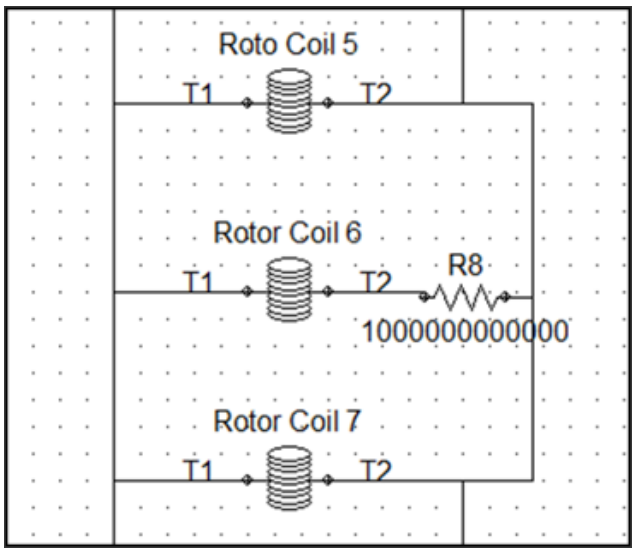

Figure 4.9: Broken rotor bar modeled by connecting a 1TOhm resistance in series.

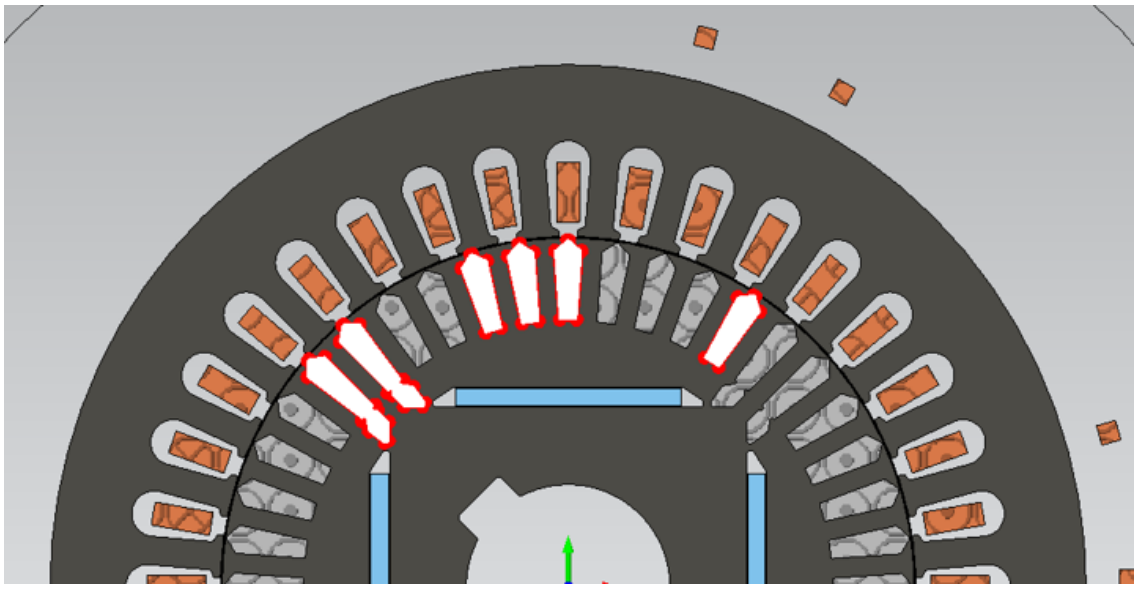

Figure 4.10: Positions of broken rotor bars. From right to left, their names are S1, S5, S6, S7, W10, and W11.

Steady-state analysis using FFT

In induction motors, when the rotor rotates at synchronous speed, the rotor current and torque is practically zero, as shown in the current-speed characteristic. The LSPMSM is no exception to this fact. This means that BB fault detection is not possible through a steady-state analysis. Still, steady-state analysis was performed to rule out any exceptions.

As expected, the motor performance data organized in Table 4.2 show no useful signs of any existing fault. Likewise, the MCSA method shown in Figure 4.18 cannot detect any of the simulated BB faults. There is a clear increase in the amplitude of high-frequency components in the stray flux spectra, especially for the worst-case scenario with three broken bars (BBS5S6S7). However, considering the real-life motor already has a higher-amplitude healthy stray flux profile, it is not certain whether this difference will be visible.

	Healthy	**BBs6**	**BBw10**	**BBs6s7**	**BBs6s1**	**BBs6w10**	**BBw10w11**	**BBs5s6s7**
$\mathbf{I_{a,rms}(A)}$	1.298	1.2982	1.2978	1.2981	1.2981	1.2978	1.2968	1.2972
$\mathbf{P_m(W)}$	750.84	750.83	750.84	750.84	750.84	750.84	750.84	750.84
$\mathbf{T(Nm)}$	4.78	4.78	4.78	4.78	4.78	4.78	4.78	4.78
$\mathbf{n_s(rpm)}$	1500	1500	1500	1500	1500	1500	1500	1500
$\boldsymbol{\cos\phi}$	0.925	0.92531	0.92557	0.92536	0.92535	0.92555	0.92611	0.92583
$\boldsymbol{\eta}$	0.902	0.90218	0.9022	0.9022	0.9022	0.90223	0.90238	0.90234

Table 4.2: Steady-state motor performance data for all BB cases.

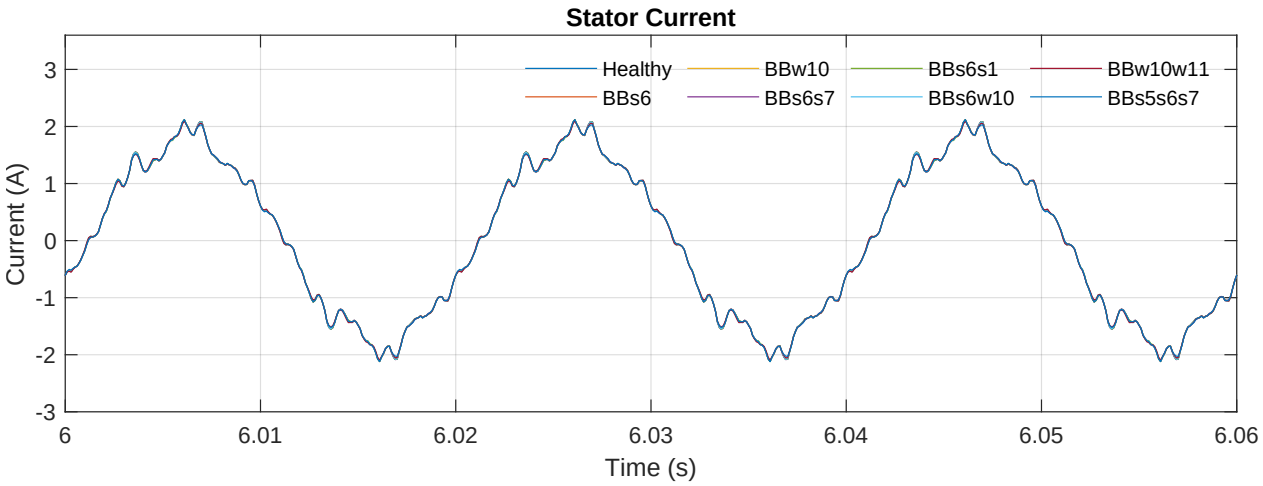

Figure 4.11: Comparative steady-state stator current time signals for all BB cases.

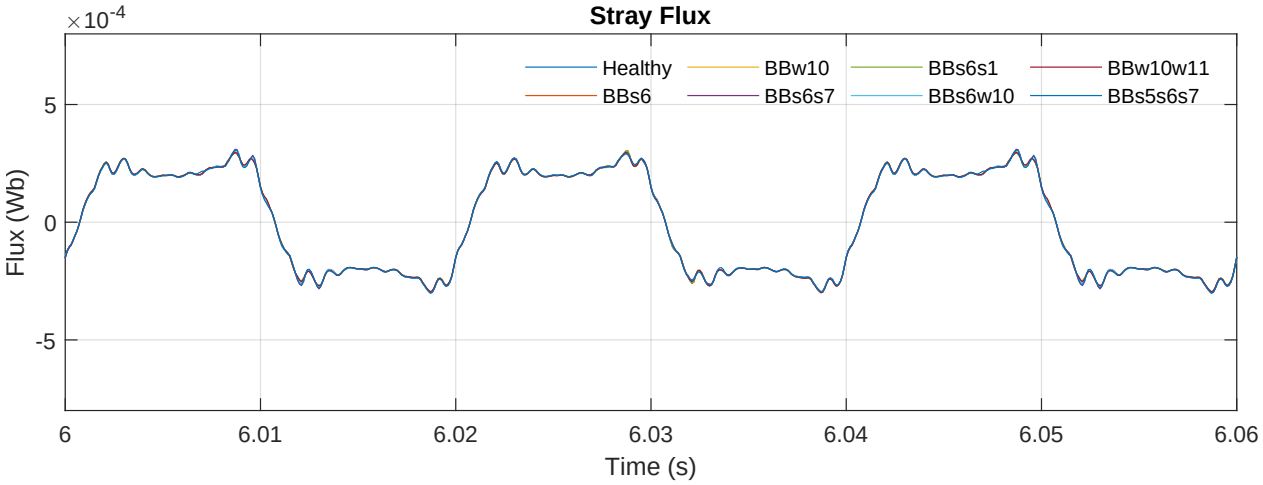

Figure 4.12: Comparative steady-state stray flux time signals for all BB cases.

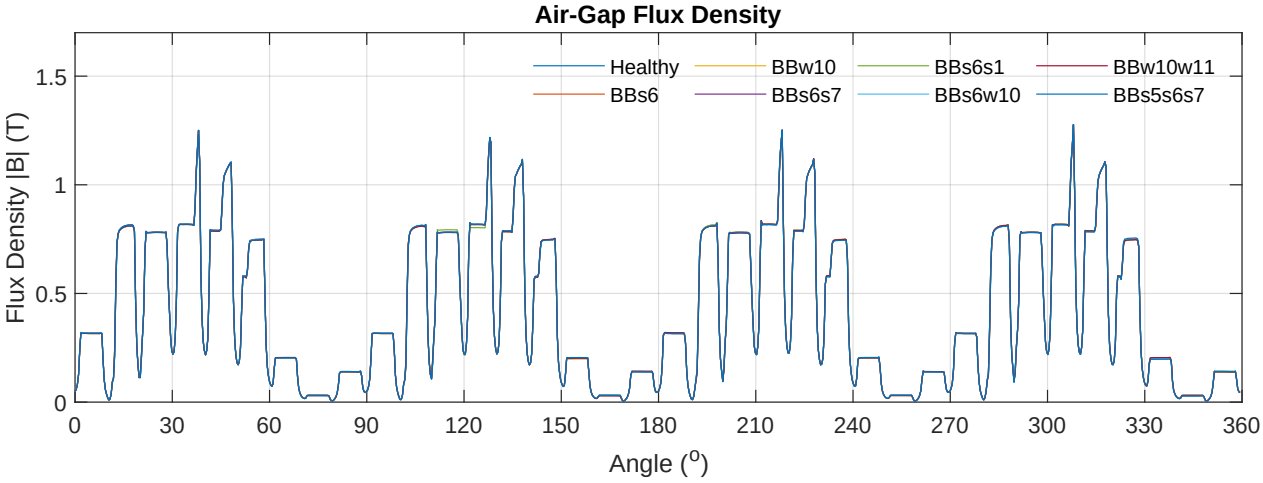

Figure 4.13: Comparative steady-state air-gap flux density of all BB cases.

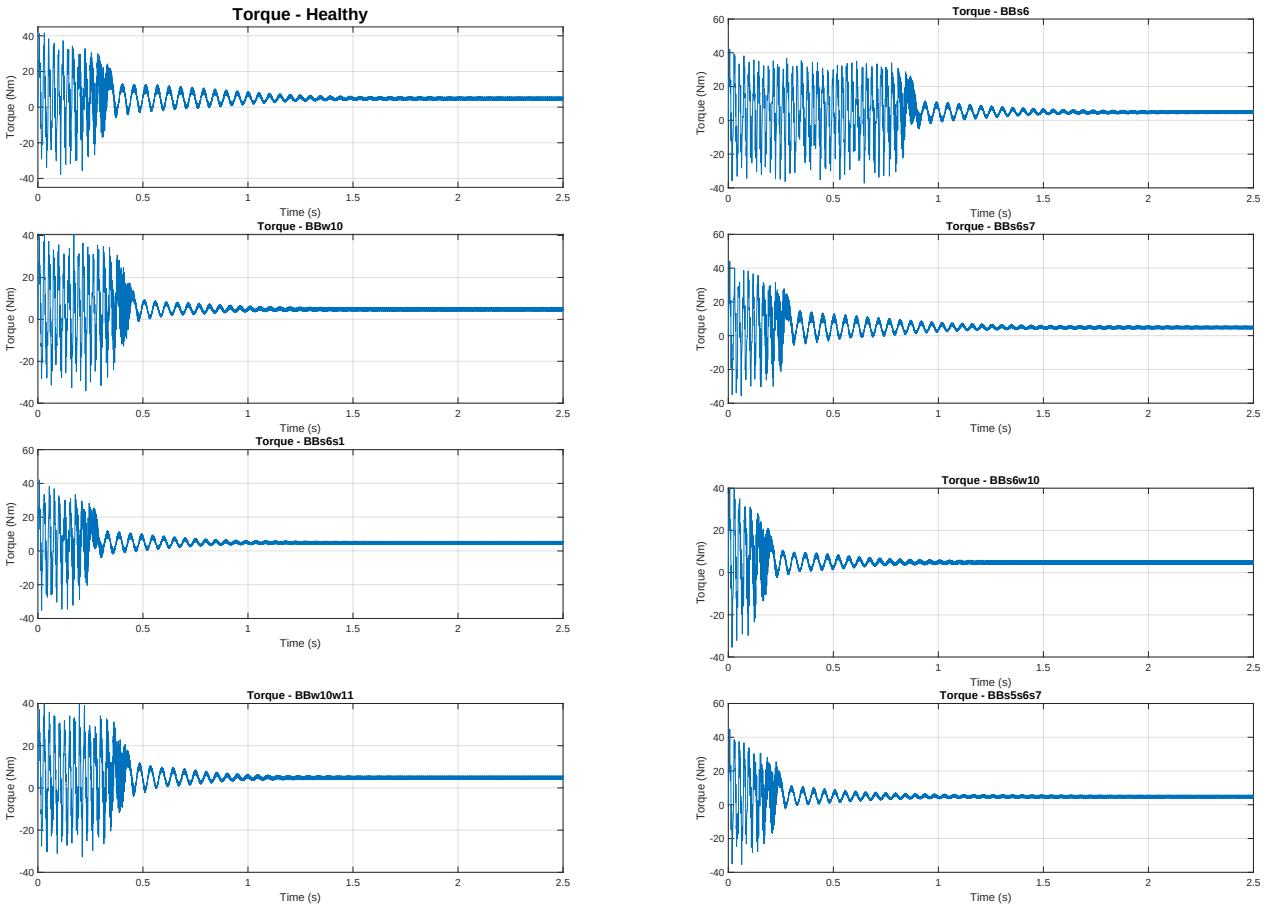

Figure 4.14: Transient torque time signal for all BB cases.

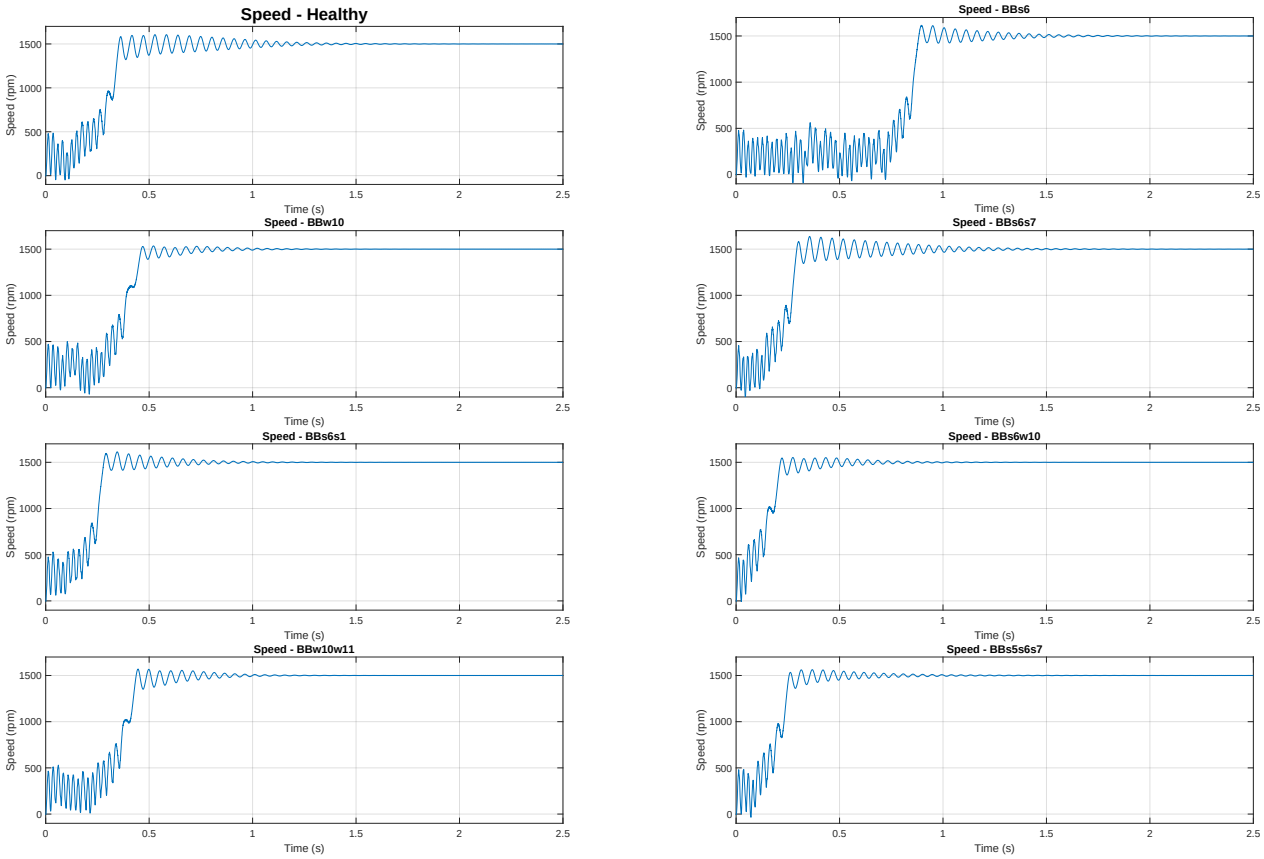

Figure 4.15: Transient speed time signal of all BB cases.

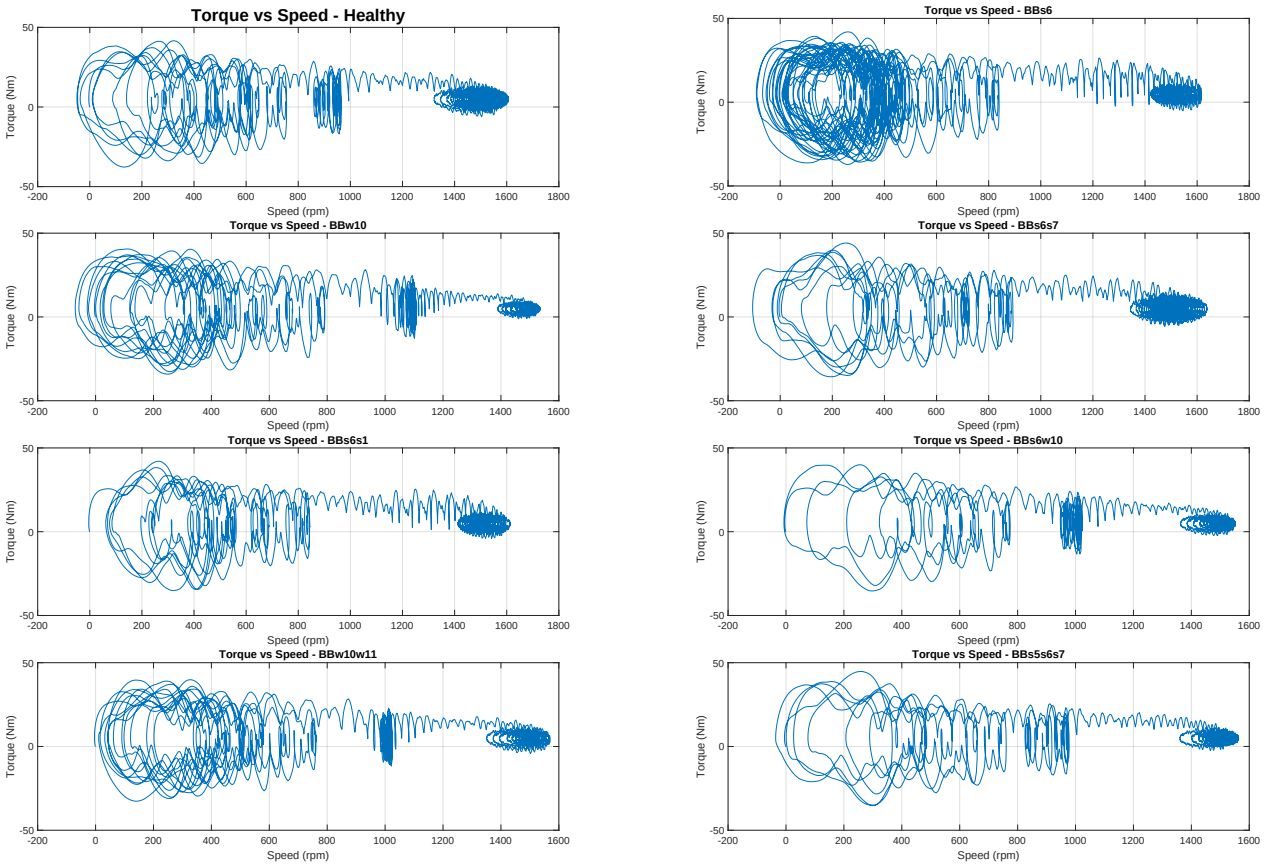

Figure 4.16: Torque-Speed characteristic for all BB cases.

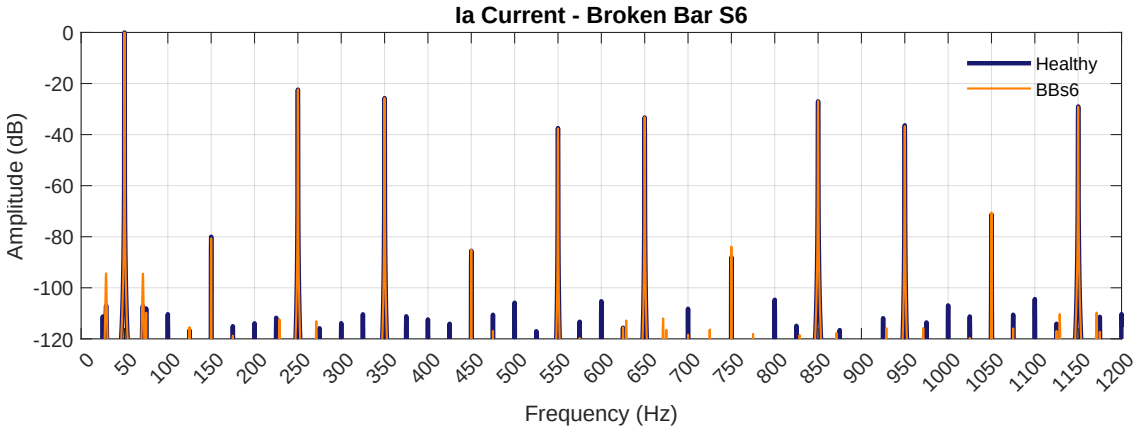
Ia Current - Broken Bar S6
Amplitude (dB)
Frequency (Hz)
Healthy
BBs6

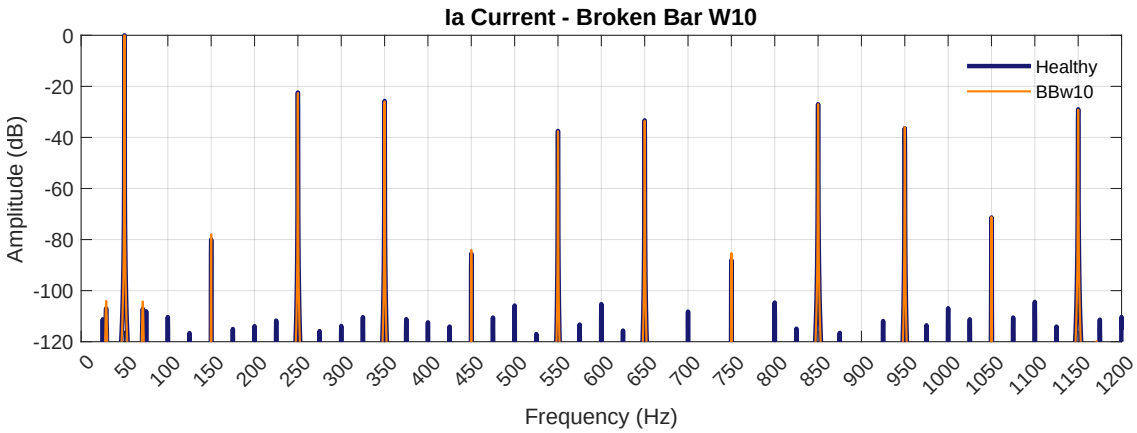
Ia Current - Broken Bar W10
Amplitude (dB)
Frequency (Hz)
Healthy
BBw10

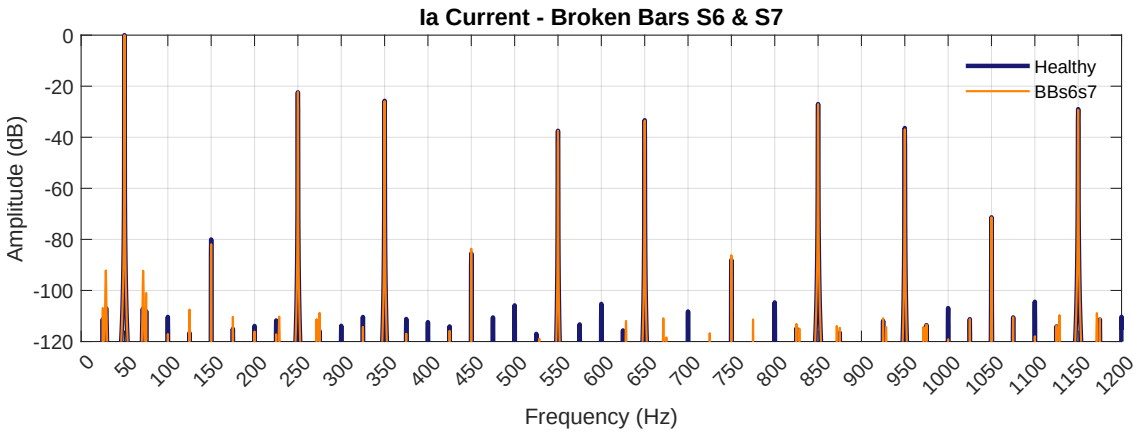
Ia Current - Broken Bars S6 & S7
Amplitude (dB)
Frequency (Hz)
Healthy
BBs6s7

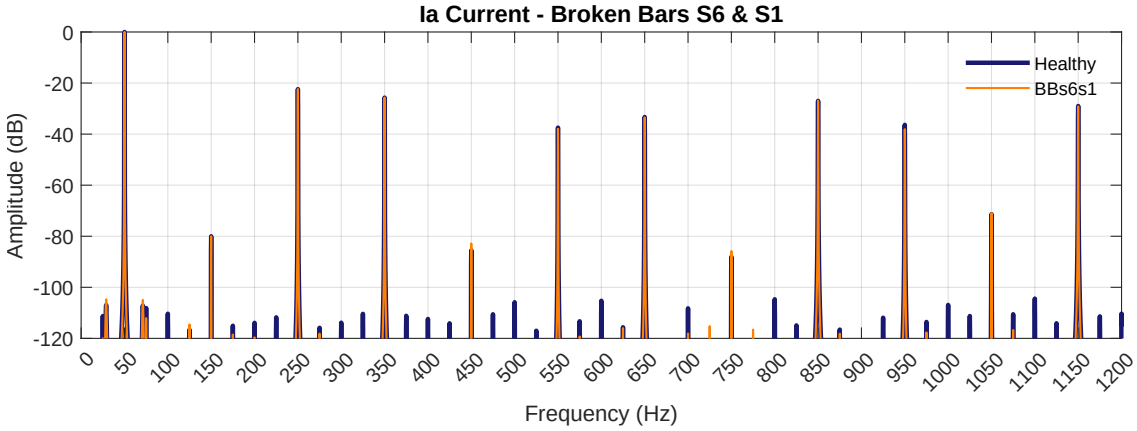
Ia Current - Broken Bars S6 & S1
Amplitude (dB)
Frequency (Hz)
Healthy
BBs6s1

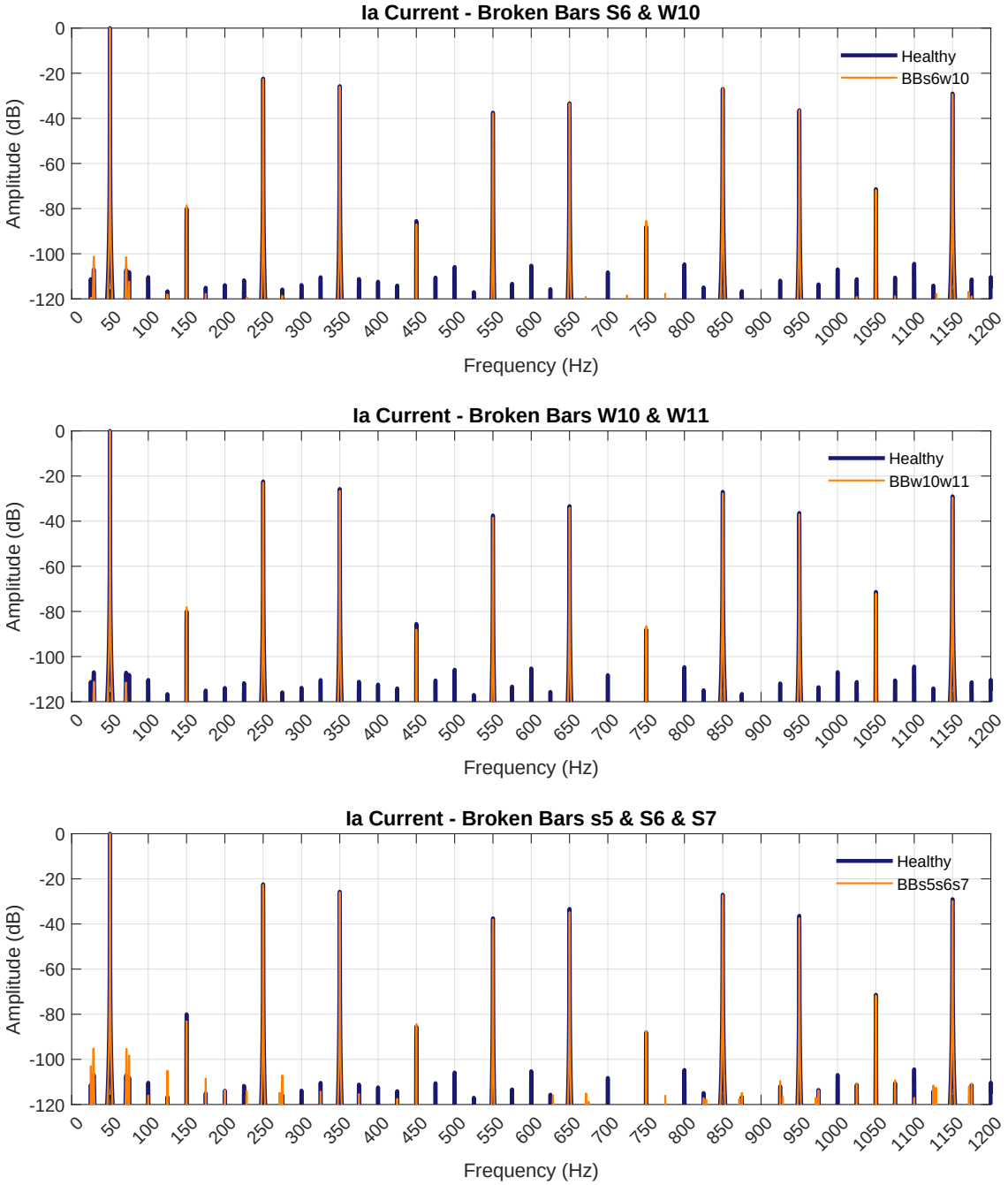

Figure 4.18: Comparative FFT spectra of healthy and faulty stator current signal for all BB cases.

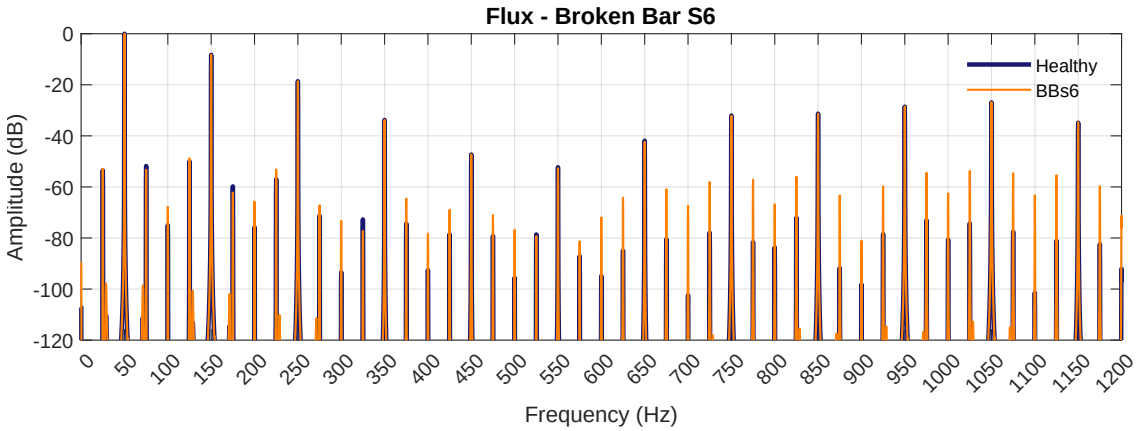
Flux - Broken Bar S6
Amplitude (dB)
Frequency (Hz)
Healthy
BBs6

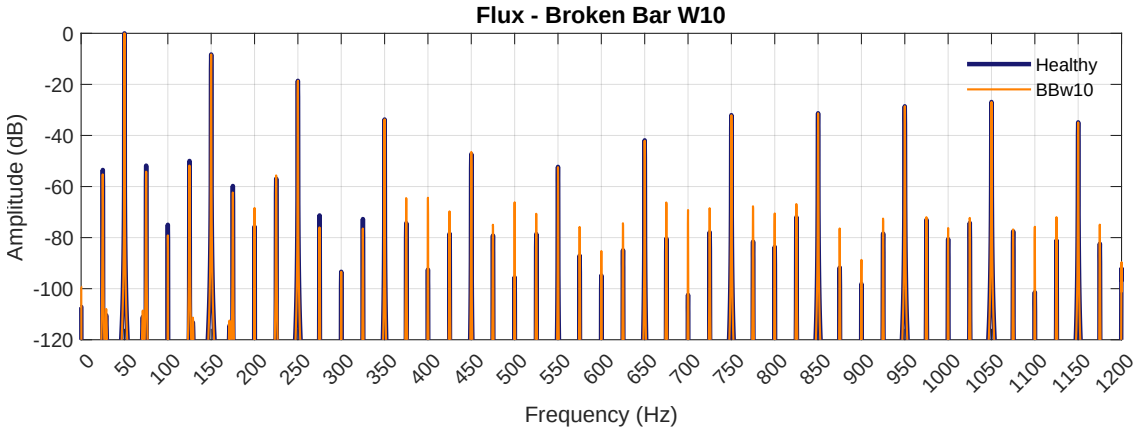
Flux - Broken Bar W10
Amplitude (dB)
Frequency (Hz)
Healthy
BBw10

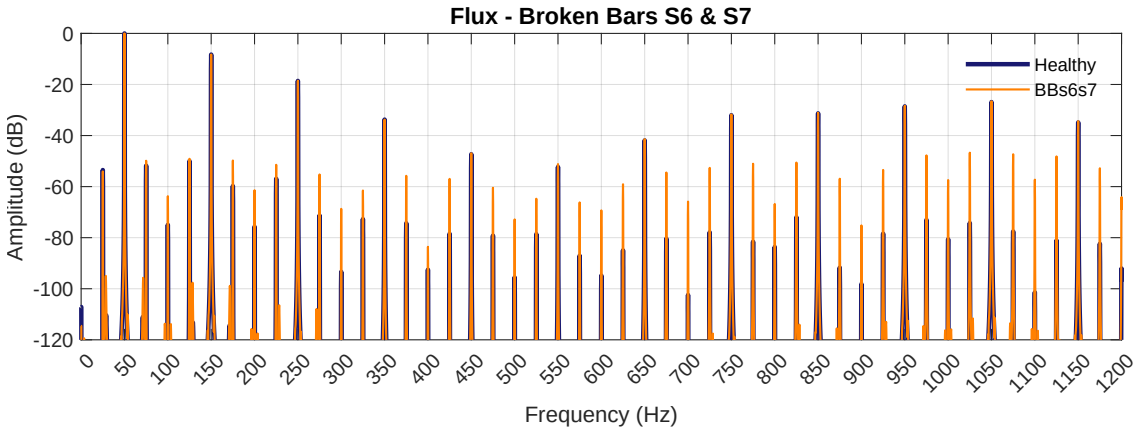
Flux - Broken Bars S6 & S7
Amplitude (dB)
Frequency (Hz)
Healthy
BBs6s7

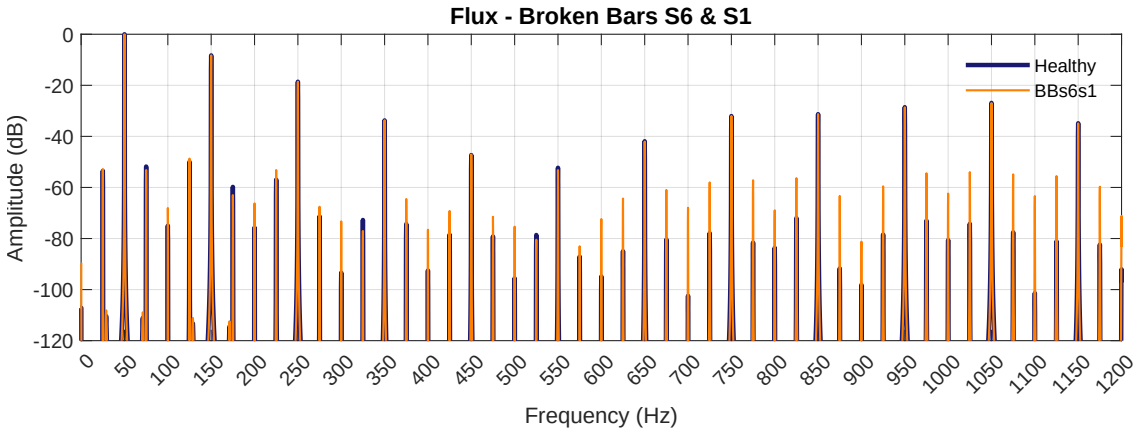
Flux - Broken Bars S6 & S1
Amplitude (dB)
Frequency (Hz)
Healthy
BBs6s1

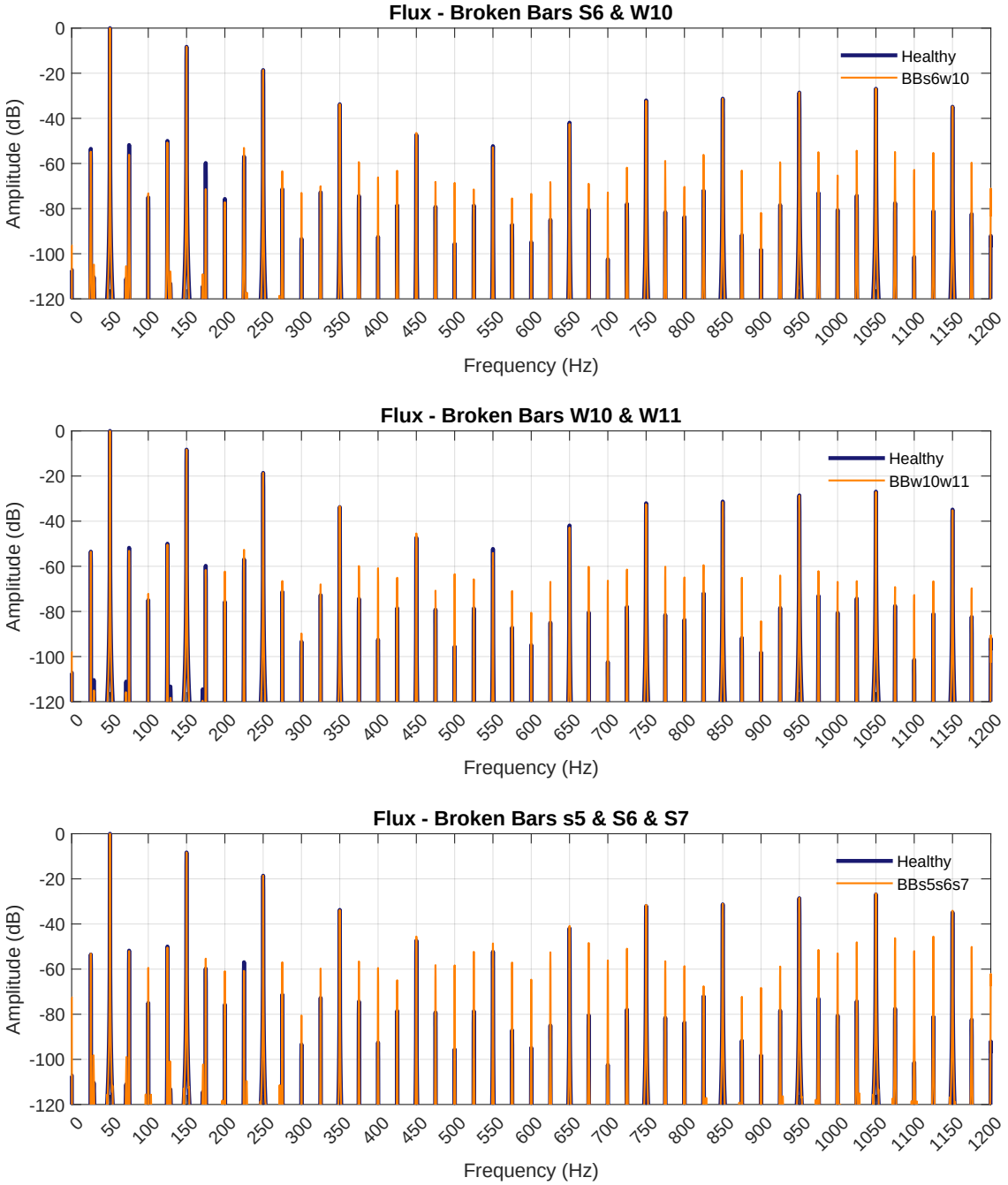

Figure 4.20: Comparative FFT spectra of healthy and faulty stray flux signal for all BB cases.

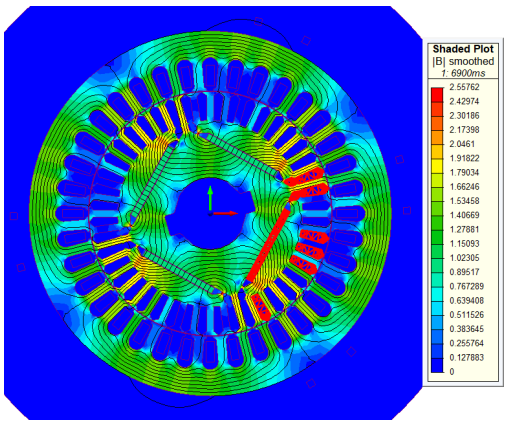

(a) Healthy

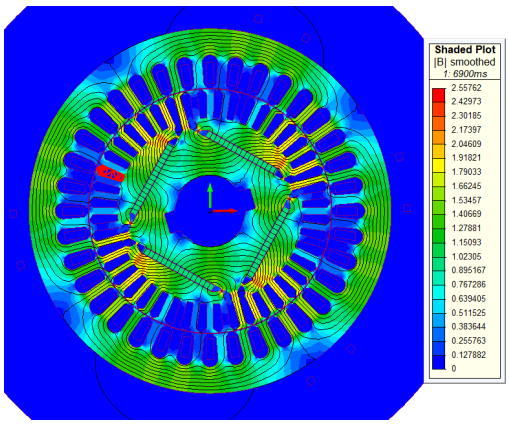

(b) BBs6

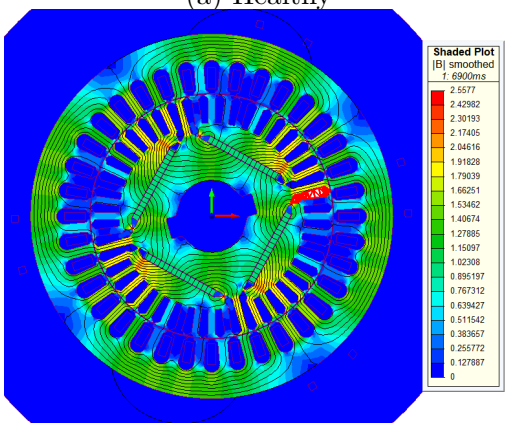

(c) BBw10

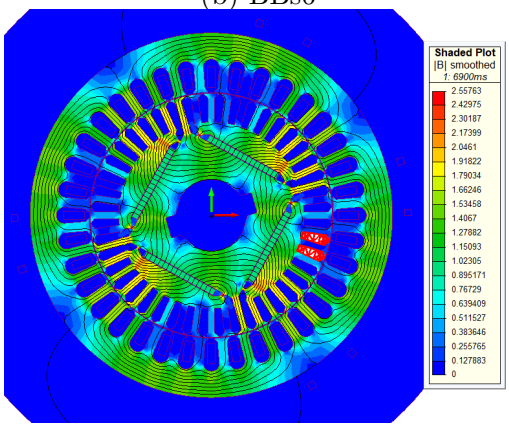

(d) BBs6s7

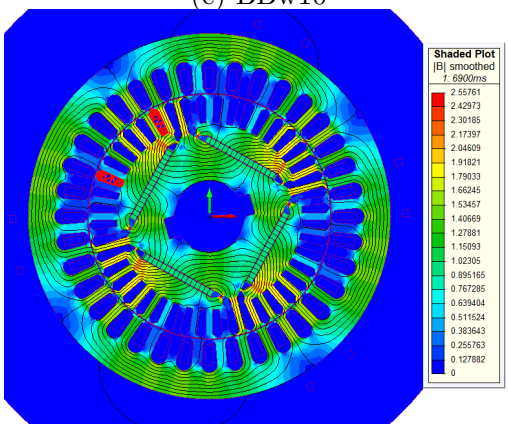

(e) BBs6s1

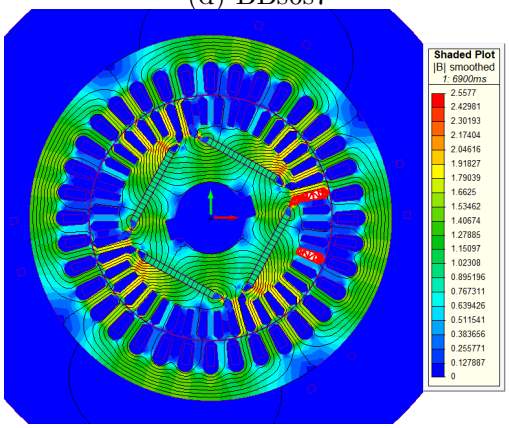

(f) BBs6w10

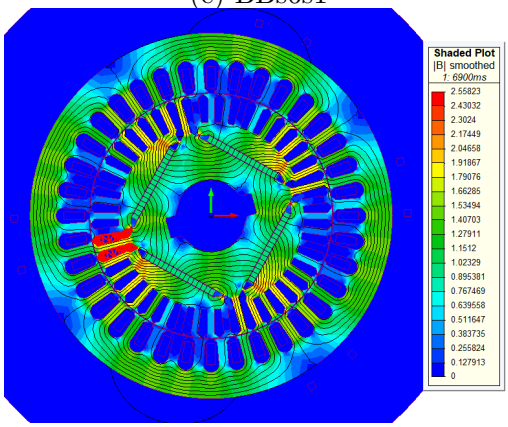

(g) BBw10w11

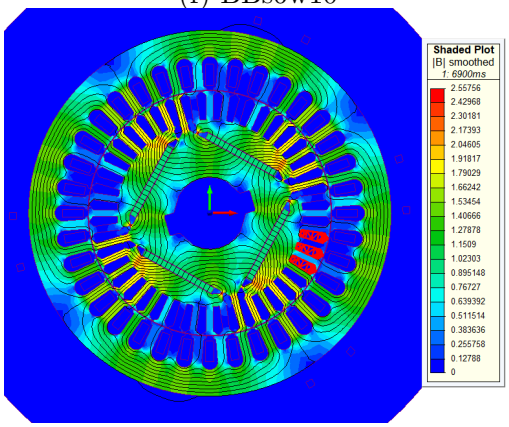

(h) BBs5s6s7

Figure 4.21: Illustration of motor's cross section magnetic flux density of broken bar fault cases in steady state.

Transient-state analysis using STFT

Since the squirrel cage has current only in the time period from the start of the motor to synchronization, called transient state. The *Short-time Fourier Transform (STFT)* is a more practical method compared to FFT in transient conditions [80]. The STFT spectograms of the stator current and the stray flux were obtained for each faulty case, and are displayed in Figure 4.22, and Figure 4.23 respectively.

The most widely spread methods for the detection of rotor damages are based on the analysis of motor currents and stray flux. Observing the current and stray flux spectrograms, it is evident that the well known broken bar fault-related sidebands located at $f_s - 2sf_s$ and $f_s + 2sf_s$ are not present. The former follows a characteristic V trajectory while the motor speed increases as it has been discussed in the corresponding theoretical section [81],[82]. There is a really strong signature starting from $0Hz$ and seems to reach $f_s = 50Hz$, which could overshadow the sidebands mentioned above. It is interesting that if one compares the trajectory of this harmonic to the transient speed signal of Figure 4.15 they are very similar. This points to the fact that it stems from the presence of the Permanent Magnets on the rotor, which start from stillness and reach synchronous speed.

What is clear is that compared to the healthy spectrogram, both faulty spectograms show many more trajectories in the areas of 0Hz-50Hz and 50Hz-250Hz resulting in high energy areas. The applied STFT however, has low resolution and those frequency components cannot be distinguished. Other signal processing methods in the Time-Frequency domain with better time-frequency resolution must be investigated for the broken bar fault.

Figure 4.22: Stator current STFT spectograms for all BB cases.

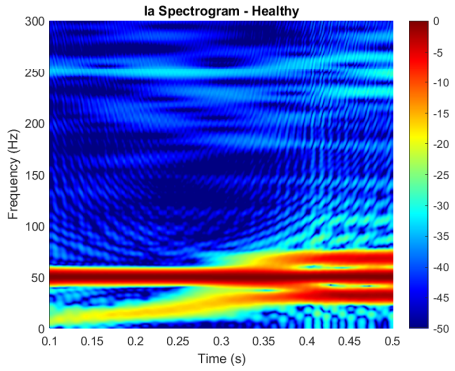

(a) Healthy

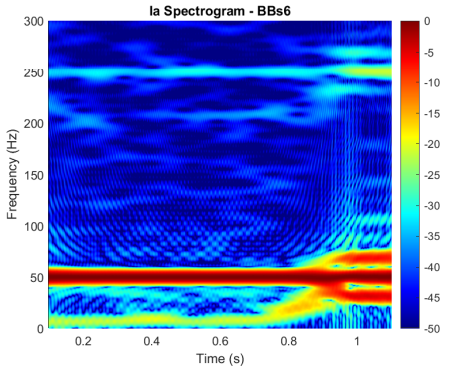

(b) BBs6

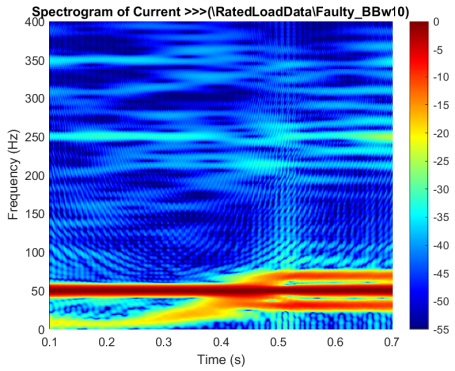

(c) BBw10

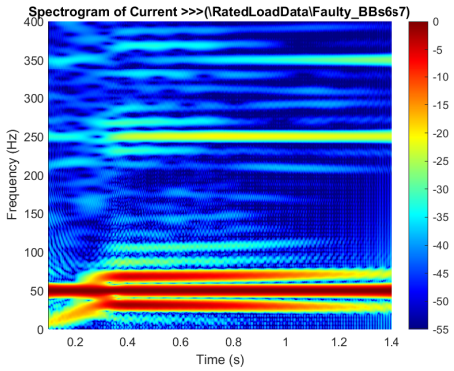

(d) BBs6s7

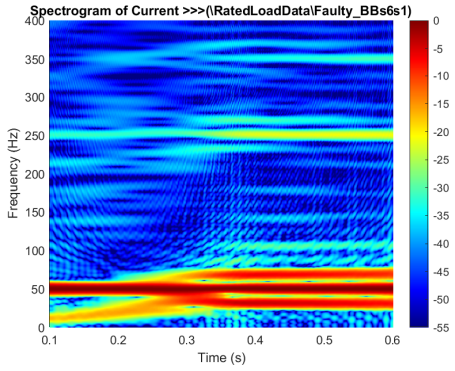

(e) BBs6s1

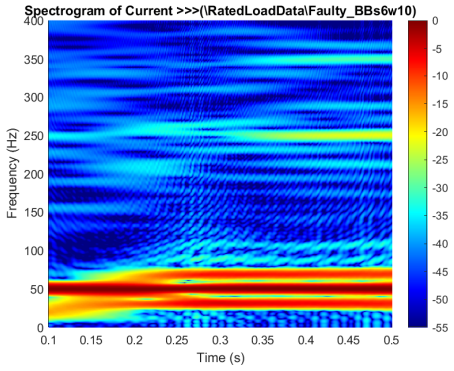

(f) BBs6w10

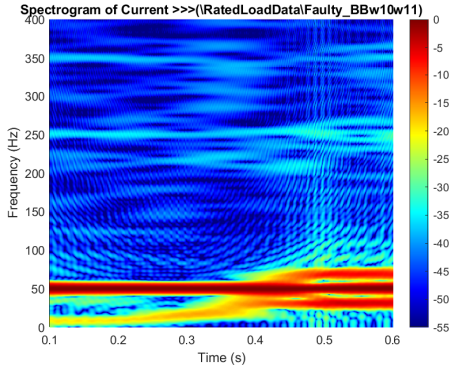

(g) BBw10w11

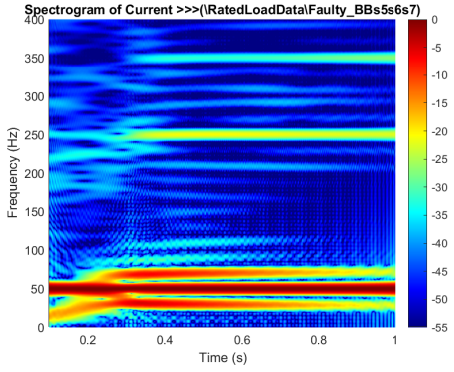

(h) BBs5s6s7

Figure 4.23: Stray flux STFT spectograms for all BB cases.

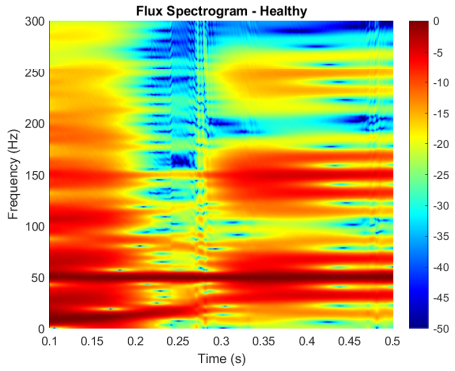

(a) Healthy

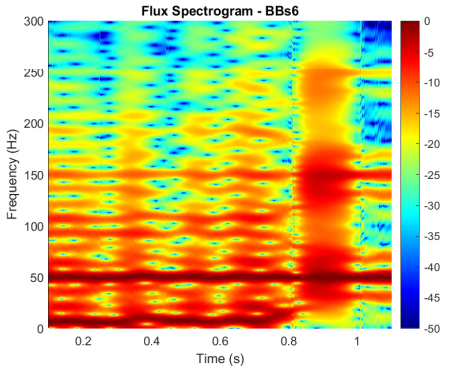

(b) BBs6

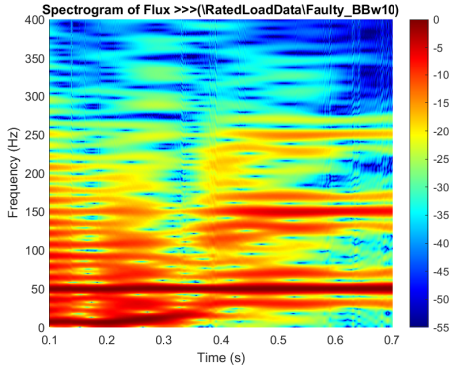

(c) BBw10

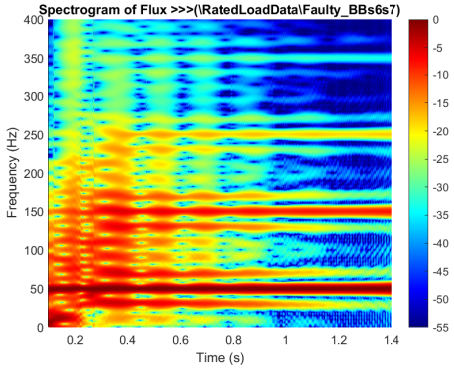

(d) BBs6s7

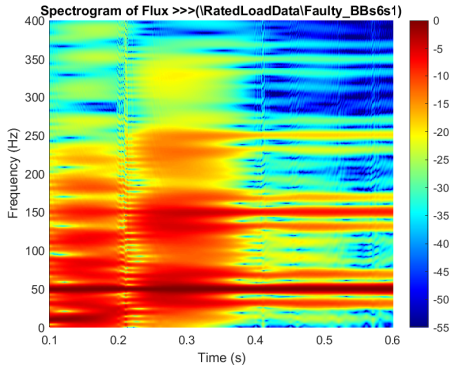

(e) BBs6s1

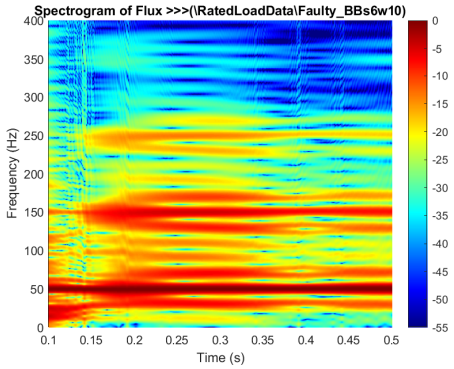

(f) BBs6w10

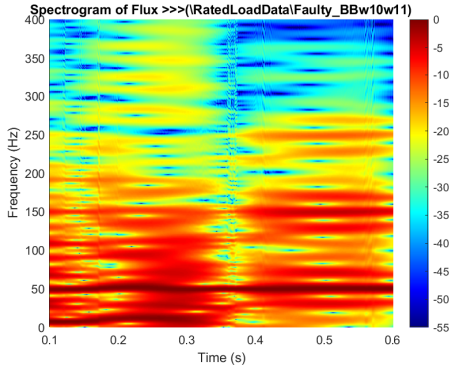

(g) BBw10w11

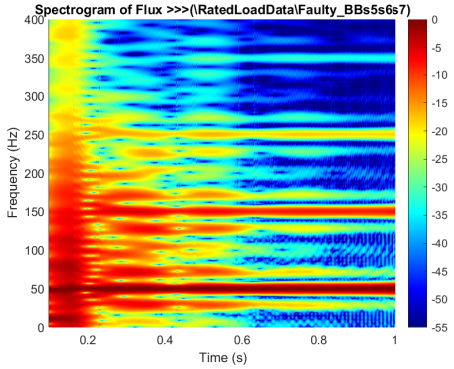

(h) BBs5s6s7

Chapter 5

Conclusion

Starting with the case of the uniform demagnetization of one magnet, it was determined that the MCSA failed to diagnose the fault, despite the fact that the literature suggests monitoring the fault at $f_s \pm k\frac{f_s}{p}$ in the stator current spectrum. It was interesting to see that all the above signatures strongly appeared in the stray flux spectrum, with very high amplitudes even from the a fault severity of 5% demagnetization. All faulty harmonics had a difference of at least 40dB when compared the healthy spectrum. Thus monitoring the stray flux of the LSPMSM can be a promising demangetization fault diagnostic method for this type of motor.

The MCSA method also did not yield anything for neither of the broken bar cases, which was expected due to the nature of the LSPMSM. On the other hand, an interesting increase in amplitude of some frequncies in the stray flux spectrum. It seemed that to be dependent on the fault severity, since the one broken bar cases had the lowest increase, while the three broken bar case had the highest increase compared to the healthy spectrum. Finally, the STFT on both stator current and stray flux did not give the expected outcome, with not even the V trajectory of $(1-2s)f_s$ showing in any of the cases. The transient in some faults was very short, while in others the time-frequency resolution was not very high. Moreover, the existence of a certain powerful trajectory starting from 0Hz and reaching up to 50Hz after synchronization was overshadowing all other possible fault harmonic trajectories. It was hypothesized that the particular harmonic is caused by the presence of permanent magnets in the rotor.

Bibliography

[1] I. E. Agency, *World energy outlook*, https://www.iea.org/reports/world-energy-outlook-2024, 2024.

[2] https://www.iec.ch/basecamp/energy-efficient-motors.

[3] https://eu-more.eu/wp-content/uploads/2022/12/U4E-MotorGuide-201709-Final.pdf.

[4] A. de Almeida, F. Ferreira, and J. Fong, "Perspectives on electric motor market transformation for a net zero carbon economy," *Energies*, vol. 16, p. 1248, Jan. 2023. DOI: 10.3390/en16031248.

[5] A. T. de Almeida, F. J. T. E. Ferreira, and G. Baoming, "Beyond induction motors—technology trends to move up efficiency," *IEEE Transactions on Industry Applications*, vol. 50, no. 3, pp. 2103–2114, 2014. DOI: 10.1109/TIA.2013.2288425.

[6] M. J. Melfi, S. Evon, and R. McElveen, "Induction versus permanent magnet motors," *IEEE Industry Applications Magazine*, vol. 15, no. 6, pp. 28–35, 2009. DOI: 10.1109/MIAS.2009.934443.

[7] A. Hassanpour Isfahani and S. Vaez-Zadeh, "Line start permanent magnet synchronous motors: Challenges and opportunities," *Energy*, vol. 34, no. 11, pp. 1755–1763, 2009, ISSN: 0360-5442. DOI: https://doi.org/10.1016/j.energy.2009.04.022. [Online]. Available: https://www.sciencedirect.com/science/article/pii/S0360544209001303.

[8] T. Marcic, B. Stumberger, G. Stumberger, M. Hadziselimovic, P. Virtic, and D. Dolinar, "Line-starting three- and single-phase interior permanent magnet synchronous motors—direct comparison to induction motors," *IEEE Transactions on Magnetics*, vol. 44, no. 11, pp. 4413–4416, 2008. DOI: 10.1109/TMAG.2008.2001537.

[9] F. R. Ismagilov, V. E. Vavilov, and D. V. Gusakov, "Line-start permanent magnet synchronous motor for aerospace application," in *2018 IEEE International Conference on Electrical Systems for Aircraft, Railway, Ship Propulsion and Road Vehicles International Transportation Electrification Conference (ESARS-ITEC)*, 2018, pp. 1–5. DOI: 10.1109/ESARS-ITEC.2018.8607689.

[10] A. C. Smith, E. Peralta-Sanchez, and S. Purbrook, "Line-start permanent magnet motors for pump applications," in *2006 3rd IET International Conference on Power Electronics, Machines and Drives - PEMD 2006*, 2006, pp. 526–530.

[11] I. D. Chasiotis, Y. L. Karnavas, and S. I. Dimadis, "A multi-criteria design method of line-start pmsm with enhanced start-up capability for gantry crane lifting systems," in *2019 IEEE Workshop on Electrical Machines Design, Control and Diagnosis (WEMDCD)*, vol. 1, 2019, pp. 9–14. DOI: 10.1109/WEMDCD.2019.8887855.

[12] W. Fei, P. C. K. Luk, J. Ma, J. X. Shen, and G. Yang, "A high-performance line-start permanent magnet synchronous motor amended from a small industrial three-phase induction motor," *IEEE Transactions on Magnetics*, vol. 45, no. 10, pp. 4724–4727, 2009. DOI: 10.1109/TMAG.2009.2022179.

[13] R. Saxena and R. T. Ugale, "Comparative study of induction motor,permanent magnet synchronous motor and line start permanent magnet synchronous motor using finite element analysis," in *2024 IEEE 11th Power India International Conference (PIICON)*, 2024, pp. 1–5. DOI: 10.1109/PIICON63519.2024.10995051.

[14] B.-A. Kerslake, A. Mahmoudi, and S. Kahourzade, "Line-start permanent-magnet synchronous motor versus induction motor: Technical, environmental and economical considerations," in *2021 IEEE 12th Energy Conversion Congress Exposition - Asia (ECCE-Asia)*, 2021, pp. 857–864. DOI: 10.1109/ECCE-Asia49820.2021.9479424.

[15] S. J. Chapman, *Electric Machinery Fundamentals*. McGraw Hill, 2011.

[16] Α. Ν. Σαφάκας, *Ηλεκτρικές Μηχανές*. Εκδόσεις Ζήτη, 2019.

[17] https://www.linkedin.com/posts/hafsat-idris-0ab738ab_a-3-phase-induction-motor-consists-of-the-activity-7234170685131038720-5uXT/.

[18] O. Chiver, L. Neamt, B. Cristian, and E. Pop, "Study on the autonomous asynchronous generator," in *2018 International Conference and Exposition on Electrical And Power Engineering (EPE)*, 2018, pp. 0863–0866. DOI: 10.1109/ICEPE.2018.8559810.

[19] D. A. Gorski, T. Balkowiec, and W. Koczara, "Grid connection of a converter controlled squirrel-cage induction generator," in *2018 7th International Conference on Renewable Energy Research and Applications (ICRERA)*, 2018, pp. 348–353. DOI: 10.1109/ICRERA.2018.8566730.

[20] https://www.electricaleasy.com/2014/02/production-of-rotating-magnetic-field.html.

[21] https://www.researchgate.net/figure/Two-pole-magnet-assembly-a-three-phase-stator-assembly-b-magnet-stator-with-coaxial_fig1_261598350.

[22] K. N. Gyftakis, "Electromagnetic analysis of induction motor faults and development of new diagnostic methods to detect them," Ph.D. dissertation, University of Patras, 2015.

[23] https://en.wikipedia.org/wiki/Squirrel-cage_rotor.

[24] https://www.swelectric.com/articles/wound-rotor-induction-motor/.

[25] https://www.researchgate.net/publication/268436920_Computation_of_eddy_currents_in_a_solid_rotor_induction_machine_with_2-D_and_3-D_FEM.

[26] https://www.sciencedirect.com/topics/engineering/induction-motor.

[27] F. J. G. Santos, M. K. I. Uemori, and E. C. Bortoni, "A cylindrical rotor synchronous generator design for small hydro power plants," in *2018 XIII International Conference on Electrical Machines (ICEM)*, 2018, pp. 474–478. DOI: 10.1109/ICELMACH.2018.8506831.

[28] K. Hruska, V. Kindl, R. Pechanek, and P. Svetlik, "Design possibilities of multiple-pole cylindrical rotor synchronous machine excitation winding," in *IECON 2014 - 40th Annual Conference of the IEEE Industrial Electronics Society*, 2014, pp. 490–496. DOI: 10.1109/IECON.2014.7048545.

[29] K. N. Gyftakis, C. A. Platero, and S. Bernal, "Off-line detection of static eccentricity in salient-pole synchronous machines," in *2018 XIII International Conference on Electrical Machines (ICEM)*, 2018, pp. 1919–1924. DOI: 10.1109/ICELMACH.2018.8507042.

[30] A.-M. Nicorici, M. Ruba, C. S. Marţiş, L. Szabó, and Z. Máthé, "Comparative analysis of permanent magnet synchronous machines designed for electric power steering applications," in *2020 XI International Conference on Electrical Power Drive Systems (ICEPDS)*, 2020, pp. 1–6. DOI: 10.1109/ICEPDS47235.2020.9249074.

[31] G. Yadagir, M. Sudha, V. S. Reddy G, D. Rani, S. Sophia, and J. F. Roseline, "Artificial neural network and implementation of robotic arm for mineral extraction in mines with permanent magnet synchronous motor," in *2023 International Conference on Inventive Computation Technologies (ICICT)*, 2023, pp. 385–390. DOI: 10.1109/ICICT57646.2023.10134219.

[32] H. Zou, Y. Hu, and S. Zhu, "Optimization of the structural parameter in line-start permanent magnet synchronous machine for traction applications," in *2023 26th International Conference on Electrical Machines and Systems (ICEMS)*, 2023, pp. 4514–4518. DOI: 10.1109/ICEMS59686.2023.10344660.

[33] A. Al-Qarni, A. EL-Refaie, and F. Wu, "Impact of machine parameters on the design of high specific power permanent magnet machines for aerospace applications," in *2021 IEEE International Electric Machines Drives Conference (IEMDC)*, 2021, pp. 1–8. DOI: 10.1109/IEMDC47953.2021.9449592.

[34] M. Glučina, N. Anđelić, I. Lorencin, and Z. Car, "Estimation of excitation current of a synchronous machine using machine learning methods," *Computers*, vol. 12, p. 1, Dec. 2022. DOI: 10.3390/computers12010001.

[35] https://onlinedocs.microchip.com/oxy/GUID-0A4BC4EE-29F5-4736-8125-17139B84E7B5-en-US-2/GUID-C1C929BC-0D12-40FB-B555-F28B23CB457E.html.

[36] https://eee.poriyaan.in/topic/why-synchronous-motor-is-not-self-starting--10210/.

[37] https://circuitglobe.com/two-reaction-theory-salient-pole-synchronous-machine.html.

[38] X. Ba, Z. Gong, Y. Guo, C. Zhang, and J. Zhu, "Development of equivalent circuit models of permanent magnet synchronous motors considering core loss," *Energies*, vol. 15, no. 6, 2022, ISSN: 1996-1073. DOI: 10.3390/en15061995. [Online]. Available: https://www.mdpi.com/1996-1073/15/6/1995.

[39] R. T. Ugale, B. N. Chaudhari, and A. Pramanik, "Overview of research evolution in the field of line start permanent magnet synchronous motors," *IET Electric Power Applications*, vol. 8, pp. 141–154, 4 2014. DOI: 10.1049/iet-epa.2013.0241. eprint: https://digital-library.theiet.org/doi/pdf/10.1049/iet-epa.2013.0241. [Online]. Available: https://digital-library.theiet.org/doi/abs/10.1049/iet-epa.2013.0241.

[40] G. Almandoz, I. Eguren, A. Egea, S. Zarate, G. Ugalde, and A. Urdangarin, "Design of a multipole line start permanent magnet machine," in *2022 International Conference on Electrical Machines (ICEM)*, 2022, pp. 2100–2106. DOI: 10.1109/ICEM51905.2022.9910825.

[41] F. Mahdavi, A. D. Aliabad, and E. Amiri, "Systematic design approach for dual-pole line start permanent magnet synchronous motors," in *2025 IEEE International Electric Machines Drives Conference (IEMDC)*, 2025, pp. 270–274. DOI: 10.1109/IEMDC60492.2025.11061122.

[42] J. Barta, L. Knebl, G. Bramerdorfer, I. Lolova, S. Silber, and O. Vitek, "Topology optimization of rotor bars geometry and arrangement for a line-start permanent magnet synchronous machine," *IEEE Access*, vol. 9, pp. 115 192–115 204, 2021. DOI: 10.1109/ACCESS.2021.3104642.

[43] S. Kahourzade, A. Mahmoudi, R. Ravji, and W. L. Soong, "Line-start axial-flux pm motors: Introduction of a new machine topology," in *2019 IEEE Energy Conversion Congress and Exposition (ECCE)*, 2019, pp. 7027–7034. DOI: 10.1109/ECCE.2019.8912992.

[44] B. M. Dinh, "Optimal Rotor Design of Line Start Permanent Magnet Synchronous Motor by Genetic Algorithm," *Advances in Science, Technology and Engineering Systems Journal*, vol. 2, no. 3, pp. 1181–1187, 2017. DOI: 10.25046/aj0203149. [Online]. Available: http://astesj.com/v02/i03/p149/.

[45] M. Mehrjou, N. Mariun, M. Norhisam, M. A. Mohd Radzi, and S. Musa, "Broken rotor bar detection in ls-pmsm based on startup current analysis using wavelet entropy features," *Applied Sciences*, vol. 7, Aug. 2017. DOI: 10.3390/app7080845.

[46] S. F. Rabbi and M. A. Rahman, "Critical criteria for successful synchronization of line-start ipm motors," *IEEE Journal of Emerging and Selected Topics in Power Electronics*, vol. 2, no. 2, pp. 348–358, 2014. DOI: 10.1109/JESTPE.2013.2295178.

[47] D. Stoia, M. Cernat, A. A. Jimoh, and D. V. Nicolae, "Analytical design and analysis of line-start permanent magnet synchronous motors," in *AFRICON 2009*, 2009, pp. 1–7. DOI: 10.1109/AFRCON.2009.5308177.

[48] M. F. Palangar, W. L. Soong, N. Bianchi, and R.-J. Wang, "Design and optimization techniques in performance improvement of line-start permanent magnet synchronous motors: A review," *IEEE Transactions on Magnetics*, vol. 57, no. 9, pp. 1–14, 2021. DOI: 10.1109/TMAG.2021.3098392.

[49] M. Rahman and T. Little, "Dynamic performance analysis of permanet magnet synchronous motors magnet synchronous motors," *IEEE Transactions on Power Apparatus and Systems*, vol. PAS-103, no. 6, pp. 1277–1282, 1984. DOI: 10.1109/TPAS.1984.318460.

[50] A. H. Isfahani and S. Vaez-zadeh, "Rotor resistance for improved start-up performance of line-start permanent-magnet synchronous motors," in *2018 IEEE Transportation Electrification Conference and Expo (ITEC)*, 2018, pp. 832–838. DOI: 10.1109/ITEC.2018.8450216.

[51] K. Kurihara and M. Rahman, "High-efficiency line-start interior permanent-magnet synchronous motors," *IEEE Transactions on Industry Applications*, vol. 40, no. 3, pp. 789–796, 2004. DOI: 10.1109/TIA.2004.827476.

[52] A. Stening and C. Sadarangani, "The effects of inter-bar currents in cast aluminium and cast copper rotors," in *2008 18th International Conference on Electrical Machines*, 2008, pp. 1–5. DOI: 10.1109/ICELMACH.2008.4800258.

[53] M. Popescu, T. Miller, M. McGilp, F. Kalluf, C. da Silva, and L. von Dokonal, "Effect of winding harmonics on the asynchronous torque of a single-phase line-start permanent-magnet motor," in *Fourtieth IAS Annual Meeting. Conference Record of the 2005 Industry Applications Conference, 2005.*, vol. 4, 2005, 2820–2827 Vol. 4. DOI: 10.1109/IAS.2005.1518860.

[54] B.-t. Kim and B.-i. Kwon, "Influence of space harmonics on starting performance of 1-phase line start permanent magnet motor," in *2006 12th Biennial IEEE Conference on Electromagnetic Field Computation*, 2006, pp. 387–387. DOI: 10.1109/CEFC-06.2006.1633177.

[55] S. Kumar, D. Mukherjee, P. K. Guchhait, *et al.*, "A comprehensive review of condition based prognostic maintenance (cbpm) for induction motor," *IEEE Access*, vol. 7, pp. 90 690–90 704, 2019. DOI: 10.1109/ACCESS.2019.2926527.

[56] M. Karami, N. Mariun, Z. Kadir, M. A. Mohd Radzi, and M. Norhisam, *Analysis of rotor asymmetry fault in three-phase line start permanent magnet synchronous motor*, Dec. 2021. DOI: 10.13140/RG.2.2.24326.91207/2.

[57] J. He, C. Somogyi, A. Strandt, and N. Demerdash, "Diagnosis of stator winding short-circuit faults in an interior permanent magnet synchronous machine," Sep. 2014. DOI: 10.1109/ECCE.2014.6953825.

[58] C. Harlişca, R. Hangiu, L. Szabo, and H. Silaghi, "Broken rotor bars detection in squirrel-cage induction machines by motor current signature analysis method," *Scientific Bulletin of the Electrical Engineering Faculty, Târgovi şte*, vol. 11, pp. 20–25, Jan. 2012.

[59] A. Adouni and A. J. Marques Cardoso, "Thermal analysis of low-power three-phase induction motors operating under voltage unbalance and inter-turn short circuit faults," *Machines*, vol. 9, no. 1, 2021, ISSN: 2075-1702. DOI: 10.3390/machines9010002. [Online]. Available: https://www.mdpi.com/2075-1702/9/1/2.

[60] B. Hecke, Y. Qu, D. He, and E. Bechhoefer, "A new spectral average-based bearing fault diagnostic approach," *Journal of Failure Analysis and Prevention*, vol. 14, Jun. 2014. DOI: 10.1007/s11668-014-9806-6.

[61] W. Z. Zezhi Xing Xiuhe Wang, "Analysis and reduction of electromagnetic force waves of permanent magnet synchronous motors considering rotor eccentricity," *Journal of Electrical Engineering Technology*, vol. 16, pp. 3047–3059, 2021. DOI: 10.1007/s42835-021-00821-6.

[62] T. Orlowska-Kowalska, M. Wolkiewicz, P. Pietrzak, *et al.*, "Fault diagnosis and fault-tolerant control of pmsm drives–state of the art and future challenges," *IEEE Access*, vol. 10, pp. 59 979–60 024, 2022. DOI: 10.1109/ACCESS.2022.3180153.

[63] J. Faiz and E. Mazaheri-Tehrani, "Demagnetization modeling and fault diagnosing techniques in permanent magnet machines under stationary and nonstationary conditions: An overview," *IEEE Transactions on Industry Applications*, vol. 53, no. 3, pp. 2772–2785, 2017. DOI: 10.1109/TIA.2016.2608950.

[64] M. Cheng, J. Hang, and J. Zhang, "Overview of fault diagnosis theory and method for permanent magnet machine," *Chinese Journal of Electrical Engineering*, vol. 1, no. 1, pp. 21–36, 2015. DOI: 10.23919/CJEE.2015.7933135.

[65] S. Nandi, H. Toliyat, and X. Li, "Condition monitoring and fault diagnosis of electrical motors—a review," *IEEE Transactions on Energy Conversion*, vol. 20, no. 4, pp. 719–729, 2005. DOI: 10.1109/TEC.2005.847955.

[66] A. Bellini, F. Filippetti, G. Franceschini, C. Tassoni, and G. Kliman, "Quantitative evaluation of induction motor broken bars by means of electrical signature analysis," *IEEE Transactions on Industry Applications*, vol. 37, no. 5, pp. 1248–1255, 2001. DOI: 10.1109/28.952499.

[67] A. Sharma, L. Mathew, and S. Chatterji, "Analysis of broken rotor bar fault diagnosis for induction motor," in *2017 International Conference on Innovations in Control, Communication and Information Systems (ICICCI)*, 2017, pp. 1–5. DOI: 10.1109/ICICCIS.2017.8660808.

[68] Y. Park, H. Choi, S. B. Lee, and K. N. Gyftakis, "Search coil-based detection of nonadjacent rotor bar damage in squirrel cage induction motors," *IEEE Transactions on Industry Applications*, vol. 56, no. 5, pp. 4748–4757, 2020. DOI: 10.1109/TIA.2020.3000461.

[69] E. Mazaheri-Tehrani and J. Faiz, "Airgap and stray magnetic flux monitoring techniques for fault diagnosis of electrical machines: An overview," *IET Electric Power Applications*, vol. 16, no. 3, pp. 277–299, 2022. DOI: https://doi.org/10.1049/elp2.12157. eprint: https://ietresearch.onlinelibrary.wiley.com/doi/pdf/10.1049/elp2.12157. [Online]. Available: https://ietresearch.onlinelibrary.wiley.com/doi/abs/10.1049/elp2.12157.

[70] K. N. Gyftakis, P. A. Panagiotou, and S. B. Lee, "Generation of mechanical frequency related harmonics in the stray flux spectra of induction motors suffering from rotor electrical faults," *IEEE Transactions on Industry Applications*, vol. 56, no. 5, pp. 4796–4803, 2020. DOI: 10.1109/TIA.2020.3002975.

[71] T. Goktas, M. Arkan, M. S. Mamis, and B. Akin, "Broken rotor bar fault monitoring based on fluxgate sensor measurement of leakage flux," in *2017 IEEE International Electric Machines and Drives Conference (IEMDC)*, 2017, pp. 1–6. DOI: 10.1109/IEMDC.2017.8002342.

[72] T. Goktas and M. Arkan, "Reliable detection of broken bar fault through negative sequence of stray flux in induction motors," in *2023 IEEE International Electric Machines Drives Conference (IEMDC)*, 2023, pp. 1–5. DOI: 10.1109/IEMDC55163.2023.10238997.

[73] P. Ponomarev, L. Aarniovuori, and J. Keränen, "Selection of optimal slice count for multi-slice analysis of skewed induction motors," Oct. 2017, pp. 2149–2153. DOI: 10.1109/IECON.2017.8216361.

[74] https://enterfea.com/electromagnetic-fea/.

[75] https://plm.sw.siemens.com/en-US/simcenter/electromagnetics-simulation/magnet/?srsltid=AfmBOopdPo_TNc2HFi8q1lq28MHorhKq8ZKcLiU2uNx-grhNtH1-PzQA.

[76] H. Norry, A. Yildiz, S. Aksun, and C. Aksoy, "Influence of manufacturing faults on squirrel cage induction motor," in *2024 Fourth International Conference on Advances in Electrical, Computing, Communication and Sustainable Technologies (ICAECT)*, 2024, pp. 1–6. DOI: 10.1109/ICAECT60202.2024.10469352.

[77] J. Bonet-Jara, J. Pons-Llinares, and K. N. Gyftakis, "Comprehensive analysis of principal slot harmonics as reliable indicators for early detection of interturn faults in induction motors of deep-well submersible pumps," *IEEE Transactions on Industrial Electronics*, vol. 70, no. 11, pp. 11 692–11 702, 2023. DOI: 10.1109/TIE.2022.3231333.

[78] A. Ferrah, P. Hogben-Laing, K. Bradley, G. Asher, and M. Woolfson, "The effect of rotor design on sensorless speed estimation using rotor slot harmonics identified by adaptive digital filtering using the maximum likelihood approach," in *IAS '97. Conference Record of the 1997 IEEE Industry Applications Conference Thirty-Second IAS Annual Meeting*, vol. 1, 1997, 128–135 vol.1. DOI: 10.1109/IAS.1997.643018.

[79] B. M. Ebrahimi and J. Faiz, "Configuration impacts on eccentricity fault detection in permanent magnet synchronous motors," *IEEE Transactions on Magnetics*, vol. 48, no. 2, pp. 903–906, 2012. DOI: 10.1109/TMAG.2011.2172977.

[80] R. A. Ayon-Sicaeros, E. Cabal-Yepez, L. M. Ledesma-Carrillo, and G. Hernandez-Gomez, "Broken-rotor-bar detection through stft and windowing functions," in *2019 IEEE Sensors Applications Symposium (SAS)*, 2019, pp. 1–5. DOI: 10.1109/SAS.2019.8706086.

[81] M. E. E.-D. Atta, D. K. Ibrahim, and M. I. Gilany, "Broken bar fault detection and diagnosis techniques for induction motors and drives: State of the art," *IEEE Access*, vol. 10, pp. 88 504–88 526, 2022. DOI: 10.1109/ACCESS.2022.3200058.

[82] D. Morinigo-Sotelo, R. de J. Romero-Troncoso, P. A. Panagiotou, J. A. Antonino-Daviu, and K. N. Gyftakis, "Reliable detection of rotor bars breakage in induction motors via music and zsc," *IEEE Transactions on Industry Applications*, vol. 54, no. 2, pp. 1224–1234, 2018. DOI: 10.1109/TIA.2017.2764846.